

Design, implementation, and characterization of a rack-mountable laser system for the optical control of trapped Calcium 40 ions

A master's thesis submitted to the faculty of mathematics, computer science and physics of the University of Innsbruck in partial fulfillment of the requirements for the degree of

Master of Science (MSc)

carried out at the Institute of Experimental Physics
under the supervision of

Dr. Thomas Monz
Univ.-Prof. Dr. Rainer Blatt

presented by

Alex Steiner

March 2023



Abstract

Ion-trapped quantum computers use lasers of different frequencies to control the electronic states of the ion. The first part of this work deals with the design and characterization of a server rack-based setup for 854 nm and 866 nm laser light, which can supply up to six experiments with light independently. These wavelengths correspond to the electrical transitions of singly ionized calcium 40. The key performance indicator is the frequency drift, measured to be less than 2 MHz. The limiting factor of this measurement is the accuracy of the wavemeter. The rack system is thus more than five times more stable than the previous system.

The second part of the work deals with stabilizing the laser linewidth of a Moglabs 729 nm diode laser to the Hertz regime. This Moglabs system is directly compared to an equivalent diode laser from Toptica. The linewidth of the Moglabs laser is determined to be below 1 Hz using a beat measurement between this laser and a TiSa reference laser. A similar measurement between the Toptica diode laser and the TiSa shows that the linewidths of the Moglabs laser and the Toptica laser are of the same order of magnitude.

Zusammenfassung

Ionenfallen Quantencomputer verwenden Laser verschiedener Frequenzen, um die elektronischen Zustände des Ions zu kontrollieren. Der erste Teil dieser Arbeit befasst sich mit dem Entwurf und der Charakterisierung eines Server-Rack-basierten Aufbaus für 854 nm und 866 nm Laserlichts. Die Wellenlängen der Laser entsprechen den elektrischen Übergängen von einfach ionisiertem Kalzium 40. Der Aufbau kann bis zu sechs Experimente gleichzeitig und unabhängig mit Licht versorgen. Ein wichtiger Leistungsindikator ist der Frequenzdrift, welcher auf weniger als 2 MHz gemessen wird. Der begrenzende Faktor bei dieser Messung ist die Genauigkeit des Wellenmessers. Das rackbasierte System ist mehr als fünfmal stabiler als das vorherige System.

Der zweite Teil der Arbeit befasst sich mit der Stabilisierung der Laserlinienbreite eines Moglabs 729 nm Diodenlasers im Hertz-Bereich. Das Moglabs-System wird direkt mit einem äquivalentem Diodenlaser von Toptica verglichen. Die Linienbreite des Moglabs-Lasers wird anhand einer Schwebungsmessung (Beat) zwischen diesem Laser und einem TiSa-Referenzlaser auf unter 1 Hz bestimmt. Eine ähnliche Messung zwischen dem Toptica-Diodenlaser und dem TiSa zeigt, dass die Linienbreiten des Moglabs-Lasers und des Toptica-Lasers in der gleichen Größenordnung liegen.

Danksagung

Ich möchte mich bei all jenen bedanken, welche mich auf irgendeine Weise während der Durchführung dieser Masterarbeit unterstützt und motiviert haben.

Als erstes bedanke ich mich bei Prof. Rainer Blatt für die Aufnahme in seine Gruppe und die Betreuung dieser Masterarbeit,

Thomas Monz für die Mitarbeit in seinem Projekt, seine Betreuung, den vielen Tipps und Tricks und das Korrigieren der Masterarbeit,

Christian Marciniaik für seine hilfreichen Antworten auf meine vielen Fragen, die Hilfe im Labor und das Korrekturlesen der Masterarbeit,

meinen Kollegen von der "LinTrap", Claire Edmunds, Michael Meth, Lukas Postler und Roman Stricker für die Unterstützung im Labor, all ihren hilfreichen Kommentaren und die zahlreichen interessanten Debatten.

Ein herzliches Dankeschön geht an die Mitarbeiter vom "BigLab" für die interessanten Physik-Diskussionen und all die lustigen Momente,

an meine Mitstudierenden für die Unterstützung und Motivation über die gesamte Dauer des Studiums.

an meine Familie, welche mir das Studium ermöglicht hat, für all ihre Unterstützung und dafür, dass sie stets ein offenes Ohr für mich hat.

Contents

Contents	v
Eidesstattliche Erklärung	vii
1 Introduction	1
2 Creation and modulation of laser light	3
2.1 Diode laser	3
2.1.1 Littrow and Littman design	6
2.1.2 Cat-eye diode laser	8
2.2 Stabilization techniques	9
2.2.1 PID controller	11
2.2.2 Pound-Drever-Hall	12
2.3 Modulation of intensity, frequency, and phase	16
2.4 Characterization of frequency and phase noise	19
2.5 Characterization of intensity noise	21
3 Quantum information processing with trapped ions	22
3.1 Ions in a linear Paul trap	22
3.2 Level scheme of ionized calcium 40	25
3.3 Quantum bit, Bloch sphere, and gate operation	26
4 Design and installation of the rack mountable laser system	30
4.1 Rack structure	30
4.2 Diode laser	32
4.3 Frequency stabilization - BEECH cavity	33
4.4 Distribution of laser light	35
4.5 Double pass units and control electronics	36
5 Characterization of the rack-system	40
5.1 Characterization of the lasers and BEECH	40
5.2 Characterization of the laser light distribution setups	43
5.3 Characterization of the double pass units	44
5.4 Measurements on the ion	46
6 Narrow linewidth diode laser for 729 nm	48
6.1 Setup	48
6.2 Stabilization in the Hertz regime	49
7 Conclusion and outlook	54

Bibliography	56
8 Appendix	60
8.1 Raspbudi Webpage	60
8.2 High bandwidth frequency modulation of an external cavity diode laser using an intracavity lithium niobate electro-optic modulator as output coupler	61

Eidesstattliche Erklärung

Ich erkläre hiermit an Eides statt durch meine eigenhändige Unterschrift, dass ich die vorliegende Arbeit selbstständig verfasst und keine anderen als die angegebenen Quellen und Hilfsmittel verwendet habe. Alle Stellen, die wörtlich oder inhaltlich den angegebenen Quellen entnommen wurden, sind als solche kenntlich gemacht.

Die vorliegende Arbeit wurde bisher in gleicher oder ähnlicher Form noch nicht als Magister-/Master-/Diplomarbeit/Dissertation eingereicht.

Innsbruck, on March 13, 2023

Alex Steiner

1 Introduction

Nature isn't classical, dammit, and if you want to make a simulation of Nature, you'd better make it quantum mechanical, and by golly it's a wonderful problem because it doesn't look so easy.

With this quote, Feynman concluded 1981 his talk at the conference *Simulating physics with computers* [1]. During his talk, he proposed the creation of a more powerful kind of computer, the quantum computer. An idea of the quantum computer is to reduce the computational complexity of certain problems by the means of quantum mechanics and the phenomena of entanglement. The concept of the quantum computer skyrocketed in the 90s and 2000s with the discovery of various algorithms suitable for quantum computing such as the Deutsch-Jozsa algorithm [2] or the Shor's algorithm [3], an efficient quantum algorithm for factoring large integer numbers. Shor's algorithm has raised particular interest as it offers a method to bypass modern encryption methods, such as the RSA cryptosystem, using quantum computers. There are several different approaches pursued to develop quantum computers based on atoms, photons, ions, quantum dots, superconducting circuits, and others [4]. Different physical effects are utilized to encode quantum information in the various setups. For example, trapped ions offer the electric state of the electron to use it as a carrier for the information. The manipulation of those states is typically carried out with the help of lasers which underwent significant development in the last couple of decades [5], to improve output power, increase stability and narrow linewidth. In this work two topics related to diode lasers and quantum information processing with trapped ions are presented:

- **The design of a rack-based laser system based on diode lasers, providing infrared light for single-ionized calcium 40.** The project aims to provide stabilized laser light using a compact, low-maintenance, and modular setup. The rack-based system provides up to six outputs of frequency stabilized 854 nm and 866 nm laser light, with all output ports individually configurable in frequency, phase, and amplitude.
- **The stabilization of a 729 nm diode laser to the Hertz regime.** The goal of the frequency stabilization is to determine the linewidth, lock bandwidth, and noise floor of the laser based on a concept of an intracavity EOM inside a cat-eye external cavity and to compare it to a diode laser using an intracavity EOM inside an external cavity based on the Littrow design. In comparison to standard EOMs, this EOM is reduced in size allowing higher bandwidths while still supporting the stabilization of the laser in the Hertz or sub-Hertz regime.

This thesis is organized as follows: In chapter 2 the theoretical framework for the design choices and the characterization methods of the rack-based system is provided. The focus lies on diode lasers and their frequency stabilization using the

1 Introduction

Pound-Drever-Hall technique. Chapter 3 introduces the concept of qubits and their implementation in trapped ions, focusing on single-ionized calcium 40. The optical transitions and associated lasers important for our experiment are discussed. Chapter 4 motivates why the setup is rack-based and explains the design of the setup in detail. In chapter 5 the rack-based approach is characterized and tested using different characterization methods previously introduced in chapter 2. Chapter 6 presents a method to lock a diode laser to the (sub-) Hertz regime using a high-finesse cavity. The laser linewidth, the lock bandwidth, and the noise floor are investigated and compared to a different diode laser. Chapter 7 concludes the thesis and gives an outlook for future improvements and experiments.

2 Creation and modulation of laser light

The functional principle of a diode laser as well as its frequency stabilization, and reduction of the linewidth are discussed in the following chapter. Furthermore, the characterization of various light parameters such as amplitude, frequency, and polarization is examined. Thereby, the theoretical foundations for chapters 4, 5, and 6 are provided.

2.1 Diode laser

Laser is the acronym for 'light amplification by stimulated emission of radiation'. Depending on the field of application and thus different requirements various types of lasers have been developed, like gas lasers, solid-state lasers, chemical lasers, dye lasers, diode lasers, and more [6]. In the following section, we shall focus on diode lasers since only diode lasers are used in this setup. This introduction to diode lasers is based on chapter 10 of the book *Laser* by Jürgen Eichler [7] and on chapter 5 of *Laserspektroskopie* by Wolfgang Demtröder [8].

Diode lasers are based on semiconductor technology. The energy level structure of semiconductors is thought of as energy bands rather than as single discrete states as it would be the case of e.g. single atoms. The semiconductor is doped with impurities to achieve free-moving electrons and holes. Regions with an excess of electrons in the conducting band are called n-doped while the regions with an excess of (positively charged) holes in the valence band are named p-doped. Both regions are filled up to the Fermi energy, which lies inside the energy band due to the amount of doping. A layer of n- and p-doped semiconductors are connected and form a so-called p-n-junction. A schematic of the p-n-junction of a laser diode is shown in figure 2.1 a). In the region of the p-n-junction electrons (and holes) diffuse from the n-doped region into the p-doped region (p-doped → n-doped region) until the Fermi energy is balanced. Due to the diffusion of electrons and holes near the p-n-junction, a static voltage V_D is created, balancing out the Fermi energy level F and shifting the energy of the valence band (VB) and conducting band (LB). The energy gap between the conducting band and the valence band is given as E_g . Applying a forward bias on the junction injects electrons from the n-layer and holes from the p-layer into the junction and oppositely doped region. In case the applied voltage is similar to the energy gap of the valence band and conduction band, electrons and holes recombine and emit the energy as a photon, see figure 2.1 b). The band gap depends on the type of semiconductor, the mixture of different semiconductors, the doping element, the amount of doping, and more parameters. Changing the band gap results in different photon energy and thus in a different wavelength. The actual design of the diode chip

2 Creation and modulation of laser light

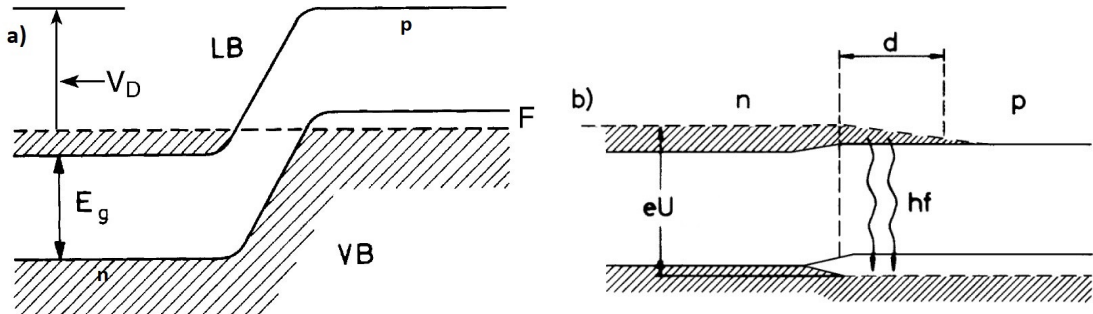


Figure 2.1: Schematic of a p-n-junction with (a) and without (b) applied voltage [7]. A forward current with voltage U is applied to the semiconductor. The potential difference between the p- and n-region is reduced, allowing free movement of electrons and holes. Distance d labels the induction of electrons into the p region. In the region with population inversion (d) stimulated emission is possible. Photons with energy hf (or $h\nu$) are emitted.

depends on the targeted wavelength and type of application [7].

Up to this point the laser diode operates like a light-emitting diode. Amplification of the light by the means of stimulated emission, e.g. by sending the emitted light partially back into the diode, is necessary to create a diode laser. One way to create feedback is to build a cavity resonator using the coated, plane-parallel rear and front facets of the diode itself¹. This cavity is a so-called Fabry-Perot interferometer [7]. Due to internal losses in the diode chip and cavity, the amplification of the laser light starts after exceeding the gain threshold. If the output power of the diode is below the gain threshold the emitted light is primarily created due to spontaneous emission, the laser behaves LED-like. Exceeding the gain threshold compensates for losses in the diode itself and stimulated emission starts to dominate. The power of the emitted light linearly depends on the driving current. Depending on the diode chip a current of hundreds of mA (e.g. laser chip) up to some A (e.g. tapered amplifiers) with an output power of tens of mW up to several W is possible. Since the conversion efficiency of electrons into photons is not unity, cooling of the diode chip is necessary to prevent damage or destruction.

Common diodes have a frequency-dependent gain $g(\lambda)$ amplifying the light over several nanometers around the center wavelength². One reason for the width of the gain profile is the final width of the conducting and valence band in the energy spectrum. Electrons and holes' various energies can recombine, emitting photons with varying wavelengths. The mathematical derivation of the frequency-dependent gain can be found in reference [7]. The Fabry-Perot cavity, used as a feedback element to generate lasing operation, creates a competing gain profile g_{cavity} which is typically narrow in frequency space compared to the laser gain profile. The Fabry Perot cavity suppresses all but standing waves; all other waves interfere destructively to zero over multiple round trips inside the cavity. The so-called phase condition with N a running integer representing the laser mode, n_{eff} the effective refractive index, and L the length of the

¹The surface of the other two spatial directions should be arranged/coated such that no standing waves can be formed.

²Up to about 10% of the center wavelength [7].

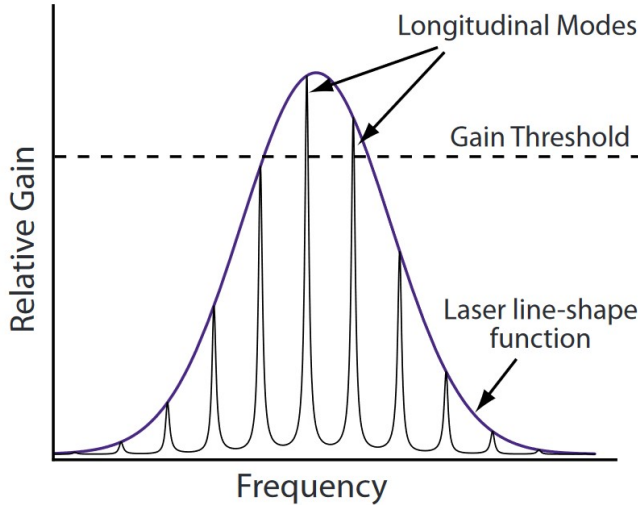


Figure 2.2: Schematic of diode laser gain profile with cavity modes. Depending on the diode laser, multiple modes exceeding the gain threshold can be excited [10].

cavity describes the allowed wavelengths inside the Fabry-Perot cavity [9]

$$\lambda_N = \frac{2n_{\text{eff}}L}{N}. \quad (2.1)$$

The distance between two modes is given by the free spectral range (FSR)

$$\Delta\nu_{\text{FSR}} = \frac{c}{2n_{\text{eff}}L}, \quad (2.2)$$

where c is the speed of light. Figure 2.2 depicts the shape of the overall gain created by the diode laser and the Fabry-Perot cavity. The laser line-shape function is the gain curve formed by the band structure of the diode, while the longitudinal modes are the allowed modes in the Fabry-Perot cavity. The longitudinal modes' relative gain g_{laser} is their product with the laser line-shape function and is the output of the laser. It can be written as

$$g_{\text{laser}} = g(\lambda) \cdot g_{\text{cavity}}. \quad (2.3)$$

The gain threshold marks the point where stimulated emission becomes dominant. A laser in free-running operation may run on multiple modes³ exceeding the gain threshold and can switch between neighboring modes, which is called mode hopping. Mode hops result in a sudden jump in the frequency space. A mode hop may change the frequency up to several free spectral ranges of the cavity. The number of running modes can be influenced by the design of the laser diode and the operating parameters like current or temperature. The gain and loss functions can be chosen in such a way that only one mode is lasing. A laser preferably lasing on only one mode is a so-called single-mode laser. In the scope of this work, multi-mode lasers are neglected since single-mode lasers are required for this project.

³A laser operating on multiple modes is called multi-mode laser.

2 Creation and modulation of laser light

Several physical phenomena contribute to a laser's linewidth both of fundamental and technical nature. For diode lasers, the lower limit for the linewidth is given by the Schawlow-Townes-Henry equation with $h\nu_{\text{ph}}$ the photon energy, v_{gv} the ratio of photon flux to photon density (group velocity) in a dispersive medium, g the laser gain, α_m the facet loss, n_{sp} the population inversion factor, P_{out} the output power, and α_H the Henry linewidth enhancement factor [11] to

$$\delta\nu = \frac{h\nu_{\text{ph}}v_{\text{gv}}g\alpha_m n_{\text{sp}}}{8\pi P_{\text{out}}} (1 + \alpha_H^2). \quad (2.4)$$

The minimum linewidth is given by quantum fluctuations, like amplitude and phase fluctuation generated by spontaneous emissions of photons into the lasing mode and is typically in the order of 10% of the center wavelength (see footnote 2). Diode lasers suffer from additional line broadening by a factor of $(1 + \alpha_H^2)$ due to variations in the real and imaginary part of the refraction index. A free-running diode laser does not reach the linewidth given by the Schawlow-Townes-Henry equation due to induced line broadening caused by mechanical, thermal, and current instability. Typical linewidths for standard diode lasers with a Fabry-Perot length of tenths of millimeters are in the range of 1 – 10 MHz (compare ref [9, 12, 13]).

An external cavity can be used to reduce the linewidth of the laser even further and simultaneously select the lasing mode (external cavity diode laser - ECDL). In the following section, two different approaches for stabilizing a diode laser with an external cavity are discussed. In the first subsection, grating-based external cavities are examined, while in the second subsection, the grating is replaced with a narrow filter and a so-called cat-eye reflector.

2.1.1 Littrow and Littman design

One way to reduce the linewidth is to increase the cavity length. Increasing the length of the diode chip itself is challenging: On one hand, a chip can only withstand a certain light power (for single-mode typically hundreds of mW) before it burns out. A chip ranging several centimeters may exceed the damage threshold. On the other hand, the difficulty of functional chip creation correlates to the physical chip size. The yield Y of defect-free chips decreases exponentially depending on the chip size A and the process defect density D (Poisson model: $Y = e^{-A \cdot D}$).

A typical solution regarding the cavity length is to use an external cavity created by the rear end of the diode and an additional feedback element. The cavity created by the facets of the diode may be suppressed by applying an anti-reflection (AR) coating on the front facet. A common external cavity design using a grating as a feedback element is the Littrow configuration (see figure 2.3 a) and b)). The grating fulfills two main objectives: creating the external cavity and selecting the lasing mode. The Littrow setup is commonly used in two configurations: Littrow type I (a) and type II (b). The difference between both configurations is the output path. In type I the 0th order of the grating is used while in type II an additional mirror behind the laser diode with a reflectivity < 100% is utilized to stabilize the laser frequency and operates as a frequency selective element. The diffraction of the laser light with wavelength λ from the grating can be described using the Bragg equation

$$m\lambda = d(\sin \alpha + \sin \beta), \quad (2.5)$$

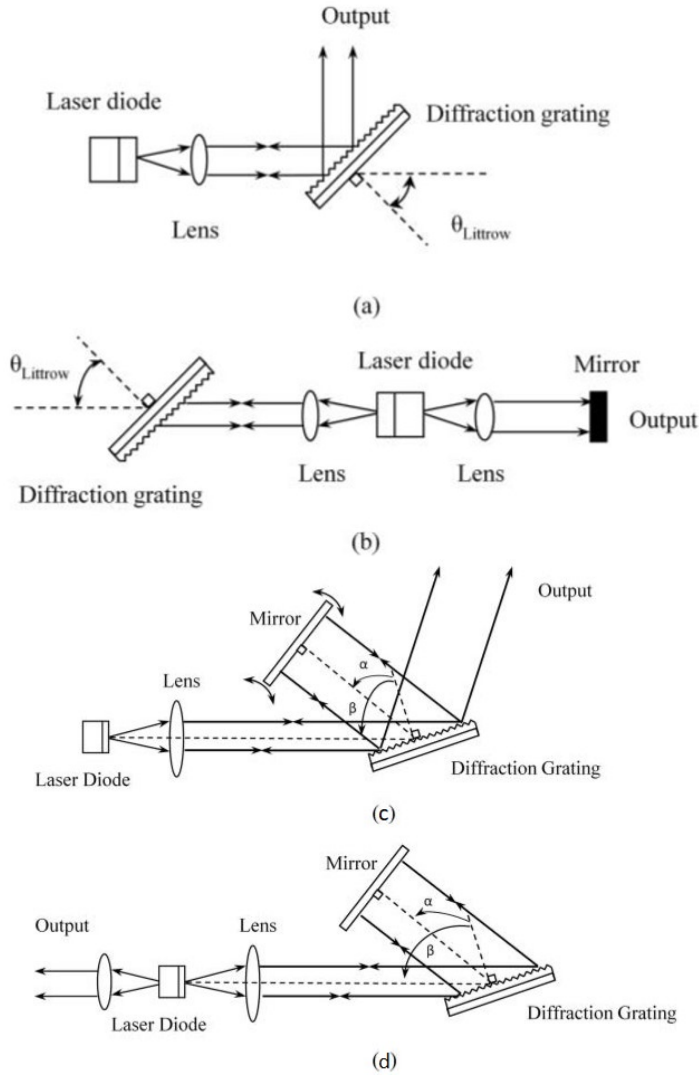


Figure 2.3: Subfigure a) and b) show two configurations of the Littrow design. The -1st order is sent back to the laser creating the feedback of the external cavity. Subfigures c) and d) show the Littman design. An additional mirror is used to create the external cavity. Figure taken from [12].

where m is the diffraction order, d is the grating constant, $\sin \alpha$ is the incident angle, and $\sin \beta$ is the diffraction angle. In the Littrow configuration $\sin \alpha = \sin \beta$ applies. The diffracted beam should be used for feedback. The advantage of the Littrow type I setup is a cheap, easy-to-build stabilization for many commercial laser diodes. A drawback of this setup is that the direction of the output beam depends on the wavelength (2.5) and thus misalignment of the experimental setup is likely in case of wavelength tuning of the laser. Type II decouples the direction of the output beam from wavelength changes, but requires AR-coatings and access to both chip facets. A drawback of type II is a reduction in output power since the output beam is not the 0th order of the grating but rather the transmission through the output mirror [12]. The power in the 0th order of the grating is not used and thus lost.

A second commonly used external cavity design based on a grating is the Littman(- Metcalf) design. It aims to eliminate the wavelength-dependent output direction. The

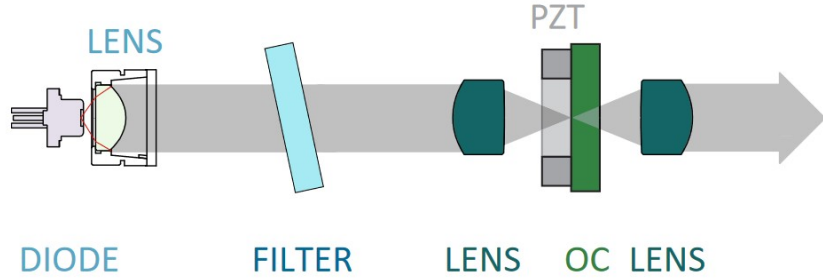


Figure 2.4: In this figure the cat-eye setup is shown. The external cavity is formed by the rear end of the laser diode and a mirror mounted on a piezo electric compound (here Lead zirconate titanate - PZT). A lens is used to focus the laser onto the mirror (cat-eye reflector). The mode is selected by an ultra-narrow bandwidth filter. The outgoing beam is focused by using another lens [15, 16].

setup is shown in figure 2.3 c) and d). The -1st order of the laser beam diffracted on the grating is back-reflected on the grating using a mirror. The grating diffracts the incoming beam a second time and the -1st order is sent as feedback to the laser diode if the mirror is properly aligned, resulting in using the -1st order of the -1st order as feedback. Aligning the Littman-Metcalf configuration requires only the rotation of the mirror, not the grating itself, leading to a fixed output direction of the 0th order while tuning the laser. The Littman-Metcalf configuration provides a better wavelength selectivity and narrower linewidth than the Littrow configuration since the light is diffracted twice on the grating and the cavity length is increased. The drawback of the design is a reduction in power of the feedback beam by double passing the grating [12, 14]. Depending on the focus of the setup on linewidth or power either the Littrow or Littman design may be selected. The Littrow design provides higher power at the cost of broader linewidth in comparison to the Littman setup, which provides lower power at narrower linewidth.

2.1.2 Cat-eye diode laser

Creating the external cavity of a diode laser in air using a grating is sensitive to vibrations as well as potential misalignment due to temperature, pressure, and humidity changes. A so-called 'cat-eye' reflector replaces the grating as a frequency-selective element improving the mechanical stability and creating more stringent frequency dependence on the output. Figure 2.4 shows the cat-eye design. The laser diode has a high reflection-coated rear facet and a low (few percent) reflection-coated front facet. The feedback from the external cavity is created using a partially reflecting mirror (OC - output coupler) mounted on a piezoelectric crystal to adjust the cavity length. A lens focuses the laser light on the mirror while a second lens on the other side of the mirror collimates the outgoing light. The setup consisting of the mirror in the focal point of the lens is the so-called cat-eye giving the name to the external cavity setup. The main advantage of the cat-eye is that in the first order the reflection does not depend on the orientation of the mirror.

The frequency-selecting element is an intracavity, narrow bandpass filter instead of

the grating used in the Littrow and Littman design. Mode selection of the laser depends on different gain and loss factors: The total frequency depending transmission function T_{total} ⁴ with G_D the gain of the laser diode, T_D the transmission function of the internal laser diode cavity, T_{ext} the transmission function of the external cavity, and T_{filter} the transmission function of the narrow filter, can be written as

$$T_{\text{total}} = G_D T_D T_{\text{ext}} T_{\text{filter}}. \quad (2.6)$$

The maximum of T_{total} defines the laser oscillation and opens the possibility to run the laser either multi-mode or single-mode. The rotation of the intracavity, narrow bandpass filter is a convenient way of changing T_{total} . The transmission wavelength of the filter depends on the angle of incidence, on the wavelength λ_0 at normal incidence, on the angle of incidence θ , and on the effective refractive index η_{eff} (typically ≈ 2). The transmission function is given as

$$\lambda(\theta) = \lambda_0 \sqrt{1 - \frac{\sin^2 \theta}{\eta_{\text{eff}}^2}}. \quad (2.7)$$

Rotating the filter changes the gain of (2.6) and therefore tunes the wavelength of the laser. The dependence of the wavelength on the angle of incidence is smaller than in the Littrow configuration, which leads to a higher resilience against mechanical noise [16]. The cat-eye reflector is self-aligning and insensitive to optical misalignment [17]. Furthermore, using an intracavity filter reduces beam walking after tuning the laser since the displacement of the outgoing beam is lower than for the Littrow configuration. Red and near-infrared lasers are demonstrated in [16] and [17]. Both sources report single-mode lasing, high passive stability, and narrow linewidth of 14 kHz at 852 nm and at a cavity length of 70 mm [16], and of 26 kHz at 780 nm and at a cavity length of 30 mm [17].

2.2 Stabilization techniques

An external cavity stabilizes the frequency and reduces the linewidth of a diode laser and can react to noise induced by the environment if controlled actively. Active regulation circuits are a possibility for stabilizing the frequency below the environmentally induced noise level and can potentially reduce the linewidth to the limit given by the Schawlow-Townes-Henry equation (2.4).

The research field dealing with active feedback loops and control circuits is control theory. The objective of control theory is to design systematic, fast converging, and stable (avoiding oscillations) feedback loops that react to disturbances or changes in the output signal [18]. A feedback loop manipulates one or more elements dynamically depending on the measured output(s) of the system to match a given reference parameter. A common example of such a feedback loop is changing the current going through a Peltier element (or other heating/cooling device) dynamically to hold the temperature at a given value despite a change in temperature of the environment. The first step in implementing control theory is the mathematical description of the

⁴Note that T_{total} is equal to g_{laser} of equation (2.3), where g_{cavity} is replaced with multiple gain and loss factors.

2 Creation and modulation of laser light

model of the system and define variables that have to be controlled and/or can be optimized. The boundary conditions of the mathematical description are based on specific conditions of the output signal and on the performance effort of achieving the goals. The established mathematical model is analyzed in detail to find an appropriate optimization technique that can be implemented and fulfills the target goals in convergence and complexity. Depending on the complexity of the system, the mathematical model can either be solved analytically or numerically [18].

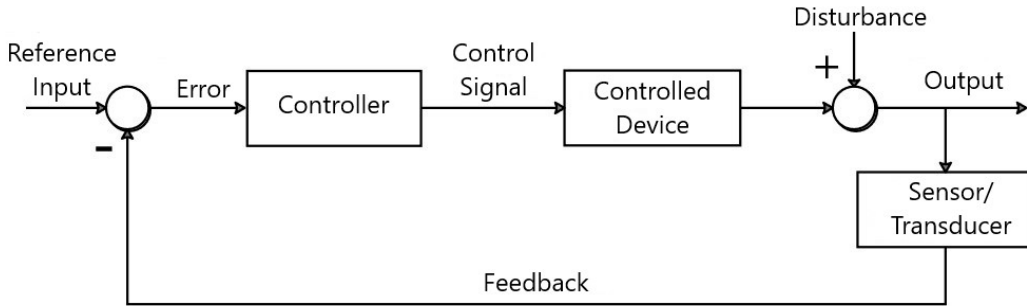


Figure 2.5: Block diagram of a (feedback-) control system [19].

The outline of the mathematical model can be illustrated in a block diagram as shown in figure 2.5. A feedback loop consists typically of a reference signal input, a controller, the controlled device/experiment, and a sensor/transducer [18, 19]. In a real control circuit, it is possible and likely, that there are multiple instances of one or more elements shown in this block diagram.

The output of a device/experiment can be influenced by disturbance introduced by the environment. A sensor/transducer is used to measure some part of the output signal, creating a so-called feedback signal. The difference between the feedback signal and a reference input is the error signal. The reference input is the desired value/set point of the device/experiment. Note that the stability of the control loop is directly dependent on the stability of the reference input. Changes in the reference signal are transmitted to the output signal. The error signal is fed into a controller that tries to minimize the error signal by changing the control parameter of the controlled device/experiment. This loop is the so-called feedback loop.

A control loop can account for the effect of some disturbance in the signal even before the disturbance has happened if knowledge about how some type of disturbance acts on an output signal is available. This type of control loop is called feed-forward, (also feedforward or Feed Forward) [20, 21]. However, introducing feed-forward is only beneficial if the disturbance can be measured before it acts on the signal. In combination with a feedback loop, it can strongly reduce the amount of required counteraction.

2.2.1 PID controller

Fast⁵ and robust⁶ controllers are needed to create feedback loops with and without feed-forward. A widely used controller is the Proportional–Integral–Derivative (PID) controller. As the name suggests, the PID controller is based on three control terms: one proportional to the error, one proportional to the time integral of the error, and one proportional to the (first) time derivative of the error. The proportional controller (P) acts on the present error signal and increases/decreases the magnitude of the control variable when the error increases/decreases. The P term needs a non-zero error to adjust the system; therefore, P alone can hardly reach zero error. The control function $u(t)$ of the proportional controller acting on the error signal $e(t)$ can be mathematically described by a proportional term k_p to

$$u(t) = k_p e(t). \quad (2.8)$$

The integral controller (I) is proportional to the integrated past evolution. It is proportional to the area beneath the error curve. The control function with gain k_i is given by

$$u(t) = k_i \int_0^t dt' e(t') \quad (2.9)$$

The steady-state error can be reduced to zero using the integral controller. The derivative controller (D) tries to handle the future values of the error signal based on the change in the current error signal. The control function of D is given by

$$u(t) = k_d \frac{de(t)}{dt}, \quad (2.10)$$

where k_d is the respective gain. The derivative controller is used to improve signal damping. A PID controller consists of the summation of the three individual control terms. The control function of the PID is given by

$$u(t) = k_p e(t) + k_i \int_0^t dt' e(t') + k_d \frac{de(t)}{dt}. \quad (2.11)$$

The effect of P, I, and D can be increased or reduced by changing the respective gain parameter $k_{p,i,d}$. Reducing a gain to 0 switches the related action off. For example, reducing k_d to 0 transforms the PID it a PI controller.

The block diagram of the PID controller is illustrated in figure 2.6. These three elements substitute the controller of the block diagram 2.5. In the case of noisy data, the PID controller can be reduced to a pure PI controller. The PI controller is more stable against noise than the PID since the D term is sensitive to high-frequency terms in the error signal. The drawback of neglecting D is the increase in time required to reach the set point and a slower reaction to perturbations of the system (compared to a PID). Multiple integrator and differentiator stages can be stacked to increase the robustness of a PID. They are labeled as $PI^\lambda D^\mu$, where λ is the number of integrator stages, and μ is the number of differentiator stages. The integrator and differentiator stages are built in a way that they are frequency-dependent, acting only on noise

⁵relative to the bandwidth of the noise

⁶resilient to a broad range of effects

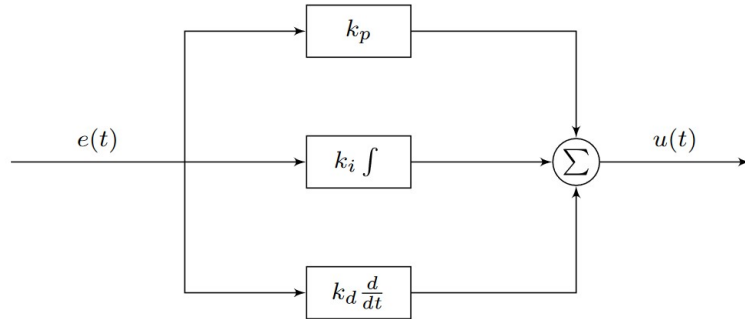


Figure 2.6: Block diagram of a PID combining the proportional, integral, and derivative term [22].

inside a specific frequency bandwidth [22, 23].

Multiple different algorithms were developed on how to tune a PID controller like the Ziegler–Nichols method [24] or the Relay (Åström–Hägglund) method [25]. Instead of using an algorithm to tune a PID controller, manual PID tuning is an option. In the following paragraph, a brief 'lab-tested' description of manual PID tuning is given: The gain parameters k_i and k_d are set to zero while the proportional gain k_p is increased until the output of the control loop starts oscillating. At this point, the proportional gain is reduced by 50%, creating a so-called *quarter amplitude decay*-type response. The integral gain is increased to minimize the offset created by the proportional gain. A too-large integral gain creates overshoot of the proportional term and an unstable control loop. At this point, the PID operates as a PI controller. The D term is increased to reduce the overshoot and damp the system to the setpoint. A too-large derivative gain creates overshoot and destabilizes the system. Manual tuning a PID controller requires some experience.

A common application of a PID controller is temperature stabilization of sensitive parts or locking a laser onto a reference and thereby stabilizing the frequency actively. In the following subsection, laser frequency stabilization using a PID controller is discussed.

2.2.2 Pound-Drever-Hall

One idea of stabilizing a laser is using a Fabry-Perot cavity⁷ as a reference and give feedback to the laser to suppress frequency fluctuations. A Fabry-Perot cavity acts like a frequency discriminator. Light fulfilling the phase condition (see equation (2.1)) is transmitted while other frequencies are suppressed. Operating the laser near one of the cavity resonances creates a non-zero transmission signal. In figure 2.7 the transmission signals for three transmission lines and two finesse⁸ F are shown. Finesse is the ratio of the free spectral range $\Delta\nu_{\text{FSR}}$ and the FWHM of the transmission lines.

$$F = \frac{\Delta\nu_{\text{FSR}}}{\Delta\nu_{\text{FWHM}}} \quad (2.12)$$

⁷Note that many different locking methods use other types of cavities.

⁸Finesse is a measure to characterize Fabry-Perot cavities.

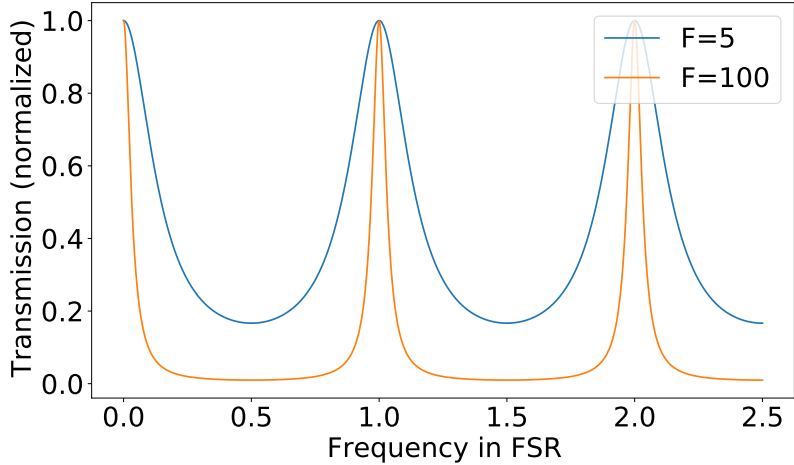


Figure 2.7: Transmission lines of a Fabry-Perot cavity with finesse 5 and 100.

In principle, the transmission through the cavity could be used as feedback for the laser. Two options using the transmission signal are common: top-of-fringe lock and side-of-fringe lock. As the name indicates, the top-of-fringe lock requires that the frequency of the laser matches the point where the transmission through the cavity is at maximum. A deviation of the laser frequency reduces the transmitted power detected by a photodiode, returning the measured value to the feedback loop to adjust the laser frequency. The downside of using a top-of-fringe lock is that there is no possibility of knowing in which direction the frequency of the laser is drifting since the transmission signal is symmetric around the setpoint. Therefore, a deviation is detected, but the correct response is unknown.

Side-of-fringe locking operates the laser frequency on the side of one transmission line. Commonly one of the points at 50% of the maximum amplitude is chosen since the slope may be nearly linear around that point. A deviation of the frequency either increases the transmission or decreases it. In contrast to top-of-fringe locking, the direction of the frequency deviation is well-known and the laser can be manipulated to stabilize the frequency.

A key drawback of side-of-fringe locking is that the control circuit can not distinguish between the amplitude noise of the laser light and frequency noise. Amplitude noise modulates the transmitted power through the cavity and is picked up by the photodiode. Therefore, amplitude noise is converted into frequency noise. In order to use top-of-fringe and side-of-fringe locking efficiently, a way of decoupling amplitude noise from frequency noise has to be found. Several locking schemes decoupling amplitude from frequency noise are available [26–28]. A common scheme is the Pound-Drever-Hall (PDH) method. This section follows the book *Frequency standards: basics and applications* by Fritz Riehle [13] and the paper *An introduction to Pound–Drever–Hall laser frequency stabilization* by E. D. Black [28].

The idea of the PDH lock is to use the reflected beam of the Fabry-Perot cavity to compensate for frequency fluctuations. Focusing on the reflected signal reveals the same issue as known from top-of-fringe locking: it is not possible to determine the direction of the frequency drift since the reflection is symmetric relating to the resonance. The solution to this problem is that the first derivative of the reflection is

2 Creation and modulation of laser light

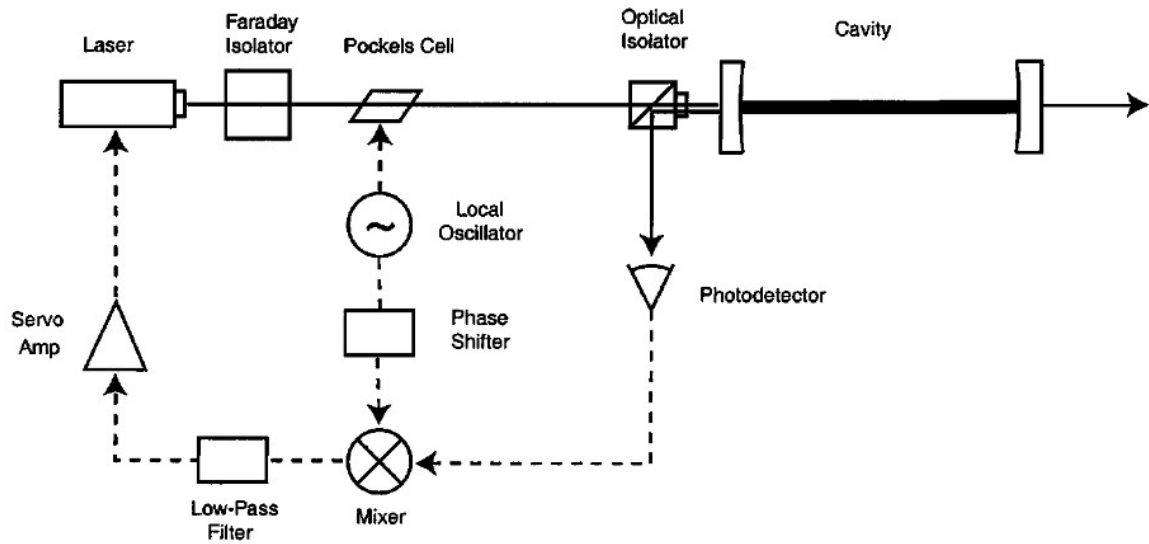


Figure 2.8: Optical and electrical setup used to create a PDH lock [28]. The laser light is modulated using a Pockels cell and is sent on the Fabry-Perot cavity, whose reflection and leakage are detected by a photodiode. The measured signal is mixed with the oscillation driving the Pockels cell. The mixed signal is sent to a low-pass filter and processed by a control unit providing feedback to the laser.

antisymmetric regarding the resonance. The reflected beam consists of two terms, the reflected part of the front mirror of the cavity and the leakage of the light from the cavity. The relative phase of these beams depends on the frequency of the laser beam. If the frequency matches the resonance exactly, the reflected and the leaked beam are 180° out of phase and cancel each other out. If the frequency of the laser does not match the resonance, the phase is not exactly 180° resulting in only a partial cancellation of the beams. Measuring the phase of the leftover part indicates on which side of the resonance the laser is operating. To this date, there is no possibility to measure the phase of light directly. Nevertheless, this can be bypassed by dithering the frequency (or phase) of the laser and thereby creating sidebands at the frequency of the dither around the laser frequency (also called the carrier). The sidebands have a definite phase relationship to the incident and reflected beams. The phase of the reflected beam can be determined by measuring the phase of the beat pattern of the sidebands with the reflected beam.

An exemplary setup for PDH is shown in figure 2.8. The laser is protected from reflections by a Faraday isolator. The dithering of the laser frequency is generated using a Pockels cell modulating the phase of the laser beam resulting in an electric light field of

$$E_{\text{inc}} = E_0 e^{i(\omega t + \beta \sin \Omega t)}, \quad (2.13)$$

where E_0 is the amplitude of the electric field, ω is the frequency, β is the modulation depth, and Ω is the phase modulation frequency. Rewriting it using the Bessel function expands into

$$E_{\text{inc}} = E_0 [J_0(\beta) e^{i\omega t} + J_1(\beta) e^{i(\omega+\Omega)t} - J_1(\beta) e^{i(\omega-\Omega)t}]. \quad (2.14)$$

For small modulation depths $\beta < 1$ the total power $P_0 = |E_0|^2$ splits into the power of the carrier

$$P_c = J_0^2(\beta)P_0 \quad (2.15)$$

and the first-order sidebands

$$P_s = J_1^2(\beta)P_0. \quad (2.16)$$

The beam is coupled into the Fabry-Perot cavity, and some part of the transmission is measured by the means of a photodiode. The reaction time of the photodiode depends on the size of the diode chip since the size of the chip is related to the capacity which is further related to the speed of the readout. Lower capacity results in faster readout, which is favorable for PDH. The transmission signal can be used to check if the laser is in resonance with the Fabry-Perot cavity. The reflection of the front mirror and the leakage out from the cavity are separated from the incoming beam using an optical isolator like a (polarizing) beam cube. The reflection is given as

$$E_{\text{ref}} = E_0[F(\omega)J_0(\beta)e^{i\omega t} + \dots] \quad (2.17)$$

$$F(\omega + \Omega)J_1(\beta)e^{i(\omega+\Omega)t} - F(\omega - \Omega)J_1(\beta)e^{i(\omega-\Omega)t}], \quad (2.18)$$

where

$$F(\omega) = \frac{E_{\text{ref}}}{E_{\text{inc}}} = \frac{r \left(\exp \left(i \frac{\omega}{\Delta\nu_{\text{FSR}}} \right) - 1 \right)}{1 - r^2 \exp \left(i \frac{\omega}{\Delta\nu_{\text{FSR}}} \right)} \quad (2.19)$$

is the reflection coefficient for a symmetric cavity with no losses. A photodiode is used to measure the power of the reflected beam, given as

$$\begin{aligned} P_{\text{ref}} = & P_c|F(\omega)|^2 + P_s(|F(\omega + \Omega)|^2 + |F(\omega - \Omega)|^2) \\ & + 2\sqrt{P_c P_s} \text{Re}[F(\omega)F^*(\omega + \Omega) - F^*(\omega)F(\omega - \Omega)] \cos \Omega t \\ & + 2\sqrt{P_c P_s} \text{Im}[F(\omega)F^*(\omega + \Omega) - F^*(\omega)F(\omega - \Omega)] \sin \Omega t + (2\Omega \text{ terms}). \end{aligned}$$

The reflection measured by the photodiode consists of three parts, the carrier at frequency ω and the sidebands at frequencies $\omega \pm \Omega$. The term proportional to Ω arises due to interference of the carrier with the sidebands and the 2Ω terms result from the interference of both sidebands. The terms of interest for PDH are the terms depending on the modulation frequency Ω^9 since they contain information about the phase of the carrier. Depending on the modulation frequency, the term proportional to $\cos \Omega$ (low modulation frequency) or $\sin \Omega$ (high modulation frequency) remains while the other vanishes. It is mixed with the driving signal of the Pockels cell which is proportional to $\sin \Omega'$ to extract these terms from the measured signal of the photodiode. The mixer forms the product of its inputs and either a term proportional to

$$\sin \Omega \cos \Omega' = \frac{1}{2} (\cos [(\Omega - \Omega')t] - \cos [(\Omega + \Omega')t]) \quad (2.20)$$

or

$$\sin \Omega \sin \Omega' = \frac{1}{2} (\sin [(\Omega - \Omega')t] - \sin [(\Omega + \Omega')t]) \quad (2.21)$$

⁹The modulation frequency is compared to the free spectral range to determine if it operates in the low or high modulation regime.

2 Creation and modulation of laser light

is received. For $\Omega = \Omega'$ the error signal is the dc signal $\cos[(\Omega - \Omega')t]$ or $\sin[(\Omega - \Omega')t]$. In the case of $\sin[(\Omega - \Omega')t]$ and $\Omega = \Omega'$ the dc signal vanishes. A phase shifter is used to shift the signal produced by the local oscillator in such a way that either $\sin \Omega \cos \Omega'$ or $\cos \Omega \sin \Omega'$ is received, resulting in a non-zero error signal. Furthermore, the phase shifter is used to compensate for possible phase delays in one of the signals. The term oscillating at $\Omega + \Omega'$ is removed using a low pass filter. In the case of low modulation frequencies, the extracted error signal is given as

$$\epsilon \approx 2\sqrt{P_c P_s} \frac{d|F|^2}{d\omega} \Omega, \quad (2.22)$$

while the error signal in the case of high modulation is

$$\epsilon \approx -\frac{4}{\pi} \sqrt{P_c P_s} \frac{\delta\omega}{\delta\nu} = -\frac{8\sqrt{P_c P_s}}{\delta\nu} \delta f. \quad (2.23)$$

The error signals for a low and a high modulation frequency are shown in figure 2.9. Both error signals are asymmetric respective to the resonance and are independent of amplitude noise, which was the aim to introduce PDH as a locking method. A side-of-fringe lock at the position of the resonance on the error signal can be used to lock the laser on the resonance of the Fabry-Perot cavity. The error signal is sent to a PID controller, that controls the laser and holds it at the resonance of the Fabry-Perot cavity, to close the control loop.

The Pound-Drever-Hall method relies on modulating sidebands on the laser frequency. Otherwise, no error signal is created. The following section describes how the modulation of sidebands on the carrier is achieved.

2.3 Modulation of intensity, frequency, and phase

Polarizing components are a possibility of changing the amplitude of (polarized) light. Two types of polarizers are common: polarization filters based on dichroism¹⁰ and polarization filters based on birefringence¹¹. Both types of polarizers have two axes of polarization. One axis is nearly 100% transparent (no absorption) while the other axis is either deflected (birefringence) or absorbed (dichroism). Rotating the polarization axis of the light relative to the axis of the polarizing element changes the intensity of transmission and deflection/absorption. A common element based on birefringent material where a phase shift is introduced in the axis of polarization depending on the length of the element is the waveplate. Usual types of waveplates either rotate the polarization (half-waveplate) or change it from linear to circular (quarter-waveplate) and vice versa. Waveplates in combination with an element based on dichroism or birefringence are mostly used if a static change in the amplitude of the light is necessary.

Electro-optical (EOM) or acousto-optical (AOM) modulators [29] allow frequency, phase, and amplitude modulation rates up to the MHz-regime or even GHz-regime [7]. EOMs typically use a linear change of the birefringence of a crystal depending on the applied electric dc or slow ac field. It is called the Pockels effect.

¹⁰Different polarizations are absorbed differently inside the material.

¹¹The index of refraction depends on the polarization and propagation of light

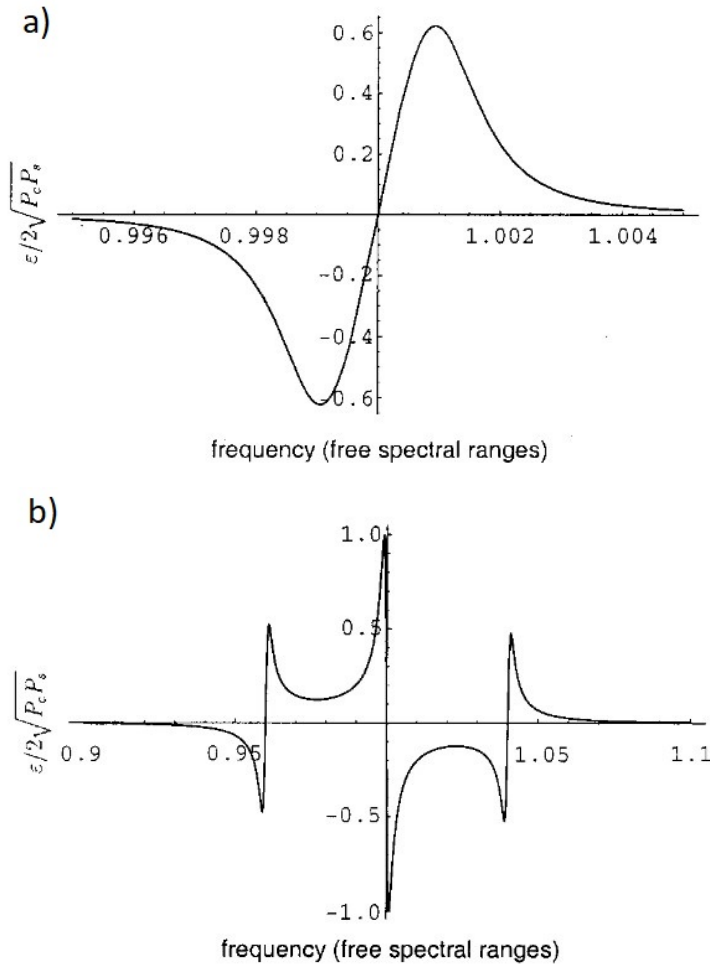


Figure 2.9: a) Pound-Drever-Hall error signal for a low modulation frequency ($10^{-3} \cdot \Delta\nu_{\text{FSR}}$). b) Pound-Drever-Hall error signal for a high modulation frequency ($4\% \cdot \Delta\nu_{\text{FSR}}$). The finesse of the cavity is 500. Picture taken from [28].

In order to create the electric field E in the nonlinear crystal, electrodes with a voltage U at a distance d are used. The internal structure of an EOM is shown in figure 2.10. The polarization of the light entering the crystal is rotated by 45° compared to the polarization axis of the crystal. It ensures that both polarization axes of the crystal are populated equally. The difference in the refractive index n between both polarization arms depends on a material constant r and is given by

$$\Delta n = n^3 r E = n^3 r \frac{U}{d}. \quad (2.24)$$

A phase shift between the light of both axes is accumulated as it passes through the crystal due to the birefringence. Combining the Pockels cell with a polarizer enables the control of the intensity of the laser beam. Depending on the length of the crystal and the desired change in refractive index a driving voltage of several hundred V up to some kV is possible.

A modulator working at low voltages is the acousto optical modulator. It is based on diffraction on a (moving) grating. The grating is created by traveling acoustic

2 Creation and modulation of laser light

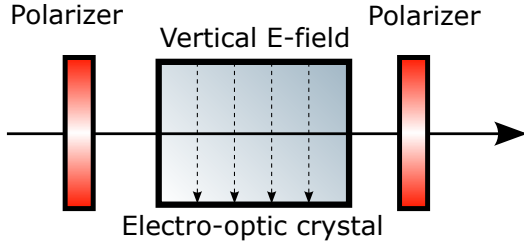


Figure 2.10: Setup of a transversal EOM. Two electrodes create a vertical electric field inside the electro-optic crystal. The polarizer in front of the electric crystal matches the polarization of the light with the alignment of the crystal while the second polarizer (additional) reduces the amplitude of the electric field depending on its polarization.

waves through a crystal changing the density and thus the refractive index locally. The frequency of the sound f_{sound} wave is typically in the range of 50 – 500 MHz. Dividing the sound velocity v by the frequency of the sound f_{sound} yields the acoustic wavelength $\Lambda = v/f_{\text{sound}}$.

A piezoelectric transducer converts the driving rf-frequency into an acoustic wave. An absorber on the opposing side of the crystal prevents the formation of standing waves inside the crystal such that the light diffracts on a moving grating. The optical power in the diffracted arm depends on the square root of the induced rf-power. Changing the rf-power is a convenient way of changing the optical power in the diffracted and non-diffracted paths.

The modulation rate $1/\tau = v/d$ is limited in the MHz range by the speed of sound and the finite diameter d of the laser beam. Focusing the beam increases the modulation bandwidth by reducing the beam diameter, but reduces the diffraction efficiency since a focused beam does not completely fulfill the Bragg condition.

The diffracted light experiences a change in frequency and phase in addition to power modulation. The frequency of the diffracted light is changed by $\pm f_{\text{sound}}$ opening the possibility of frequency modulation. The frequency shift can be explained by a Doppler shift of the light on the moving grating. Another way of understanding the frequency shift is the momentum and energy conservation of the involved photons and phonons. The photon frequency is shifted by the frequency of the phonons. Furthermore, the phase of the incoming light is shifted by the phase of the sound wave. In some cases, the absorber is removed to allow the formation of standing waves. In this case, the transmitted light gets an amplitude modulation at twice the sound frequency $2f_{\text{sound}}$.

The AOM can be operated in two regimes: diffraction on a thin (Raman-Naht) and a thick (Bragg) grating. The thin grating regime is given by $\lambda l < \Lambda^2$, where λ is the wavelength of the light in vacuum and l is the length of the crystal. The Raman-Nath setup is shown in figure 2.11 a). The incident laser beam is diffracted into multiple orders. The angle between neighboring orders is given by

$$\sin \theta = \frac{\lambda}{\Lambda n}, \quad (2.25)$$

where n is the index of refraction. The maximum diffraction efficiency for a sinusoidal grating is 33.8%. In the Bragg regime, a diffraction efficiency of up to 100% in one order is possible. It is given by $\lambda l > \Lambda^2$. The Bragg regime is shown in figure 2.11 b). Destructive interference occurs between diffracted waves along a grating line if the

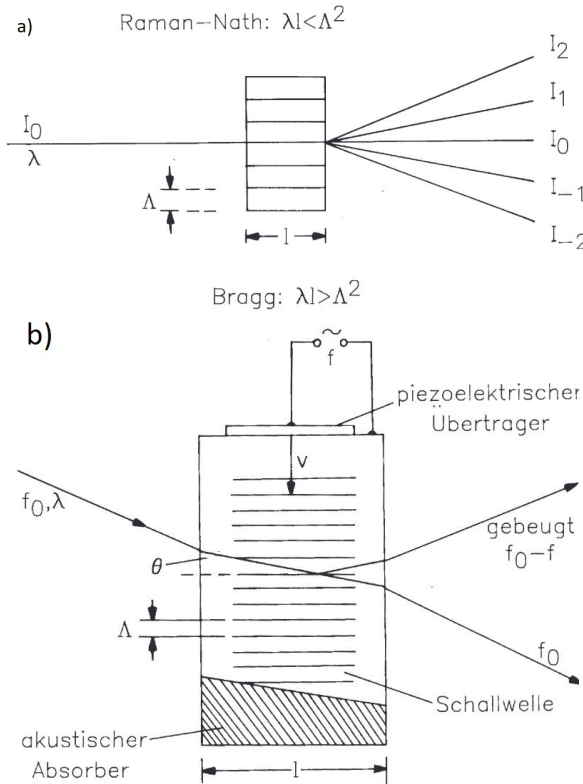


Figure 2.11: AOM setup in the Raman-Nath regime (a) and Bragg regime (b). Figures taken from [7].

angle of incidence of the light beam is perpendicular to the direction of propagation of the sound wave. Rotating the crystal fulfilling the Bragg condition

$$\sin \theta = \frac{\lambda}{2\Lambda n} \quad (2.26)$$

creates constructive interference. Only one order of diffraction appears. The direction of the sound wave inside the crystal defines the sign of the frequency shift $\pm f_{\text{sound}}$ of the light.

The choice of the modulator type depends on the experiment and its specific requirements. Some parameters that influence the decision are cost, available space, switching speed, and efficiency. More on modulators can be found in reference [29].

2.4 Characterization of frequency and phase noise

There is no possibility to measure terms oscillating at the frequency of the lasers since measuring electric signals is limited to the GHz-range and lower. Nevertheless, two different approaches are available to extract information about the frequency and phase of the laser light: homodyne and heterodyne detection [13]. In homodyne detection, the information about the phase or frequency of a modulated signal is extracted by mixing the signal with a local oscillation that is identical to the unmodulated signal. In optics, the local oscillation and the modulated signal are derived from the same

2 Creation and modulation of laser light

laser. In heterodyne detection, the frequency of the local oscillator differs from the signal. Knowing the frequency (and/or phase) of the local oscillator allows measuring the frequency (phase) of the modulated signal.

One way to measure the stability of the phase or frequency of a laser is to rate the stability of one laser in comparison to another, ideally well-defined, reference laser operating at a similar wavelength. This method is called a (heterodyne) beat measurement. It requires a superposition of both laser beams on a photodiode resulting in an electric signal which consists of terms proportional to the sum and difference of the frequencies of the lasers. Only the frequency difference between both lasers can be measured with a photodiode since electric signals are in the GHz-range and lower. The fluctuations are averaged to a DC signal if the differential frequency exceeds the bandwidth of the photodiode¹².

Frequency and phase noise are encoded as modulations onto a laser signal and can be measured using the homodyne or heterodyne measurement scheme. The frequency noise is directly related to the phase noise and is characterized by measuring the frequency noise spectrum [13] or the phase spectral density (PSD) [13]. The frequency noise spectrum describes the noise power per unit of bandwidth and consists typically of random walk, flicker noise, and white noise for a well-stabilized system. Induced noise by different sources may dominate and alternate the measured frequency noise spectrum. An example of a frequency noise spectrum is shown in figure 2.12. Deviations in the noise spectrum are created due to resonances induced by the environment.

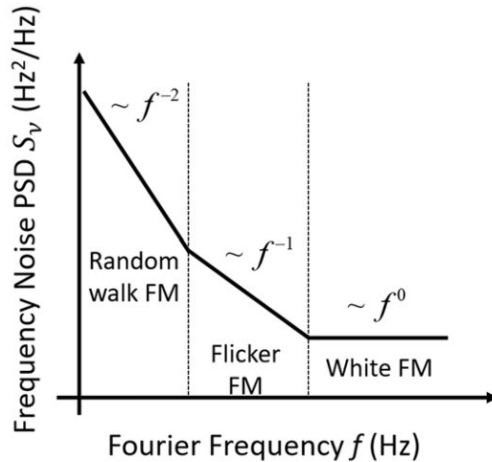


Figure 2.12: The dependence of the noise on the frequency is shown [30]. Both axes are on a logarithmic scale.

Another key parameter is the linewidth of the laser since lasers are commonly used as local oscillators. A local oscillator is required to run more stable as the driven system. The linewidth of the laser can be received by analyzing a PSD, which may be complicated. A faster way to approximate the laser linewidth is to measure the linewidth of the beat directly using a spectrum analyzer. The linewidth of the beat is an upper linewidth of the laser linewidth since the beat is the convolution of both

¹²The resolution bandwidth of a fast photodiode is typically hundreds of MHz or in the GHz-range. It defines the maximum frequency distance between both lasers.

laser linewidths [13].

Not only phase and frequency but also the intensity of the laser beam is sensitive to noise. In the next section, the characterization of intensity noise is discussed.

2.5 Characterization of intensity noise

The intensity noise is quantified with a PSD (similar to the frequency noise). The optical power $P(t)$ of the laser is given by

$$P(t) = \bar{P} + \delta P(t), \quad (2.27)$$

where \bar{P} is the average value and $\delta P(t)$ is the fluctuating part with zero mean value. In contrast to frequency noise, no beat is needed since the power can be directly measured using a photodiode. The photodiode must be operated in a region of linear response. Saturation of the diode should be avoided to not blur the measured data. A spectrum analyzer is used to evaluate the measured spectrum. Another possibility is to use an oscilloscope to measure the signal on a time basis and calculate the fast Fourier-transformation afterward. The lowest measurable noise frequency is the inverse of the total duration while the highest frequency is given by half the sampling rate. The fundamental limit of intensity noise is given by the shot noise to

$$S_l = \frac{2h\nu}{\bar{P}}, \quad (2.28)$$

where $h\nu$ is the energy of one photon [13]. Peaks in the intensity noise spectrum can be induced due to mechanical vibrations and thus changes in the laser resonator. Good protection from vibrations and acoustic waves is needed to reduce the intensity of noise. A further technique to reduce the amplitude noise is to apply active feedback loops for example to regulate the pump power inside the resonator [13].

3 Quantum information processing with trapped ions

The second chapter discussed the properties of laser light, its creation, and stabilization techniques for frequency, phase, and amplitude. For quantum information processing based on trapped ions stable laser light is one fundamental requirement. In this chapter encoding the fundamental unit of quantum computing, the qubit, in trapped ions is discussed.

3.1 Ions in a linear Paul trap

Considering that ions are electrically charged, electric and magnetic fields are favorable to interact with them. However, it is not possible to enclose an ion in a three-dimensional well-defined region using only static electric or magnetic fields [13]. Either a combination of static magnetic and electric fields or a time-dependent inhomogeneous field has to be used [13]. The Paul and the Penning traps are two recognized representatives taking advantage of those fields.

The Penning trap is based on static magnetic and electric fields, while the Paul trap is based on a time-dependent inhomogeneous field. More details about both traps can be found in the chapter *Ion-trap Frequency Standards* of *Frequency Standards* by Fritz Riehle [13]. The trap used in our experiments is a Paul trap, the Penning trap is not further investigated within the scope of this thesis.

Any trap needs a potential $\Phi(\vec{r})$ leading to a force acting on the ions pointing towards the trapping volume at any point in space to enclose the ions in a well-defined region (trapping volume). The force $\vec{F}(\vec{r})$ created by the potential can be expressed as

$$\vec{F}(\vec{r}) = e\vec{E}(\vec{r}) = -e \cdot \nabla\Phi(\vec{r}), \quad (3.1)$$

where e is the electron charge, $\vec{E}(\vec{r})$ is the electric field defined by the potential $\Phi(\vec{r})$ and ∇ is the Nabla operator. Ideally, the force $\vec{F}(\vec{r})$ should increase linearly with distance \vec{r} to allow the particle to perform harmonic oscillations. The scalar potential fulfilling these conditions may be written as

$$\Phi(x, y, z) = C(ax^2 + by^2 + cz^2), \quad (3.2)$$

where a , b , and c are constants fulfilling the condition

$$a + b + c = 0 \quad (3.3)$$

and C is a global prefactor. Two configurations are often used to trap ions: The linear Paul trap with

$$a = 1, b = -1, c = 0 \quad (3.4)$$

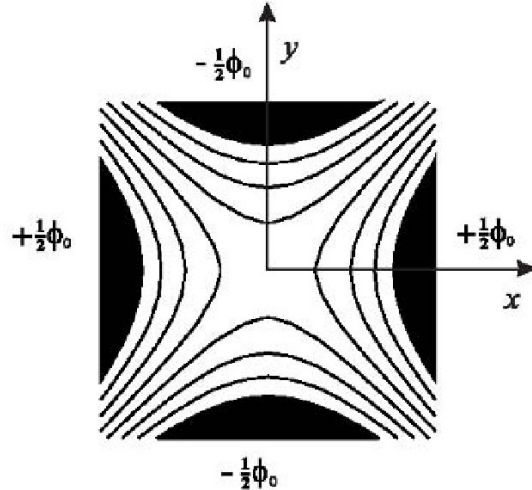


Figure 3.1: Potential of the linear Paul trap in the $x - y$ plane created by four hyperbolic electrodes. Figure taken from [13].

and the three-dimensional Paul trap

$$a = b = 1, c = -2. \quad (3.5)$$

In the case of the linear Paul trap, no potential is created along the z -axis (axial direction). The 3D-Paul trap is not further investigated since most of the traps used by our group are linear Paul traps. More on the 3D trap can be found in ref [13]. Four electrodes separated by a distance $2r_0$ create the potential along x and y (radial directions), which is given as

$$\Phi(x, y) = C(x^2 - y^2). \quad (3.6)$$

The two opposing electrodes are on the same potential $\pm\Phi_0/2$. The position of the electrodes and the created field is shown in figure 3.1. A positively charged ion is repulsed by the positively charged electrodes and attracted towards the negatively charged electrodes, confining the ion in one dimension and repelling it in the other. By changing the polarity of the electrodes, confinement in the second dimension is achieved, while the first dimension is now unrestrained. Confinement in both axes can be achieved by periodically switching the polarity of the electrodes. An applied static voltage U_{dc} is combined with an alternating voltage $V_{ac} \cos \omega t$ to switch the polarity, creating the potential

$$\Phi_0 = U_{dc} - V_{ac} \cos \omega t. \quad (3.7)$$

The frequency ω is the driving angular frequency. The motion in both axes has to have a stable amplitude, a growing amplitude causes a loss of ions over time. The Mathieu equations [13], derived from the equation of motion, are differential equations used to calculate sets of parameters resulting in a stable motion of the ions. The Mathieu equations (here in 2D)

$$\frac{d^2x(\tau)}{d\tau^2} + (a - 2q \cos 2\tau)x = 0 \quad (3.8)$$

$$\frac{d^2y(\tau)}{d\tau^2} - (a - 2q \cos 2\tau)y = 0 \quad (3.9)$$

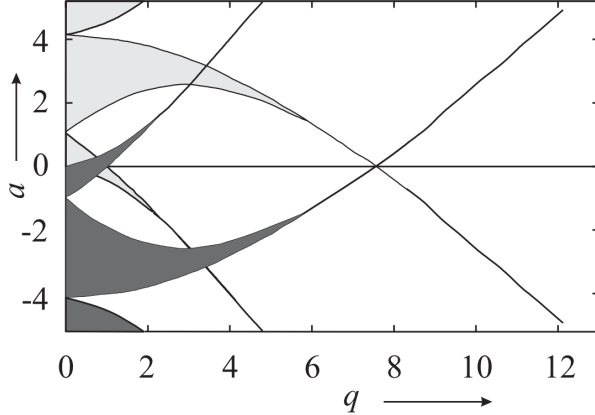


Figure 3.2: Stability diagram of the 2D Mathieu equations. Overlapping regions are stable in x- and y-motion. Figure taken from ref [13].

are commonly expressed using the dimensionless parameters

$$\tau = \frac{\omega}{2}t, \quad (3.10)$$

$$a = \frac{4eU_{\text{dc}}}{m\omega^2 r_0^2}, \quad (3.11)$$

$$q = \frac{2eV_{\text{ac}}}{m\omega^2 r_0^2}, \quad (3.12)$$

$$(3.13)$$

with e the electric charge and m the ion mass. The stable solutions of the Mathieu equations do not depend on the initial conditions of the ions but they depend only on the parameters a and q .

The solution of the Mathieu equations is often visualized in a so-called stability diagram, see figure 3.2. The shaded regions show where either the x-(light gray) or y-(dark gray) motion is stable. Both, the x- and y-motions, are stable in the region of overlap. A point in overlapping regions is used to calculate the trapping parameter. Additional confinement in the axial (z) direction is necessary to trap ions. Axial confinement can be achieved by adding additional dc electrodes along the z -axis. The linear Paul trap used in one of our experiments can be seen in figure 3.3. The electrodes needed for the quadrupole trap are formed by metal blades while the electrode tips (or endcaps) confine the ions in the axial direction. For example, a string of 6 calcium-40 ions is trapped in the trapping region and detected by a CCD camera. The following chapter explains how manipulation and detection of these ions is implemented.

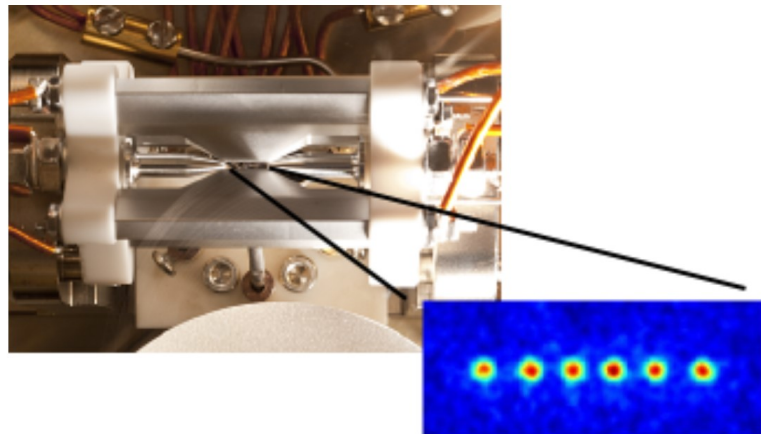


Figure 3.3: Linear Paul trap. In the insert 6 trapped ions are displayed.

3.2 Level scheme of ionized calcium 40

In our experiment, the single ionized form of calcium 40 is used. Calcium is part of the alkaline earth metal group, having two valence electrons. One way of ionizing calcium 40 is photoionization. Single ionizing the atom using one laser is inconvenient since the necessary wavelength to remove the electron is far in the ultraviolet regime (203 nm). Only lasers with special optics and coatings can create the necessary wavelength. Instead, two lasers overlapped on the trapping zone are used to photoionize calcium 40: one laser beam at a wavelength of 423 nm excites one of both valence electrons to the $3p^64s^4p$ state. This state is chosen since it can be reached from the ground state and the required lasers are commercially available. A second laser operating at 375 nm separates the excited electron from the atom.

In figure 3.4 the levels used by our experiments are shown. Note that calcium 40 has no hyper-fine structure. The key states of $^{40}\text{Ca}^+$ within the scope of our experiments are the ground state $S_{1/2}$, the excited states $P_{1/2}$ and $P_{3/2}$ and the metastable $D_{3/2}$ and $D_{5/2}$ states. The transition between the ground state and the $P_{1/2}$ state is used for multiple purposes, such as Doppler cooling the ion and measuring the qubit state. The detection used in our experiments is fluorescence detection. Photons with an energy corresponding to the wavelength of 397 nm are scattered if the 397 nm laser is able to drive the dipole transition between the $S_{1/2} \leftrightarrow P_{1/2}$ states. These scattered photons are detected by a photomultiplier tube and/or a CCD camera. If photons are detected the ion is 'bright'. In our setups, the CCD camera is used in the case multiple ions are trapped since it can resolve the spatial distribution of the ions. A string of ions detected with a CCD camera is shown in figure 3.3. In the case where neither the $S_{1/2}$ nor the $P_{1/2}$ is populated the 397 nm laser is not able to drive the transition between both states and no photons at 397 nm are scattered. The ion is 'dark', it can not be detected using the photomultiplier tube or the CCD camera.

The $P_{1/2}$ state has a nonzero probability to decay into the $D_{3/2}$ state [32]. In our experiment, this decay reduces the efficiency of cooling and detection since it prevents the scattering of 397 nm photons while the population is in the $D_{3/2}$ state [33]. A laser operating at 866 nm drives the transition $P_{1/2} \leftrightarrow D_{3/2}$ to prevent trapping the population in the $D_{3/2}$ state. This laser is referred to as repump laser.

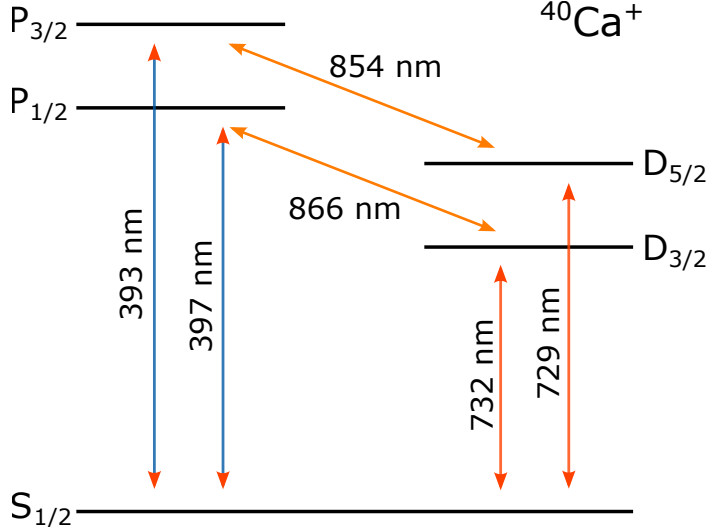


Figure 3.4: Simplified energy level structure relevant for this work. The transitions between the ground state $S_{1/2}$ and the excited states $P_{1/2}$ and $P_{3/2}$ and between the P states and the D states are electric dipole transitions while the transitions between the D states and the ground state are electric quadrupole transitions [31].

In our experiments the quadrupole transition between the ground state and the metastable $D_{5/2}$ state is used as a qubit transition. The transition wavelength between the ground state and the $D_{5/2}$ state is 729 nm . Since the transition between the ground state and the $D_{5/2}$ state is a quadrupole transition (it is dipole-forbidden), the metastable $D_{5/2}$ state is a long-living state. It has a lifetime of 1.2 s , which is 10^8 times larger compared to the lifetime of the $P_{1/2}$ state at 6.9 ns [33, 34]. Coupling the states $D_{5/2}$ and $P_{3/2}$ using a laser operating at 854 nm can be used to shorten the lifetime of the $D_{5/2}$ state. Therefore, it is used for e.g. sub-Doppler cooling techniques like sideband cooling. This laser is referred to as 'reset laser'.

3.3 Quantum bit, Bloch sphere, and gate operation

This section follows the 1st chapter of the book *Quantum Information, Computation and Communication* by Jonathan A. Jones and Dieter Jaksch [35]. In digital computing, the fundamental unit of information is given by the bit. The bit is a logical state whose value is often represented by the numbers 0 and 1. In quantum information, the quantum bit or short qubit is a way to replace the bit as the unit of computing. In contrast to the classical bit, the value of the qubit is not a binary number. It can take all possible combinations of

$$|\Psi\rangle = \alpha|0\rangle + \beta|1\rangle, \quad (3.14)$$

where α and β are imaginary numbers, and $|0\rangle$ and $|1\rangle$ are orthonormal states in a two dimensional Hilbert state. A common vector representation (computational basis) is in the Pauli z-Basis as:

$$|0\rangle = \begin{pmatrix} 1 \\ 0 \end{pmatrix}, |1\rangle = \begin{pmatrix} 0 \\ 1 \end{pmatrix}, \quad (3.15)$$

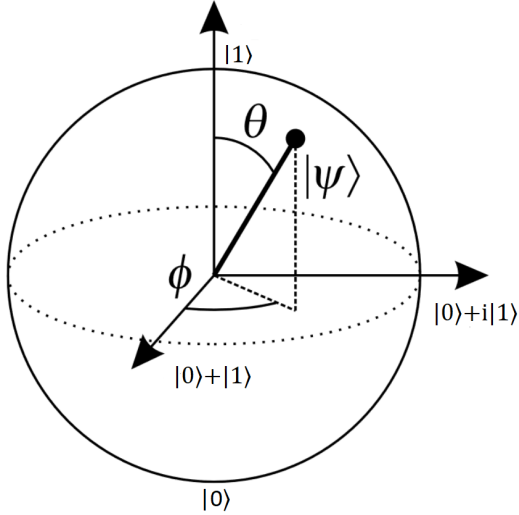


Figure 3.5: The Bloch sphere is used to represent the state of a qubit. The state Ψ is given by equation (3.17). The two states $|0\rangle$ and $|1\rangle$ lie on the two poles of the sphere.

while the so called 'bra' $\langle 0| = (\langle 0|)^\dagger$ is the matrix conjugate transpose of the corresponding ket [36]. The imaginary numbers α and β have to fulfill the relation

$$|\alpha|^2 + |\beta|^2 = 1. \quad (3.16)$$

The two cases $|\alpha|^2 = 1, |\beta|^2 = 0$ and $|\alpha|^2 = 0, |\beta|^2 = 1$ resemble the states 0 and 1 of the classical bit. All other possible solutions of relation (3.14) which fulfill equation (3.16) have no classical analogue and are superpositions of the two states $|0\rangle$ and $|1\rangle$. In the case that a pure quantum state $|\Psi\rangle$, defined in the Hilbert state $H = H_A \times H_B$, can not be separated, that means it cannot be written as a product of two states $|\Psi\rangle = |\Psi_A\rangle \times |\Psi_B\rangle$, the quantum state is entangled [37]. Entanglement means that a state can not be described independently from the other states.

One way of realizing a qubit with the help of trapped calcium 40 ions is to encode it into the electric states of the ion while the collective quantized motion of the ions in the trap allows to mediate entanglement between multiple qubits. The two orthonormal states $|0\rangle$ and $|1\rangle$ of the two-dimensional Hilbert state are typically encoded in the $S_{1/2}$ ground state ($|0\rangle$) and the $D_{5/2}$ excited state ($|1\rangle$). Lasers introduce coupling and entanglement between those different electric states and also the collective quantized motion, in case of entanglement between different qubits is needed.

An arbitrary pure single-qubit state may be graphically represented as a vector pointing on a sphere's surface, the so-called Bloch sphere. It is depicted in figure 3.5. The north and south poles of the Bloch sphere (on the z-axis) are typically assigned to the two states $|0\rangle$ and $|1\rangle$. The complex parameters α and β have to be rewritten in polar coordinates θ and ϕ converting equation (3.14) in

$$|\Psi\rangle = \cos(\theta/2)|0\rangle + \sin(\theta/2)e^{i\phi}|1\rangle, \quad (3.17)$$

where $e^{i\phi}$ is a local phase [36] to create the Bloch representation. The state of the qubit depends on the two angles $0 \leq \theta \leq \pi$ and $0 \leq \phi \leq 2\pi$ creating the surface of the sphere.

The operation acting on a quantum state is called gate operation. A quantum gate

3 Quantum information processing with trapped ions

is a unitary operation U acting on one or more qubits. In contrast to many classical logic gates, quantum gates are reversible [37]. The action of the gate U on a quantum state $|\Psi_1\rangle$, forming the result $|\Psi_2\rangle$, is given by

$$U |\Psi_1\rangle = |\Psi_2\rangle. \quad (3.18)$$

The operators U are described as unitary matrices relative to a given computational basis. Common gates are the Pauli-X,-Y,-Z gates; the CNOT gate, and the Hadamard (H) gate [37]. These gates are usually represented by the matrices:

$$X = \sigma_x = \begin{bmatrix} 0 & 1 \\ 1 & 0 \end{bmatrix} \quad (3.19)$$

$$Y = \sigma_y = \begin{bmatrix} 0 & -i \\ i & 0 \end{bmatrix} \quad (3.20)$$

$$Z = \sigma_z = \begin{bmatrix} 1 & 0 \\ 0 & -1 \end{bmatrix} \quad (3.21)$$

$$H = \frac{1}{\sqrt{2}} \begin{bmatrix} 1 & 1 \\ 1 & -1 \end{bmatrix} \quad (3.22)$$

$$CNOT = \begin{bmatrix} 1 & 0 & 0 & 0 \\ 0 & 1 & 0 & 0 \\ 0 & 0 & 0 & 1 \\ 0 & 0 & 1 & 0 \end{bmatrix} \quad (3.23)$$

The Pauli-X,-Y,-Z gates are single qubit gates and act as a rotation on the respective axis on the Bloch sphere. The Hadamard gate acts on a single qubit and maps the state $|0\rangle \rightarrow \frac{|0\rangle+|1\rangle}{\sqrt{2}} = |+\rangle$ and the state $|1\rangle \rightarrow \frac{|0\rangle-|1\rangle}{\sqrt{2}} = |-\rangle$, creating a superposition of $|0\rangle$ and $|1\rangle$. The CNOT gate is a two-qubit gate that flips the state ($|0\rangle \rightarrow |1\rangle$ or $|1\rangle \rightarrow |0\rangle$) of the second qubit if the first qubit is in the state $|1\rangle$. It is used to create and destroy entanglement.

A universal set of gates is necessary to perform any operation on a quantum computer [38]. It has the property that any unitary operation can be approximated with this universal set's final number of gates. An example of such a universal set of gates consists of Hadamard, CNOT, and $\pi/8$ gates [37].

Gates are susceptible to errors induced by the environment. Considering quantum information processing based on trapped ions, fluctuations in e.g. the magnetic or electric field of the trap or the intensity or phase of a laser induce an error in the gate. A measure to characterize the error of the gate is to calculate the distance between a gate U and the created quantum operation E depending on the input state ρ [39]. The measure of how close E and U are is called gate fidelity F . The fidelity for a unitary quantum operation U ($U(\rho) = U\rho U^\dagger$) and its implementation E , for a state ρ , is

$$F_{E,U}(\rho) = \left(\text{tr} \sqrt{\sqrt{E(\rho)}U(\rho)\sqrt{E(\rho)}} \right)^2. \quad (3.24)$$

A outcome of $F = 1$ means the states U and E are indistinguishable while $F = 0$ means fully distinguishability between both states [39].

Fluctuations in the intensity and the phase of a laser beam can limit the fidelity of quantum gates to $F < 1$ [40]. The evolution of the qubit on the Bloch sphere

3.3 Quantum bit, Bloch sphere, and gate operation

depends on the noise in the laser source. Frequency noise leads to unwanted rotations on the z-axis while intensity noise creates not wanted rotations around the x- and y- axis resulting in an imperfect overlap of the target state with the final quantum state [40]. The decrease in fidelity due to frequency fluctuations can not be reduced by narrowing the linewidth of the laser. The fidelity decay constant $X^{(u)}$ depends on the spectral overlap of the noise power spectral density with the filter function of the target operation u of duration τ [40], leading to a fidelity of

$$F^{(u)}(\tau) \approx 1 - \frac{X^{(u)}}{2}. \quad (3.25)$$

The fidelity decay can be reduced by the means of active stabilization of a finite bandwidth up to the limit given by spontaneous emission.

The fundamental limit for the intensity noise is given by the shot noise limit (SNL). The error induced by a laser running at the SNL is less than the error induced by spontaneous emission of photons and thus can be neglected [40]. A greater source of intensity noise may be intensity noise created by optical elements between the laser and the ion or by beam point jitter, reducing the fidelity of a gate operation.

A key problem for quantum information is the loss of quantum coherence, also called decoherence. Decoherence is composed of different physical effects like the thermalization of the states to equilibrium. One example of such an effect is the decay of the excited state into the ground state or the dephasing of the superposition of the qubit. The timescale of the decay process is defined by the longitudinal relaxation rate T_1 while the dephasing is defined by the transverse relaxation rate T_2 [37].

4 Design and installation of the rack mountable laser system

This chapter discussed the design process based on the set targets concerning high stability, space consumption, and maintenance cost. In the first section, the overall structure is reviewed while in the following sections, each part is evaluated in detail.

4.1 Rack structure

In one lab of our group, four different experiments are based on ionized calcium 40, namely the Linear Trap, AQTION, Big Cavity, and Fiber Cavity. Building the laser infrastructure for each experiment individually would consume multiple optical tables and disproportionately large expenditures while consuming only a fraction of the available power. One laser has sufficient power to operate all four experiments simultaneously. Therefore, the Linear Trap, the Big Cavity, and the Fiber Cavity share the same infrared, ionizing, and 397 nm lasers while AQTION is supplied by its own infrastructure [41].

The legacy setup for the 854 nm and 866 nm lasers is based on Toptica diode lasers mounted on an optical table. Multiple optical elements are used to split the lasers up into several paths, seeding a cavity, wavemeter, and experiments. Both the repumping and reset lasers and also the 397 nm laser are locked on the so-called quad-cavity. The quad-cavity unites four individual cavities on one spacer and is, therefore, able to lock the 397 nm, 423 nm 854 nm, and 866 nm lasers individually using separate piezo transducers for each wavelength. It is temperature stabilized and under vacuum to reduce environmental coupling. The laser frequencies can be tuned to the desired setpoints by changing the piezo voltages of the cavity. The laser frequency locked on the cavity is intentionally not identical to the ion transition frequency. AOMs in double pass configuration are used to match the laser frequency with the ion frequency. Every experiment has its own double pass for both the 854 nm and 866 nm lasers, shifting the frequency up by 400 MHz and controlling the amplitude of the laser light.

The goal of this work is to upgrade the setup of the 854 nm and the 866 nm lasers in frequency stability, space consumption, and output power while reducing maintenance effort and footprint reduction. The output power is increased to support up to six experiments. The new setup is rack-based to reduce the required footprint and complexity simultaneously. The rack is a standard 19 inch rack with dimensions $l \times d \times h = 800 \text{ mm} \times 800 \text{ mm} \times 47 \text{ rackunits(RU)}$ from NVent Schroff. One RU is 44.45 mm resulting in a total rack height of 220 cm including the base plate and roof. A rear and front door provides easy access. Sensitive devices are located at the bottom while electronics and less sensitive units are located towards the top section. The design of the rack is shown in figure 4.1 a).

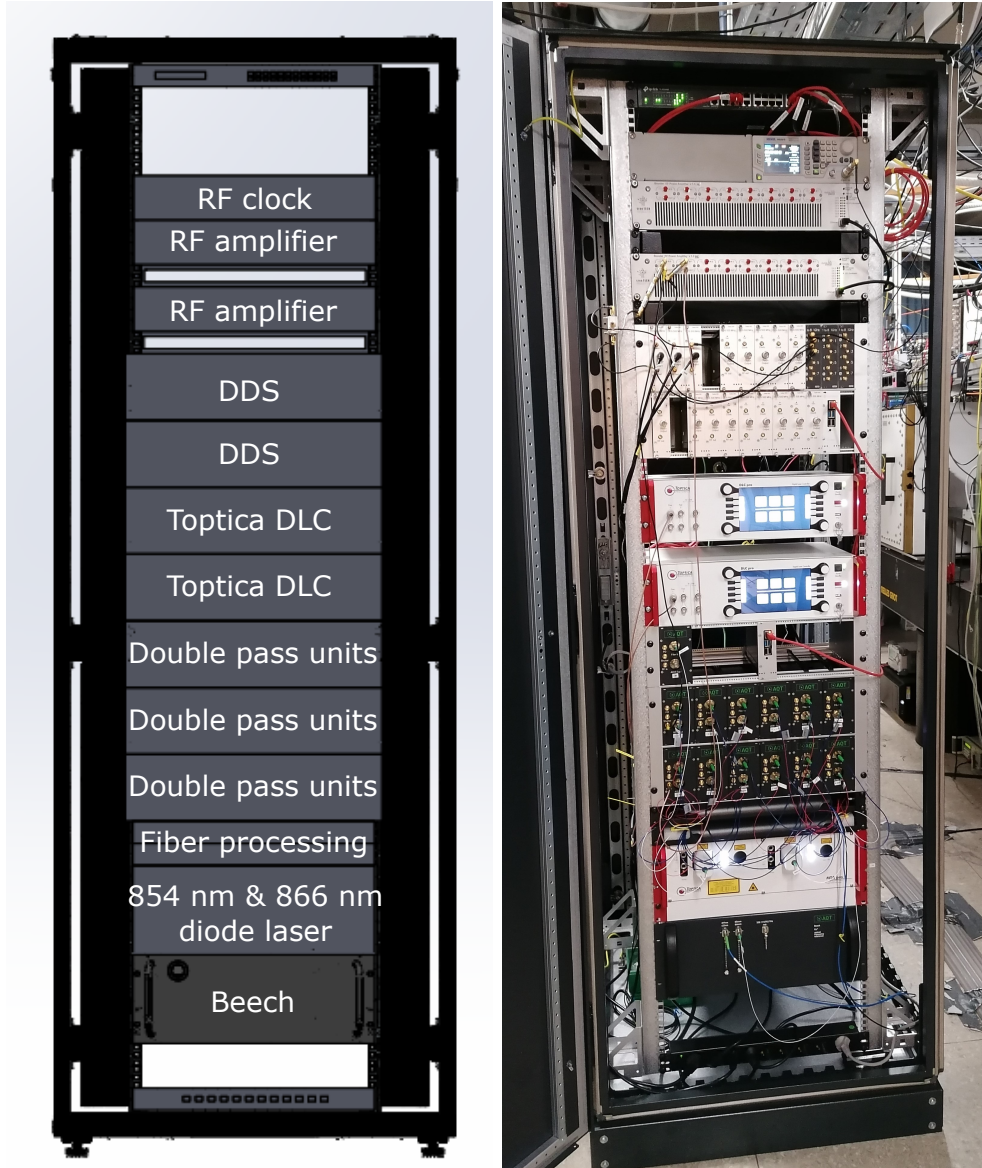


Figure 4.1: Schematic a) and actual b) rack. In b) the individual elements are spaced out to improve the airflow. The side walls are not mounted.

Temperature and mechanical stability of the rack

The position of the individual elements is based on their sensitivity to vibrations and temperature fluctuations. Elements located in the lower section of the rack experience vibrations with lower amplitude compared to elements in the top section and are provided with a steady stream of cold air. The air temperature increases in the vertical direction reducing the cooling effectiveness. Two options are available to cool the rack: running it with open side walls or cooling it actively using a cooling compressor mounted at the rear door. The advantage of using active cooling is decoupling the rack from the environment. Temperature drifts inside the lab are compensated and prevent dirt from clogging fans and filters.

The internal rack structure based on sensitivity on temperature fluctuations and vibrations is as follows: The cavity used to stabilize the lasers, hereinafter referred to

4 Design and installation of the rack mountable laser system

as BEECH [42], sits at the bottom of the rack, receiving a steady stream of cold air, maintaining a constant temperature. Above the BEECH both lasers are installed. The Toptica MTA TA pro unit provides the 854 nm and the 866 nm light. It is driven by two DLC pro units, located further up inside the rack. One empty height unit is located in between the laser and the BEECH to provide a steady stream of cold air. The optics used to split the light into several paths and manipulate the amplitude and frequency are directly located above the lasers inside the so-called fiber processing elements and double pass units. The BEECH, MTA TA pro unit, the fiber processing elements, and the double pass units contain laser optics, while all other elements are devices operating and controlling the lasers and the modulation of the laser light. The direct-digital-synthesis (DDS) units combined with the rf-amplifier provide the rf-signal driving the AOM inside double pass units. An Ethernet switch provides remote access to the BEECH, DLC pro units, rf-amplifiers, and DDS units. A picture of the setup is shown in figure 4.1 b).

Lab and equipment safety

One concern is to protect the people inside the lab from possible hazards like scattered light or high voltage/current while protecting the devices from the environment. The rack is equipped with walls and a rear and front door to fully cover it up, decreasing the likelihood of emitting stray light and avoiding possible contact with live cables. The whole rack is fiber-based to further reduce possible light scattering and reduce maintenance work. The rack is splashproof and behaves as a Faraday cage, shielding the interior from electromagnetic radiation. Additional struts ensure increased stability (earthquake-proof up to a load of 800kg) and diminish vibrations.

4.2 Diode laser

The laser module used inside the rack is the MTA TA pro module produced by Toptica. It consists of one element containing both, the 854 nm and the 866 nm, lasers, and two DLC pro control units, one for each laser. The MTA TA pro is an external cavity diode laser, stabilized via the Littrow 2.1.1 setup. Wavelength selection is provided via a combination of temperature, current, and piezo voltage control. Coupling inside the MTA TA pro is based on automated mirrors, reducing the maintenance effort. The MTA TA pro unit combines each laser with a tapered amplifier (TA) increasing the output power from approximately 50 mW to above one Watt (fiber coupled - class 4 laser). The laser parameters are given in table 4.1. Note that the piezo voltage depends on the environment and may change over time.

laser	ν_{ion} (THz)	ν_{laser} (THz)	$\nu_{\text{ion}}-\nu_{\text{laser}}$ (MHz)	T (°C)	I (mA)	U_{pz} (V)
854 nm	350.862 999	350.862 574	425	20.3	82.2	79.64
866 nm	346.000 380	346.000 754	-374	20.9	84.9	62.52
laser	I_{TA} (A)	T_{TA} (°C)	output power (W)	output power fiber (W)		
854 nm	4.18	25	3.05	1.2		
866 nm	4.25	25	3.3	1.0		

Table 4.1: Electric transition (ion) and laser parameters.

4.3 Frequency stabilization - BEECH cavity



Figure 4.2: Front plate of the MTA TA pro laser module and the BEECH reference cavity with their respective fiber docks.

4.3 Frequency stabilization - BEECH cavity

An external cavity is used as a feedback mechanism to stabilize the diode lasers. The BEECH [42] is able to lock the 397 nm, the 423 nm, the 854 nm, and the 866 nm lasers simultaneously. It has two fiber inputs one for 397 nm & 423 nm and one for 854 nm & 866 nm. The front plates of the BEECH and of the Toptica MTA TA pro laser unit are shown in figure 4.2.

In our experiment the 423 nm laser is not locked on a reference, it is swept over a frequency range. The 397 nm, 854 nm, and 866 nm light is combined inside the BEECH via a dichromatic mirror and sent on the cavity. The cavity has a length of 10 cm resulting in an FSR of ≈ 1.5 GHz. Locking light with different frequencies on the same cavity allows only certain possible cavity lengths, where the phase condition (2.1) is fulfilled for each frequency. The cavity length has to be an integer multiple of each laser frequency, such that standing waves for all given frequencies are possible. Cavity lengths fulfilling the phase condition for the 397 nm, 854 nm, and 866 nm lasers are named *lockpoints*. Potential lockpoints can be found via simulation by taking the ion frequencies, the center frequency of the AOM, and its detuning range into account. AOMs with higher center frequencies are favored since the bandwidth increases with the center frequency.

The lockpoint used in this setup has the following properties: The cavity temperature is ≈ 30.65 °C and the laser frequencies are 346.000 632 THz (866), 350.862 446 THz (854), and 755.222 479 THz (397). Both AOMs for the infrared lasers have a center frequency of 200 MHz with a tuning range of ± 10 MHz. The AOM for the 866 nm laser shifts the light down by ≈ 193.2 MHz and 854 nm laser shifts the light up by ≈ 204 MHz to match the transition frequency of the ion. The lockpoint for the 397 nm laser is identical to the lockpoint used by the legacy setup, operating at

4 Design and installation of the rack mountable laser system

755.222 479 THz and upshifted by a double pass unit operating at 125 MHz. The 0th order is used for recrystallization and loading while the 1st (upshifted) order is used for cooling.

The lasers are locked using the PDH scheme 2.2.2. Two feedback signals stabilize the laser on the given frequency. The fast input is a laser current modulation directly applied to the laser head. The slow feedback changes the piezo voltage to counter e.g. temperature and pressure drifts and is connected to the DLC pro by the means of analog remote control (arc). The correct setting of the arc depends on the laser type and the locking mechanism.

The BEECH requires an input power of $\approx 120 \mu\text{W}$ (infrared lasers) to create the optimal PDH error signal. Exceeding this threshold saturates the photodiode and may cause damage to several parts whereas falling below it decreases the signal-to-noise ratio, decreasing the lock stability. The error signal of the PDH setup is visualized via a virtual oscilloscope and/or spectrum analyzer included in the BEECH. Both devices can be used to optimize the PID parameters improving the lock quality and frequency stability. In figure 4.3 a) the PDH error signal of the 866 nm laser is shown (in red). The laser frequency is scanned over the cavity resonance to create the error signal. The laser frequency is varied by changing the piezo voltage triangularly (green curve), controlling the external cavity length of the laser. The shown PDH error signal is the error signal for high modulation frequency (compare equation (2.23)). Figure 4.3 b)

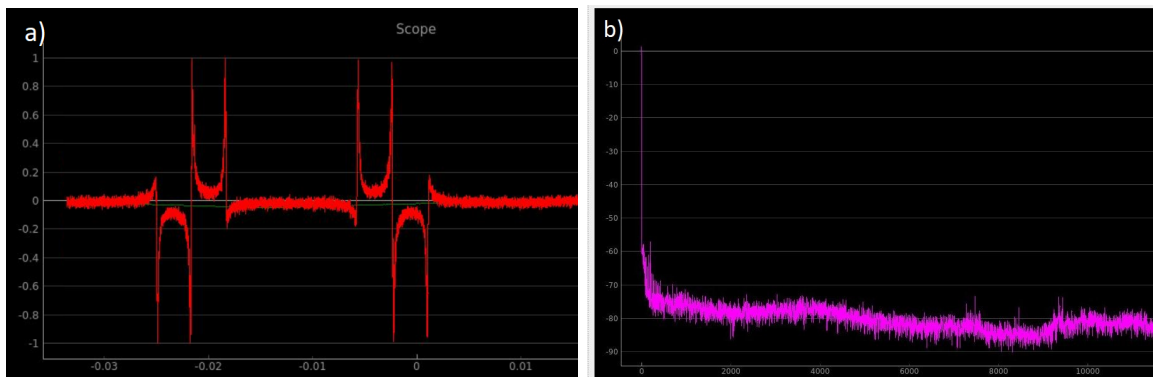


Figure 4.3: a) The size of the PDH error signal (red) depends on the laser power, PID gain, and design choices of the BEECH. The laser is scanned over the resonance creating the error signal. The scan voltage is shown as green triangular voltage (barely visible due to its amplitude of 0.1 V). b) The lock parameters can be improved using a frequency analyzer. The noise is reduced to its minimum while oscillations are suppressed. The spectrum may look different for different lasers.

shows the PDH error signal of the locked laser in the frequency space recorded with the spectrum analyzer. A spectrum analyzer is used to determine oscillations in the error signal, which reveal themselves as peaks in the frequency space. A change in lock parameters increases/reduces the PID response in a certain frequency range and can suppress noise and resonances like 50 Hz noise created by the power supply, or cavity resonances. Decreasing the gain of the PID or changing the cutoff frequencies of different PID stages may reduce oscillations. The goal is to reduce noise and avoid oscillations in the error signal.

The controller of the BEECH is a Next Unit of Computing (NUC). It hosts the control

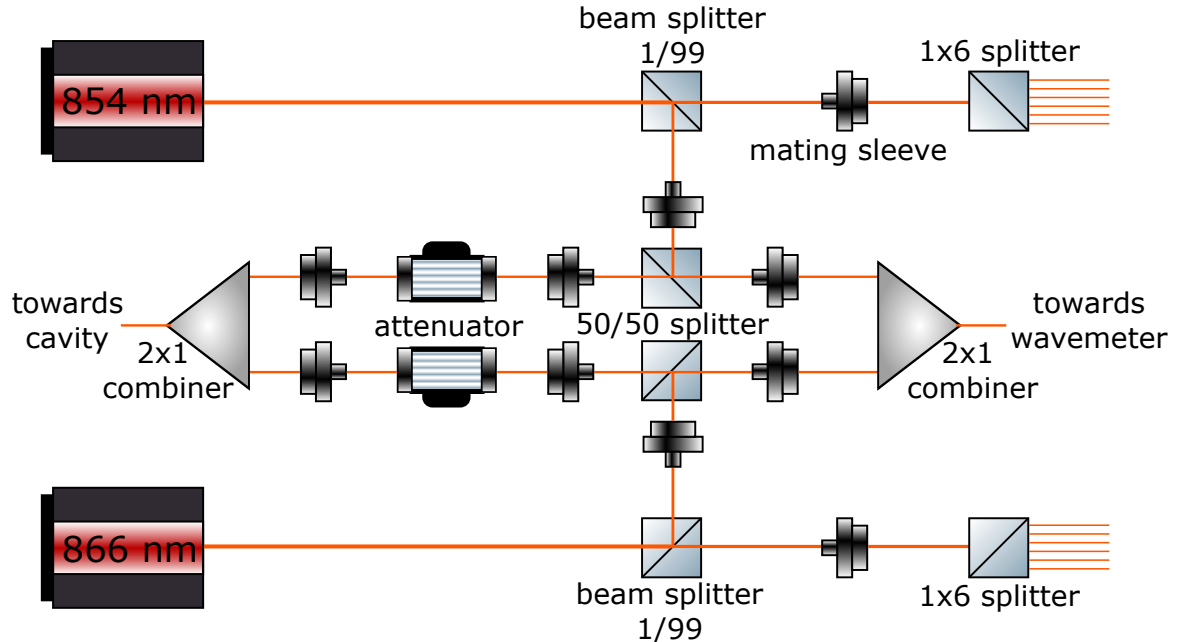


Figure 4.4: Both lasers are split up into several paths seeding the wavemeter, BEECH, and double pass units. All elements are fiber-based.

software and acts as a connection between all parts needed to run the BEECH. The control software is based on a locally hosted web interface, providing access to the lock parameters, an oscilloscope, a spectrum analyzer, and further in-depth settings.

4.4 Distribution of laser light

The main laser beam is split up into several beams with different intensities supplying the BEECH and the experiments with light. A free space solution and a fiber-based solution were considered, both having their advantages and disadvantages: The fiber-based setup reduces maintenance by reducing coupling and is more resistant to vibrations compared to the free space setup. In addition, fiber-based elements may be more compact regarding space as their free space counterparts and are advantageous in guiding light in tight setups compared to guiding free space beams by the means of mirrors. Furthermore, all components are provided by multiple companies, are quickly replaceable in case of failure, and increase the safety of the setup by not scattering light unintentionally.

The drawback of using a fiber-based setup is increased losses in polarization extinction ratio (PER) and power compared to the free space setup. The PER is typically limited to around 20 dB due to the used fibers and mating sleeves¹. Mating sleeves reduce the power by 3-10% (measured in this setup) due to misalignment of the cores of the fibers. All components except those going towards the wavemeter are polarization-maintaining elements and are located in the two drawers named 'fiber processing' in figure 4.1. A schematic of the setup is shown in figure 4.4. The laser light provided by the 854 nm and 866 nm lasers is split up into two paths for each laser via a 1x2 fiber splitter²,

¹Thorlabs PM mating sleeve ADAFCPM2

²Agiltron FC-P82211313, 1x2 PM850 FC/APC, 1/99, min PER 20.8 dB

4 Design and installation of the rack mountable laser system

seeding the BEECH and the wavemeter. 1% of the light in the main beam is deflected towards them since they only need tenths of milliwatts to operate. The remaining 99% are split up equally by a 1x6 beamsplitter³ and are connected to the double pass units. The power in each outgoing path is reduced by 10 dB⁴ compared to the incoming power.

The path towards the cavity and the wavemeter is split equally by the means of another 1x2 fibersplitter⁵. A 2x1 non-polarization maintaining micro-electromechanical system (MEMS) fiber switch⁶ is used to connect the lasers to the wavemeter. It assures that only one laser at a time is on the wavemeter. The fiber switch is controlled via a Raspberry Pi. A python (and flask) based website hosted on the lab computer controls the Raspberry Pi and therefore the fiber switch via transistor-transistor-logic (TTL).

The wavemeter is located outside the rack, connected via a 15 m long multi-mode fiber to the switch. It has a maximum input power of 5 mW in all wavelengths. In case the power exceeds the damage threshold a mechanical attenuator⁷ can be installed.

The second output of the beamsplitter is sent to the cavity. The BEECH needs both lasers combined in one fiber with a power of $\approx 120 \mu\text{W}$ in horizontal polarization. Lower power reduces the signal to noise of the error signal and thus decreases the stability of the system while too high power may cause damage to the BEECH. A mechanical attenuator is installed in both arms controlling the power toward BEECH. It has a variable attenuation range of 0.1 dB – 40 dB.

4.5 Double pass units and control electronics

All fibers coming from the 1x6 splitters in the fiber processing setup (see figure 4.4) are connected to individual double pass units. A total of 12 double pass units are necessary. The double pass units serve two main purposes: They function as a switch for the laser light and they are used to fine-adjust the power and laser frequency to match the transition frequency on the ion. Furthermore, they assure that the ion transition frequency and the laser frequency do not have to be the same. Figure 4.5 shows a 3D drawing of a double pass unit. The fiber containing the 854 nm/866 nm light is connected to the Schäfter+Kirchhoff fiber coupler and collimator⁸, coupling the light from the fiber to free space. A half-wave plate is used to align the polarization of the light maximizing the reflection on the following polarizing beam cube. The reflected light traverses an AOM⁹, which is set up to maximize the power in the first order. The zeroth order is blocked since it is unused for the infrared lasers. The first order is focused on a rear mirror using a lens, reflecting the first order back into the AOM. The lens increases the robustness of the rear mirror against vibrations and

³Haphit FPFM-850-1X6-H5P01-2220-FC/APC, Center wavelength 850(15) nm, 10.1 dB input → output, fast axis blocked

⁴9 dB are necessary to split the light up into 6 paths while 1 dB account for the input loss and coupling efficiency.

⁵Agiltron FC-P82291313, PM850 FC/APC, min PER 21 dB, 50/50 splitting, IL 3.5 dB

⁶Photonwares FFSW-123840313, PM850 FC/APC, 0.28 dB loss, ER 24 dB, TTL 1 : 0 V, 2 : 4.5 V

⁷Agiltron Fiber-to-Fiber VOA, MVOA-111838313, IL 0.1 – 40 dB, PM850 FC/APC

⁸S+K 60SMS laser beam coupler, pm, FC/APC, 850 nm

⁹G&H AOM 3200-1214, center frequency 200 MHz, bandwidth 50 MHz

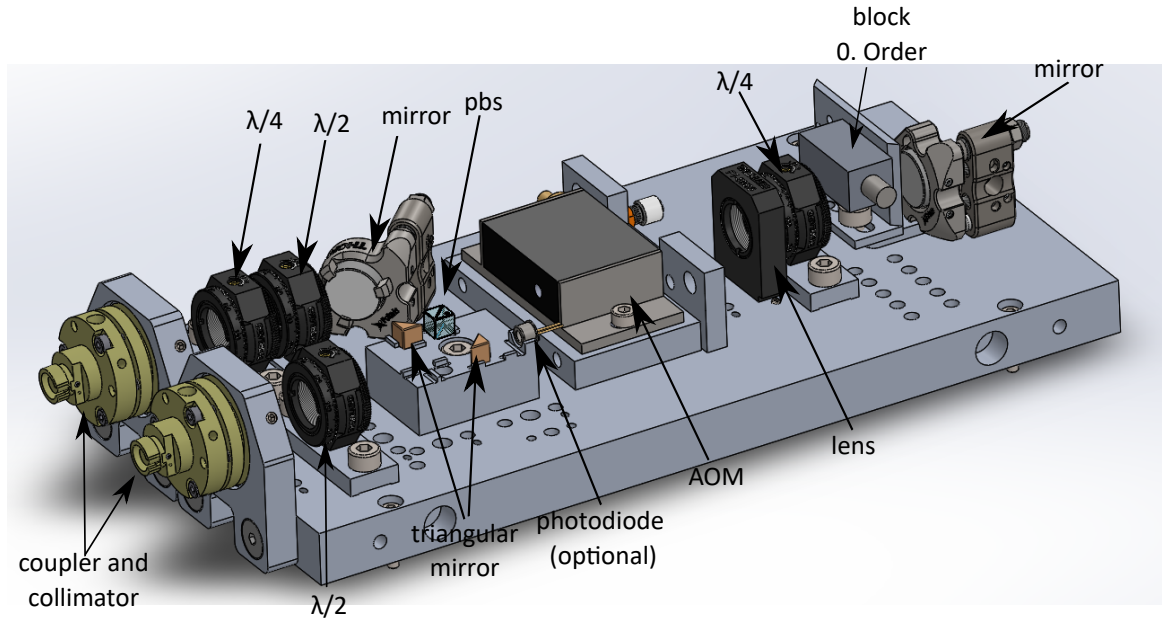


Figure 4.5: 3D drawing of a double pass unit. Design by Alpine Quantum Technologies.

misalignment. A quarter-wave plate is installed to rotate the polarization of the light by 90° in total, allowing the light to pass through the polarizing beam cube with minimal reflection. The rear mirror is set up to increase the power in the first order while passing the AOM a second time, shifting the frequency a second time in the same direction. The first order is coupled in a fiber via the S+K fiber coupler. A half-wave plate and a quarter-wave plate are installed to match the polarization of the light and the polarization of the fiber. In case an experiment needs 854 nm and 866 nm light in one fiber, an additional fiber coupler is installed behind one 854 nm double pass and one 866 nm double pass unit. 50% of the power is lost due to the combiner since the polarization of both beams is required identical. A schematic of the setup is shown in figure 4.6. Another possibility is to send the light in different fibers to the experiment, avoiding the losses due to the fiber coupler.

The AOM inside the double pass unit is controlled by a system called Raspbuddy. It consists of a direct digital synthesis (DDS) unit controlled by a Raspberry Pi 8.1 and a TTL signal sent by the experiment software. The TTL signal triggers an internal attenuator (minimum 30 dB) switching off the DDS. The DDS provides an rf-signal with adjustable power, frequency, and phase. A schematic of the setup is shown in figure 4.7.

An Euro rack mountable EA PS 800-80 power supply is used to provide power for the DDS unit as well as for the Raspberry Pi. The clock for the DDS is an rf-generator Rigol DSG 815 running at 800 MHz and -1 dBm . For each 854 nm double pass unit two DDS are necessary and for 866 nm one DDS is required. The reason for using two DDS per AOM is that two different power levels of 854 nm laser light are required by the experiment¹⁰ and switching rf-power by switching DDS via TTL is faster than switching the rf-power of one DDS via Ethernet and the Raspberry Pi. The signals created by both 854 nm DDS units are combined using a rf-combiner¹¹. The rf-signal

¹⁰For example, two different rf-powers are needed to run efficient sideband cooling.

¹¹Mini-Circuits 1x2 splitter, ZFSC-2-2-S+, 10 – 1000 MHz

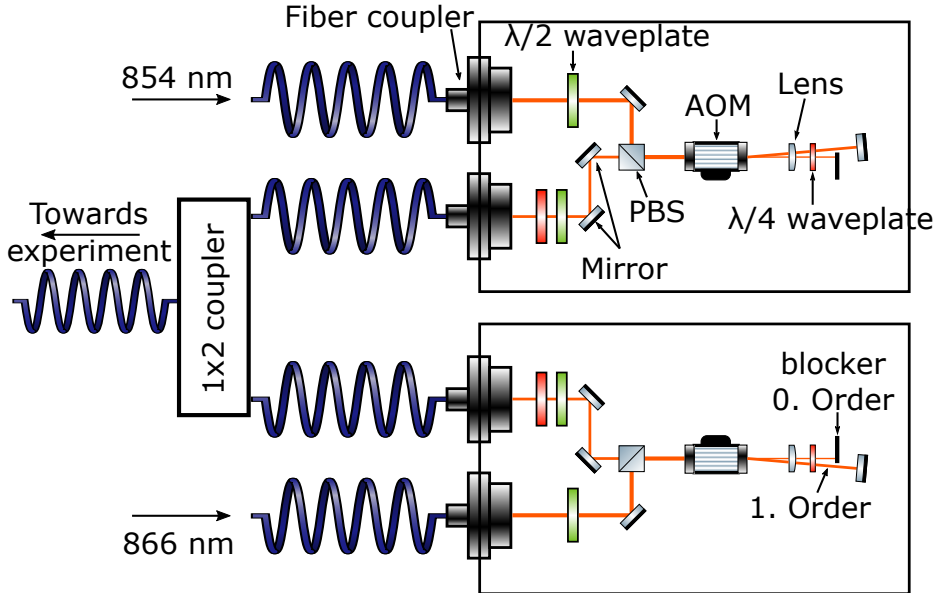


Figure 4.6: Two double pass units are combined via a fiber 1x2 coupler to provide 854 nm and 866 nm light in one fiber.

created by the DDS is amplified by 30 dB and sent to the double pass unit.

In the setup, a total of 18 DDS units are used, mounted in two Euro racks and connected via a back plate. The power supply is mounted on the rear side of the rack and is connected via cables to the back plate. In case all DDS units are running up to ≈ 12 A are applied. The Raspberry Pi driving the DDS units is installed in the same Euro rack as the DDS units, controlling them via BUS¹². The Euro rack is located directly above the DLC pro unit controlling the 866 nm laser 4.1.

The rf-clock can seed up to 22 devices due to three in-series connected 1x8 active rf-splitters. Inside an rf-splitter the signal is amplified by 10 dB before splitting, compensating for the splitting reduction of ≈ 10 dB. The amplifier of the DDS output signal is the so-called BOOSTER¹³. It is a remote-controllable 8-channel amplifier designed for high linearity. Two BOOSTERS are installed to amplify the rf-signal for all 12 double pass units. In case of a failure or too high input power (max input power 6 dBm), an interlock is opened and thereby preventing lab equipment damage. Resetting the interlock may be done remotely or by pressing a button on the BOOSTER. The output signal of the BOOSTER is connected to the rf-input of the double pass units.

In this chapter the structure of the rack as well as the design choices of the single parts and their requirements were discussed. The rack is based on fiber-based elements to minimize space consumption and maintenance work while optimizing beam path lengths, stability, and simplicity. The heart of the rack is the Toptica MTA TA pro diode laser setup and the BEECH-cavity, providing and stabilizing the laser light. As in section 4.1 stated, the rack can support up to 6 calcium 40 experiments with infrared light simultaneously, while each experiment can fully control the frequency, phase, and amplitude of their light. In the following chapter, the characterization of

¹²Communication system to transport data between components of a computer.

¹³Createch BOOSTER, 8 channel amplifier, up to 5W power, High linearity [43]

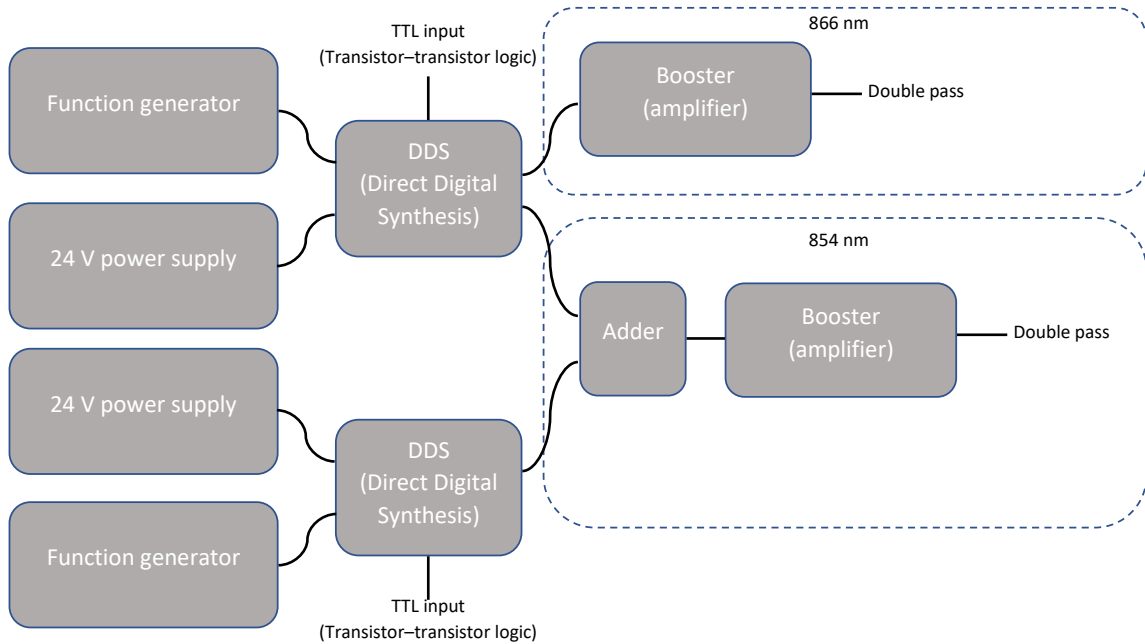


Figure 4.7: Schematic of the rf-setup used to drive the AOM inside the double pass unit. The rf-output of the DDS is switched on/off by a TTL input controlled via the experiment control.

the system is evaluated.

5 Characterization of the rack-system

In the previous chapter, the experimental layout and design principles were discussed. The scope of this chapter is to characterize and compare the rack-based setup to the legacy system.

5.1 Characterization of the lasers and BEECH

One requirement of our experiments is to have frequency-stabilized lasers. In this section, the frequency stability of the infrared lasers is investigated. The characterization aims to investigate the lock quality, the linewidth of the lasers, and the long-term stability. The quality of the lock influences the linewidth of the lasers and the period until the lasers unlock from the cavity. Using the BEECH combined with the Toptica MTA TA pro module, a laser linewidth in the range of 100 kHz and a lifetime of the lock of one month is expected. The lifetime of the lock is limited due to fluctuations in the environment like air pressure and room temperature changes. The drifts cause the lasers to drift out of the controllable range.

Two key parameters of the locked lasers are the short-term stability (seconds to minutes) and the long-term stability (hours to days and months). A beat with the legacy, free space system mounted on the optical table is carried out to measure the short-term stability of the rack-based laser system. Both laser systems are locked on their respective cavities. The cavities do not lock the lasers on the same frequencies. In the case of the legacy system, both lasers are locked 400 MHz below the ion transition while for the rack system, the 854 nm laser is locked \approx 425 MHz below it and the 866 nm laser is locked \approx 374 MHz above the ion transition. The light of the legacy system is not shifted during this measurement while the rack-based setup is up-shifted by 400 MHz for the 854 nm laser and down-shifted by 400 MHz in case of the 866 nm laser, resulting in a beat with a differential frequency of \approx 400 MHz. A photodiode S5973¹ with a self-made amplifier is used to record the beat. The data of the beat is shown in figure 5.1. The beat is averaged 10 times to increase the signal-to-noise ratio. The distance between both lasers in frequency space and the FWHM of the beat is received by fitting the beat signal with a Lorentzian² curve

$$f(x) = \frac{A}{\pi} \frac{\gamma}{(x - x_0)^2 + \gamma^2} + c \quad (5.1)$$

where A is the fit amplitude, γ is the FWHM, x_0 difference in absolute frequency between both lasers, and c is the noise floor. The FWHM of the 854 nm beat is

¹Hamamatsu photonics, 1 GHz bandwidth, 320 – 1000 nm

²The Lorentzian is used to model the beat linewidth. It may not be the exact model since the gain profile of the laser is not exactly Lorentz-shaped, but an upper limit to the bandwidth of the beat and the lasers is derivable.

5.1 Characterization of the lasers and BEECH

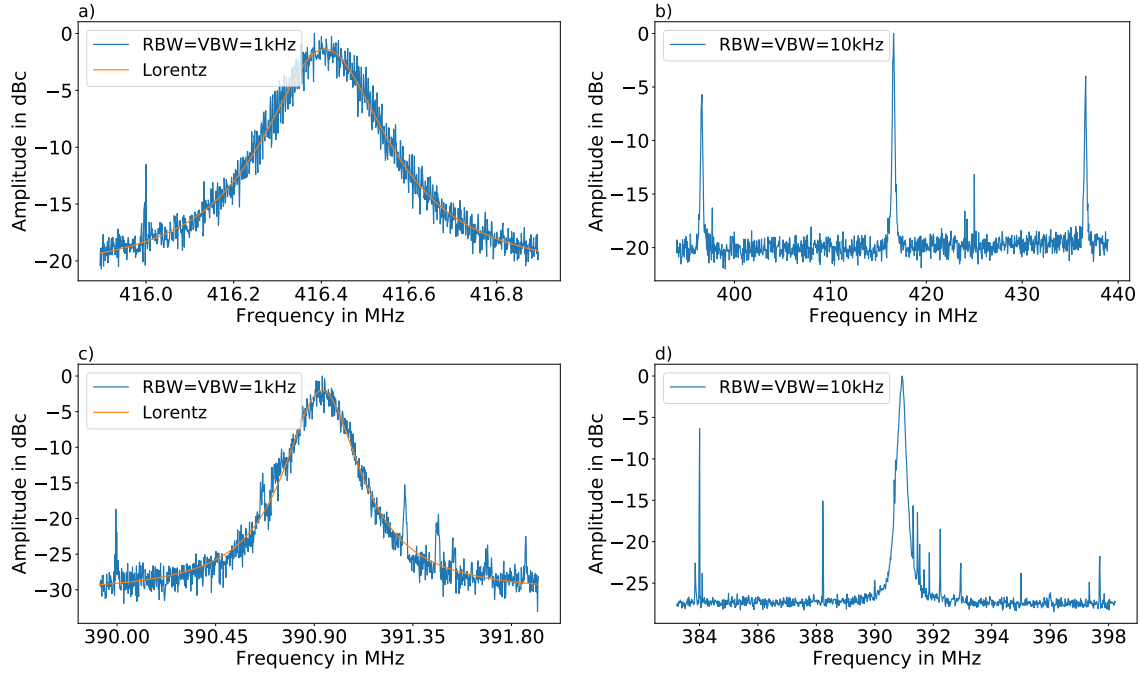


Figure 5.1: Figure a) shows the beat between both 854 nm laser systems. It is fitted using a Lorentzian curve. The frequency distance between both lasers is 416.4082(7) MHz and the beat has a FWHM of 177(2) kHz. b) Two sidebands are visible, located at ± 20 MHz around the carrier. These sidebands are modulated on the legacy 854 nm laser. The remaining peaks are electric signals picked up by the photodiode or amplifier. c) A beat between both 866 nm lasers. The distance between both lasers is 390.9352(14) MHz with a FWHM of 217(3) kHz. d) No sidebands are modulated on both 866 nm lasers. Testing of the photodiode reveals that the residual peaks are created by the photodiode or amplifier.

$\gamma = 177(2)$ kHz. The FWHM of the beat is an upper limit to the FWHM of the single lasers. A three-cornered-hat beat measurement (or a power spectral density measurement) is required to measure the FWHM of the individual lasers exactly, which was out of scope for this work due to technical and time constraints. No data on the linewidth of the legacy lasers locked on the quad-cavity is available, but it is expected that the linewidth of both lasers is of the same order of magnitude.

The beat of the 866 nm lasers visible in 5.1 c) is fitted with the same function (5.1) as in a). The FWHM of the beat is 217(3) kHz. The difference in the FWHM of the beats between the 854 nm and 866 nm lasers can be explained by different PID parameters. As for the 854 nm lasers, it is expected that the FWHM of the legacy and the rack-based 866 nm laser are of the same order of magnitude. The measured FWHM for both lasers matches the aim of achieving frequency stability of ≈ 100 kHz or better. The remaining peaks visible in figure 5.1 a)-d) are electric pickup signals collected by the photodiode or amplifier.

A beat measurement taken over multiple hours can be used to measure the long-term stability of both lasers. In the ideal case, the FWHM does not change and the beat is drifting with the same speed as the difference of the cavity drifts. The difference in the drifts can not be used to identify the drift rate of the single lasers. In the case both cavities are drifting in the opposite direction, the drift rate is increased while it is decreased if the cavities are drifting in the same direction. In the case the drift is the

5 Characterization of the rack-system

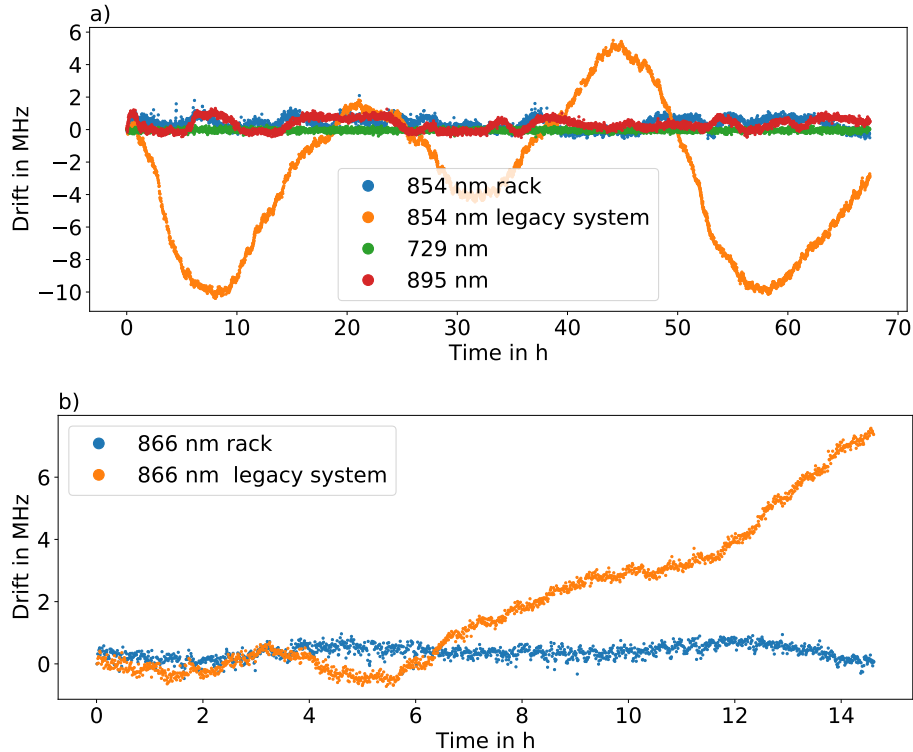


Figure 5.2: a) Laser frequency stability measurement over ≈ 70 h. The wavemeter is calibrated once a minute using the 729 nm qubit laser (green). A second reference laser at 895 nm is connected to test the accuracy of the wavemeter (red). The frequency stability of both reference lasers should be of the same order of magnitude since they are locked to atomic references. The legacy 854 nm is shown as an orange curve while the rack-based is the blue curve. b) Only the legacy 866 nm laser (orange) and the rack-based one are shown (blue).

same for both cavities, no total drift can be measured. The wavemeter WS8-2 from High Finesse is used to perform long-term stability measurements and can measure the drifts and absolute frequencies of the lasers individually. The drawback of using a wavemeter is a loss in accuracy and precision. While a beat measurement can resolve linewidths up in the millihertz region, the accuracy of the used wavemeter is limited to ± 2 MHz and the precision to 100 kHz. The fluctuations of the wavemeter in the ± 2 MHz range are dominated by daily temperature fluctuations and by the wavemeter drift. The wavemeter is auto-calibrated every minute using the 729 nm qubit laser that is stabilized on an atomic transition (compare figure 5.2, drift: 100 Hz/h - linewidth: ≈ 1 Hz [44]), to reduce the influence of the temperature fluctuations and the drift generated by the wavemeter itself. A second reference laser at 895 nm locked to a cesium cell is connected to the wavemeter. A stability measurement taken over ≈ 70 h is shown in figure 5.2 a). The 729 nm qubit transition laser is shown as the green line. It fluctuates by ± 100 kHz matching the precision of the wavemeter. No long-term drift is possible for this laser since the wavemeter is auto-calibrated on this laser every 60 s. A laser drift is converted into a wavemeter drift. The 895 nm reference laser locked on the cesium cell is shown as the red curve. The precision of the frequency measurement matches the wavemeter precision of 100 kHz but frequency

5.2 Characterization of the laser light distribution setups

drifts of ≈ 1.8 MHz are measured over a timescale of 4 h. Both lasers are expected to drift ≈ 100 Hz/h³ since they are locked on atomic references. The measured laser drift exceeds the individual cavity drifts by a factor of 10^4 . Any combination of the laser drifts is not sufficient to explain the measured drift, it is dominated by the drift of the wavemeter. The ≈ 1.8 MHz drift is an upper limit to the frequency stability of the laser. The actual value may be lower.

The rack-based laser is shown as the blue curve. It fluctuates by ≈ 1.8 MHz, similar to the fluctuation of the 895 nm reference laser, leading to an upper limit for the fluctuation. Since the BEECH is locked on the 895 nm reference it is expected that the laser fluctuations are below the measured ≈ 1.8 MHz and the fluctuations are dominated by the accuracy of the wavemeter. The legacy 854 nm laser is simultaneously measured on the wavemeter and is shown as an orange curve. This laser is drifting by ± 10 MHz/24h. The reason for this drift is not fully understood. The temperature, voltage, and current control of the cavity and laser do not show a similar oscillation in current/voltage. Comparing the drifts of both systems reveals that the legacy laser fluctuates more than five times as much as the rack-based 854 nm laser, reducing the amount of calibrations needed during an experiment run.

For the 866 nm lasers a similar behavior is expected since they are locked on the same cavities as the 854 nm lasers. A measurement over 15 h is shown in figure 5.2 b). The legacy 866 nm laser is shown in orange while the rack-based laser is shown as the blue curve. Since the 866 nm laser is locked on the same cavity as the 854 nm laser a similar drift as for the 854 nm laser is expected. The measurement shows a drift of 8 MHz for the legacy laser confirming the previous assumption. The fluctuation is less than 2 MHz for the rack-based setup, similar to the 854 nm laser.

In summary it is expected that the linewidth of both setups is of the same order of magnitude. A reduction of a daily drift from 10 MHz to below 2 MHz is expected using the rack system, increasing the stability of the experiment by at least 5 times.

5.2 Characterization of the laser light distribution setups

The quality of the lock depends on the stability of the power and the PER of the light heading toward the BEECH. Fluctuations in the laser light reduce the signal-to-noise ratio of the PDH error signal. In this section, the change in light power and PER is investigated individually for each component. The laser power is measured using a power meter⁴ and the PER using a Polarization Analyzer⁵. The polarimeter measures typical and minimum values of the PER. For these measurements the PER is given as the minimum PER measured by the polarimeter. The PER describes the optical power in one (wanted) polarization axis (+) compared to the unwanted axis

³The drift rate of the 729 nm laser was measured in [44] and the drift rate of the 895 nm laser is stated in [42].

⁴Thorlabs PM100D handheld optical power meter, sensor S121C, 400 – 1100 nm, $\pm 3\%$ uncertainty

⁵Schäfert+Kirchhoff Polarization Analyzer SK010PA-VIS, 450 – 800 nm, PER & DOP (degree of polarization) & SOP (state of polarization)

5 Characterization of the rack-system

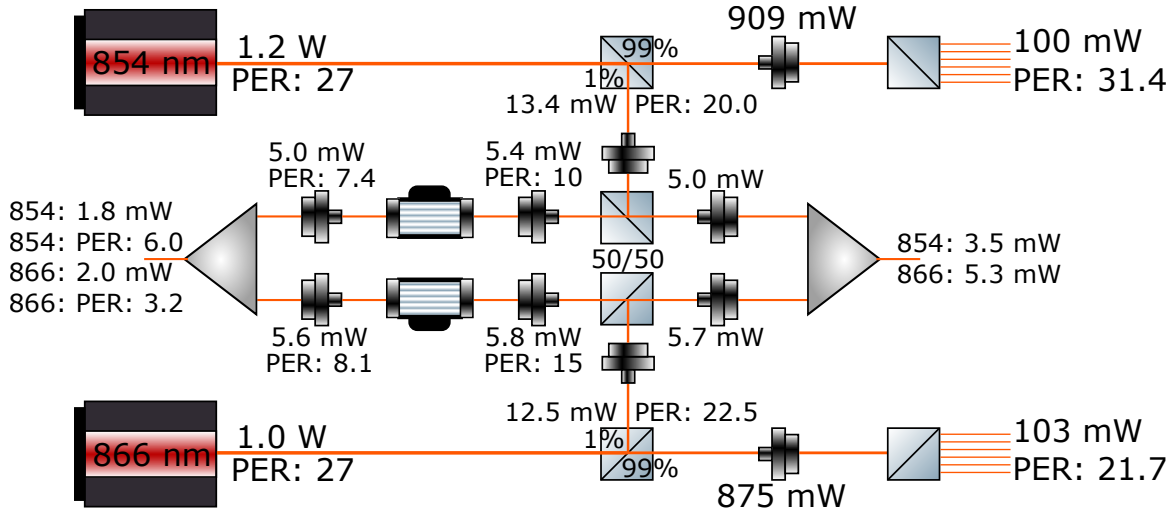


Figure 5.3: Characterization of the power and PER in dB. The given PER is the minimum value given by the polarimeter. Typical values may be up to twice as large. Note that the output power is different for different lasing modes. By changing the laser frequency, the output power of the laser may deviate from the given values.

(-). Here it is expressed on a logarithmic scale and defined as

$$\text{PER} = 10 \log_{10} \frac{P_+}{P_-}. \quad (5.2)$$

The setup with the corresponding measured values are shown in figure 5.3. Attaching multiple fiber-based elements and mating sleeves in series reduces the laser power and the PER towards the BEECH. On the path toward the wavemeter the PER is not measured because the wavemeter is not polarization dependent. The power heading towards the wavemeter and the BEECH exceeds the optimum power threshold intentionally and therefore must be attenuated. The reason for exceeding the power threshold is to not be limited in case the laser power decreases over time.

5.3 Characterization of the double pass units

The double pass units are directly connected to the 1x6 splitters and receive up to 100 mW of power (compare figure 5.3). Proper fiber coupling has to be ensured to prevent damage to the fibers or collimators. Typical coupling efficiencies and overall losses are shown in figure 5.4. Waveplates and mirrors reduce the laser power by less than 1% due to proper coating. Additional 4% are lost on the beam cube due to a finite PER of ≈ 20 dB (or 1%) and reflections. The used fibers limit the PER of the incoming light to ≈ 20 dB. A higher PER can be achieved by using different fibers. The AOMs have maximum diffraction (datasheet) into the first order of $\approx 90\%$ for 850 nm light. This maximum transmission can be reached in a single pass configuration. The second pass is reduced by an additional 10% to $\approx 80\%$ resulting in an overall efficiency of $\approx 72\%$ in double pass configuration. The largest individual loss factor of the double pass unit is coupling the light into the fiber heading toward the experiment. Using the S+K 60SMS couplers and collimators, 70-75% of the light can be coupled into the fiber. A total efficiency of 50% transmission can be achieved using these double

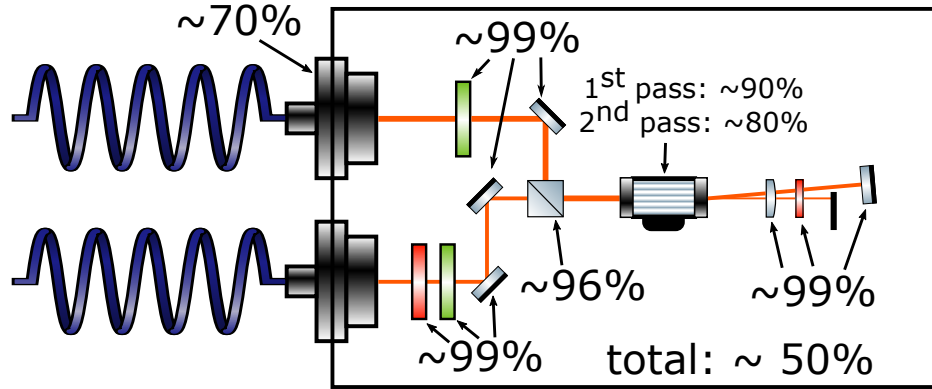


Figure 5.4: Measured coupling efficiency for a double pass unit. The total efficiency varies by $\pm 5\%$ between different double pass units.

pass units. These values are typical values due to imperfections in the individual components and the setup. The actual values of each double pass unit may differ by up to 5%.

The DDS controlling the AOM is operational between 50 – 500 MHz and can output an rf-power between 0 to -30 dBm. The DDS signal is amplified by additional 30 dB using the BOOSTER to drive the AOM. The AOM is set up to work at peak efficiency at 204 MHz (854 nm) and 192.3 MHz (866 nm). These frequencies are necessary to match the ion transition frequency. A key parameter is the bandwidth of the AOM and the dependence of the power on the rf-detuning since the laser frequencies can only be tuned via the AOM. A measurement of the bandwidth of the AOMs is shown in figure 5.5. In figure a) the dependence of the bandwidth on the rf-frequency is shown.

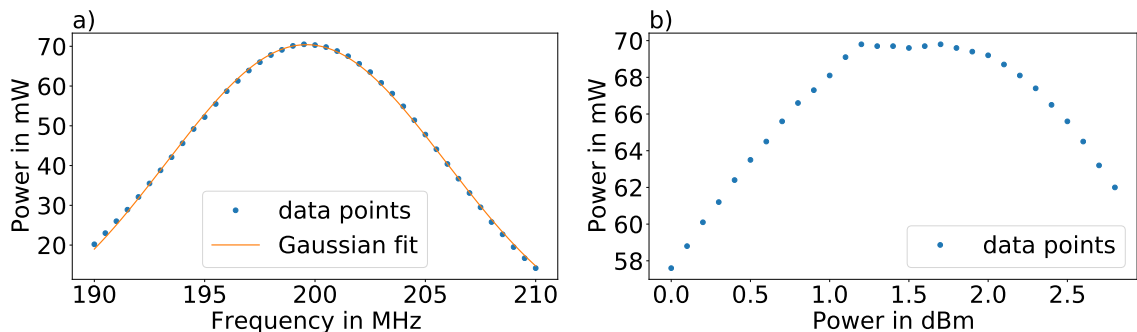


Figure 5.5: Deflected power in the 1st order depended on the frequency a) and on the rf-power b). a) The FWHM of the fit is 14.9(2) MHz. b) The rf-power is the output power of the DDS before the amplifier.

The AOM is set up to have maximum deflection into the 1st order at 200 MHz⁶ by adjusting the angle of incidence of the laser beam. The rf-frequency is varied by ± 10 MHz in 0.5 MHz steps. The measured data is fitted using a Gauss function (5.3) with A the amplitude, x_0 the expectation value, σ the standard deviation, and c the y-offset, to measure the bandwidth of the AOM.

$$f(x) = A \cdot \exp -\frac{(x - x_0)^2}{2\sigma^2} + c \quad (5.3)$$

⁶The AOM is set to 200 MHz to measure the bandwidth at its center frequency.

5 Characterization of the rack-system

An expectation value of $199.606(14)$ MHz and standard deviation of $6.34(9)$ MHz resulting in an FWHM of $14.9(2)$ MHz are measured.

The tuning range of the rack setup is reduced compared to the legacy system. The difference in both systems is that in the rack setup, the laser frequencies are shifted using the AOM while in the legacy system, the AOM operates at a fixed power (peak performance) while the cavity length is changed. The laser frequency can be shifted over several GHZ by changing the cavity length. Changing the piezo voltage is not possible for the BEECH due to locking multiple lasers at the same time on the same cavity. No shifts exceeding ± 10 MHz are expected due to the increased long-term stability of the system. Therefore, a tuning range of ≈ 15 MHz is sufficient. The maximum tuning range of the rf-power is limited by the minimum laser power required to run the experiment and the maximum laser power at peak efficiency and thus may differ from the FWHM. In figure b) the deflection into the first order depending on the rf-power is measured. The given rf-power is the output power of the DDS unit. The AOMs saturate between $1 - 2$ dBm, and more power leads to a reduction in diffraction efficiency. The rf-power should not exceed 2 dBm to prevent damaging the AOMs.

5.4 Measurements on the ion

The light is sent to the ions to check if the lasers and AOMs are working on the correct frequency and if the setup is working as intended. Multiple factors have to be considered to trap ions without changing the setup or the settings of the experiment: The frequency of the light has to match the ion transition frequency, the power has to be of the same order as for the legacy system ($\approx 80 \mu\text{W}$ for 854 nm / $\approx 600 \mu\text{W}$ for 866 nm), and the AOMs response must match the rf-signals created by the experiment control. Incorrect settings may result in a drop in measurement efficiency or even in the loss of trapped ions.

In our setup the 866 nm light is used for trapping, loading, and cooling the ions while the 854 nm light is used to couple the qubit state to the $P_{3/2}$ and is important for e.g. sideband cooling. Ions can be loaded, trapped, and manipulated using the rack-based setup. Loaded and Doppler-cooled ions can be seen on the CCD camera image figure [5.6](#).

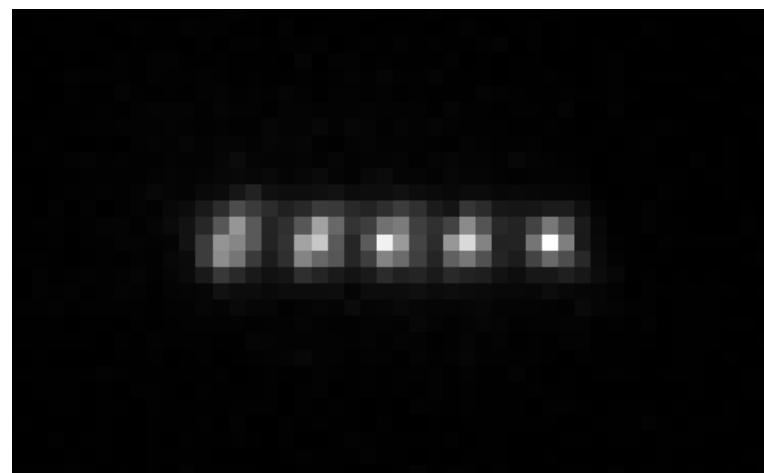


Figure 5.6: 5 ions are trapped in the linear Paul trapped and cooled using 397 nm light and the rack-based 866 nm laser. In the right image PMT counts for the individual ions are visible.

6 Narrow linewidth diode laser for 729 nm

Up to this chapter, the focus is on the design and characterization of a rack-based laser system for infrared lasers. In contrast to the infrared lasers, which are stabilized in the 100 kHz-regime, this chapter aims to stabilize a red diode laser to the Hertz regime. The red laser acts as a local oscillator driving the qubit transition. It should be more stable than the qubit transition to prevent introducing additional noise into the system, creating the requirement for as narrow and as stable lasers. The laser to be stabilized is a 729 nm (qubit transition) diode laser provided by Moglabs. As a reference, the TiSa [44] laser utilized by the experiments in our labs is used. The well-known linewidth of the TiSa allows conclusions about the linewidth of the Moglabs diode laser. The measured data is compared to a 729 nm diode laser built by Toptica.

6.1 Setup

The optical beat setup for the different lasers is identical for the Moglabs and the Toptica diode laser, therefore it is explained here only once. The main difference in the design is that the Toptica laser has a built-in TA amplifying the laser power to 500 mW while the Moglabs diode laser is not amplified and has an output power of 40 mW (fiber-coupled). Another difference is found in the design of the lasers. The Toptica laser is an ECDL based on the Littrow design, see 2.1.1, while the Moglabs diode laser is based on the cat-eye design, see 2.1.2. Both lasers have an intracavity EOM in their external cavities to reduce the linewidth actively. In comparison to frequency stabilizing the diode laser via current modulation, the intracavity EOM offers a bandwidth in the MHz to GHz range while having a reduced relative intensity noise [45]. Standard intracavity EOMs are based on crystals in the order of $4 \times 10 \times 40 \text{ mm}^3$ [45, 46]. In the case of the Moglabs diode laser, the typical intracavity EOM is replaced with a lithium-niobate chip, with a thickness of 0.5 mm and a height and width of 4.2 mm, deposited on the inside of the output coupler (OC) 2.4.

A high finesse cavity provides the feedback for the frequency stabilization (piezoelectric crystal of the external cavity and EOM). The schematic of the setup is shown in figure 6.1. The light of the Moglabs/Toptica diode laser is sent on a free space distribution breadboard. A halfwave plate and a polarizing beam cube are used to split up the laser light into two paths: One path is used to seed the high-finesse cavity (FSR: 1.5 GHz, Finesse 3×10^5 , fractional frequency stability 2×10^{-15} at 1 s integration time) built by Toptica while the second path is sent towards the experiment. The high-finesse cavity requires a laser light power of $10 \mu\text{W}$ to stabilize the laser. Exceeding this power threshold may damage several parts of the cavity while falling below it reduces the signal-to-noise ratio. Multiple AOMs and optical components

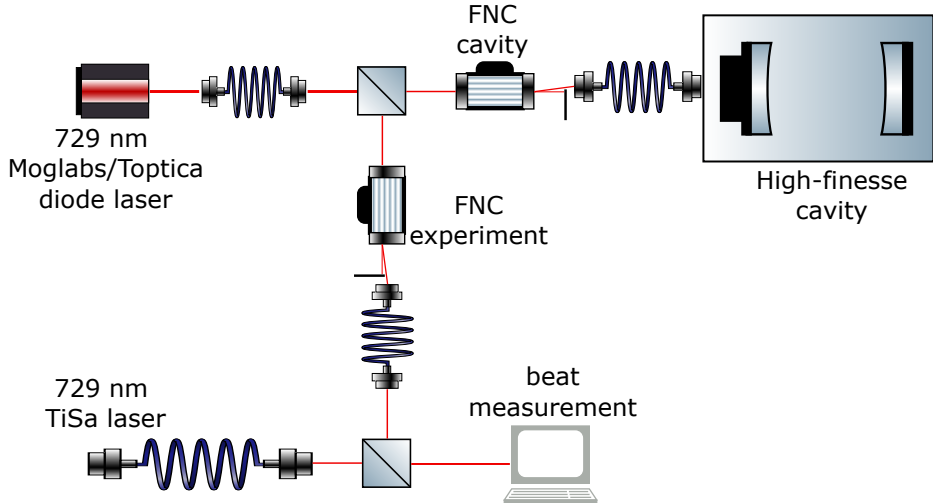


Figure 6.1: Schematic setup of the beat experiment. The Moglabs/Toptica laser is stabilized on the Toptica high-finesse cavity. The frequency-stabilized light is used to beat the TiSa 729 nm laser.

of the cavity setup increase the necessary power to a total input power of 20 mW, measured at the distribution breadboard.

A high-finesse cavity build by Toptica is used as reference stabilizing the laser frequency. The rf-output of the high-finesse cavity is sent to a FALC pro (PID) from Toptica, which is further connected to the laser head and the DLC pro. The DLC pro controls the FALC pro, the laser, and the high-finesse cavity. In the case of the Moglabs laser, an adapter board for the different cable types used by Toptica and Moglabs is necessary to connect the laser to the DLC and the FALC pro, which contributes to an increase in noise on the frequency and amplitude of the laser light due to insufficient shielding of rf-signals and electric fields.

The light in the experiment path is overlapped with the light coming from the MSQUARED 729 nm TiSa laser on a free space beam cube, which is similarly locked on a different high-finesse cavity [44]. A non-polarizing beam cube is used since a beat measurement requires the same polarization in both beams. Both beams are overlapped on a photodiode¹ and the beat is recorded using a spectrum analyzer.

6.2 Stabilization in the Hertz regime

This section will characterize the 729 nm Moglabs diode laser and compare the measured data to the data from the Toptica diode laser. Three key parameters are investigated: The lock bandwidth, the noise floor, and the linewidth.

Before starting these measurements, the Moglabs laser has to be locked on the high finesse cavity. The transmission and reflection of the cavity are visualized on an oscilloscope simplifying the optimization of the parameters of the FALC pro and the DLC pro. The optimization aims to archive continuous transmission through the cavity resulting in a stable lock. The FALC pro has 3 integrator (I_1, I_2, I_3) and two derivative (D_1, D_2) stages. The I_2 stage and both D stages are not used since they destabilize

¹Thorlabs PDA015A/M

Table 6.1: PI and FALC parameters

Stage	Gain	P	I	I_1	I_2	I_3
PID	5	0.005 V/V	0.011 V/V/ms	—	—	—
FALC	-5 dB	—	—	7 kHz	—	6 Hz

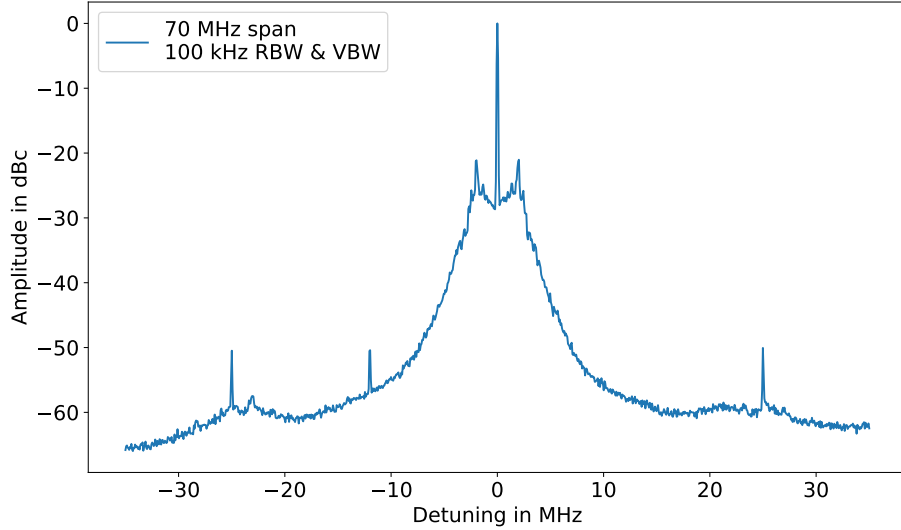


Figure 6.2: Beat between the Moglabs diode laser and the TiSa with a bandwidth of 70 MHz. The peaks at ± 25 MHz are the servo bumps created by the intracavity EOM of the Moglabs laser while the peaks at ± 2 MHz are created due to resonances in the lithium-niobate piezoelectric crystals in the cat-eye setup. The peak at ≈ -11 MHz is electric pickup of the fast photodiode.

the lock in our experiment. The cutoff frequency of I_1 and I_3 and the gain have to be adjusted to optimize the lock. Further optimization of the lock is done using the PI(D)² inside the DLC pro. Continuous transmission is achieved using the PI and FALC parameters given in the table 6.1. A beat measurement is used to optimize the lock beyond the resolution of the oscilloscope. The PI and FALC parameters are optimized to minimize the linewidth of the beat.

The first measurement focuses on the lock bandwidth of the Moglabs laser. It is dominated by the used EOM inside of the external cavity. The intracavity EOM used by Moglabs is smaller than the bulk EOMS typically used elsewhere, which may result in increased bandwidth and subsequently potentially enable hertz or sub-hertz linewidths [45]. A beat³ width a span of 70 MHz is recorded to measure the bandwidth of the intracavity EOM. The servo bumps created by the intracavity EOM are barely visible if the laser is locked correctly, they are at the noise level. For display purposes, the PI and the FALC gain are increased, decreasing the lock stability but amplifying the servo bumps created by the EOM. The servo bumps are shown in figure 6.2. The trace is averaged 100 times to increase the signal-to-noise ratio. The resolution bandwidth (RBW) and the video bandwidth (VBW) are set to 100 kHz on the spectrum analyzer. The servo bumps created by the intracavity EOM show

²The D-stage is not used.

³The absolute frequency difference between the Moglabs and the TiSa laser is ≈ 86 MHz.

Table 6.2: optimized PI and FALC parameters

Stage	Gain	P	I	I_1	I_2	I_3
PID	5	0.005 V/V	0.011 V/V/ms	–	–	–
FALC	−11 dB	–	–	7 MHz	–	18 Hz

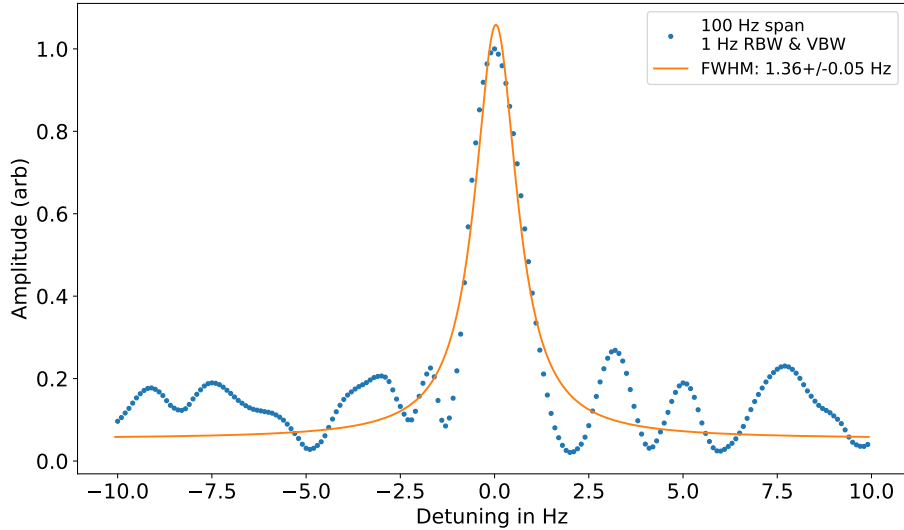


Figure 6.3: Beat signal between the Moglabs diode laser and TiSa reference laser, relative to the 86 MHz frequency difference between both lasers. The figure is zoomed in to ± 10 Hz around the beat signal.

up at ± 25 MHz. Two more peaks are shown at ± 2 MHz. They are created due to resonances in the lithium-niobate EOM of the external cavity of the laser. The peak measured at ≈ -11 MHz is an electric pickup of the fast photodiode.

The second measurement focuses on the linewidth of the beat between the TiSa and the Moglabs diode laser. The PI and the FALC pro parameters are optimized to narrow the linewidth of the beat. The optimized values are given in table 6.2. The beat between both lasers is shown in figure 6.3. The span of the beat measurement is set to 100 Hz and the RBW and VBW are set to 1 Hz (minimal values of the spectrum analyzer). The data is fitted using a Lorentzian curve (5.1) to measure the upper limit of the linewidth of the beat, resulting in a linewidth of 1.36(5) Hz. The amplitude is given in arbitrary units (linear scale) since it is not of interest in this measurement. The linewidth of the TiSa reference laser was determined by a three-cornered-hat measurement with two similar systems to 1.7(5) Hz in a previous measurement, leading to an upper limit of the linewidth of the Moglabs diode laser of 1 Hz. A reference laser with even narrower linewidth or a self-homodyne measurement scheme is necessary to increase the precision of the linewidth measurement.

A beat measurement with a span of > 10 MHz is necessary to investigate the lock bandwidth and the noise floor of the beat. The FALC pro and PI settings are the same as for the linewidth measurement. Special interest in the noise floor is at ± 1 MHz and ± 3 MHz around the beat since the axial and radial modes are located at this frequency. Reducing the noise floor prevents off-resonant coupling during gate operations. The beat measurement is shown in figure 6.4. The amplitude of the noise floor

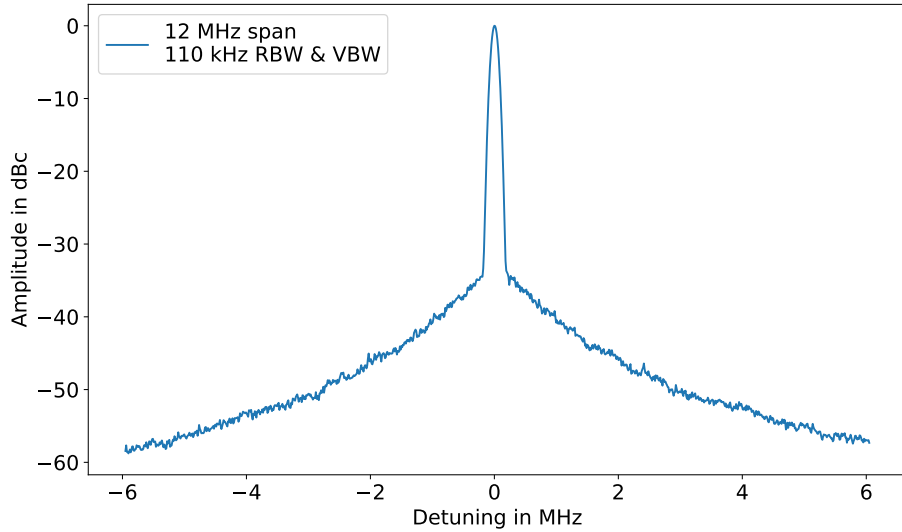


Figure 6.4: Noise floor and lock bandwidth measurement for the beat between the Moglabs diode laser and the TiSA laser. A noise floor of ≈ 92 dBc/Hz at 1 MHz and ≈ 101 dBc/Hz at 3 MHz is measured.

is ≈ 42 dBc at 1 MHz and ≈ 51 dBc at 3 MHz. We calculate the average amplitude spectral density of the beat measurement per frequency bin by dividing it by the RBW of the spectrum analyzer. A noise floor of ≈ 92 dBc/Hz at 1 MHz and ≈ 101 dBc/Hz at 3 MHz is measured. Furthermore, a locking bandwidth of 5 MHz is measured.

The Toptica diode laser is used to compare the results of the Moglabs laser. It replaces the Moglabs laser in the setup 6.1. As for the Moglabs laser the lock bandwidth, the noise floor, and the linewidth of the beat are the interesting parameters. A span of 100 Hz and a RBW = VBW = 1 Hz is chosen to measure the linewidth of the beat and to compare it to the Moglabs data. The linewidth measurement is shown in figure 6.5. The beat is fitted using the same Lorentzian function as for the Moglabs laser. A linewidth of $1.270(14)$ Hz is measured. The upper limit of the linewidth matches the upper limit of the linewidth of the Moglabs laser within two standard deviations. It can be assumed that the linewidth of both lasers locked to the high finesse cavity is in the same range. The signal-to-noise ratio of the beat is a factor of 2 higher for the Toptica laser. The reason for the increased signal-to-noise ratio may lie in a difference in the lock quality. The high finesse cavity is optimized for the Toptica lasers. For the Moglabs laser, no lock parameters were available and they were determined by optimizing the transmission through the cavity and narrowing the beat linewidth. A more stable set of parameters may be found during different measurements.

The span of the TiSa-Toptica beat is increased to 10 MHz to measure the noise floor at ± 1 MHz and ± 3 MHz around the beat and to measure the lock bandwidth. The measured data is shown in figure 6.6. The RBW = VBW = 5.1 kHz for this measurement. The course of the noise floor is different for the Toptica laser. In the case of the Moglabs diode laser, the amplitude of the noise floor steadily declines by increasing the distance to the beat while for the Toptica laser, the noise floor drops off more steeply and stays constant at about -60 dBc/Hz. The noise floor is ≈ 92 dBc at 1 MHz and ≈ 100 dBc/Hz at 3 MHz which is in the same range as for the Moglabs laser. The lock bandwidth of the Toptica laser is 5 MHz which is the same as for the

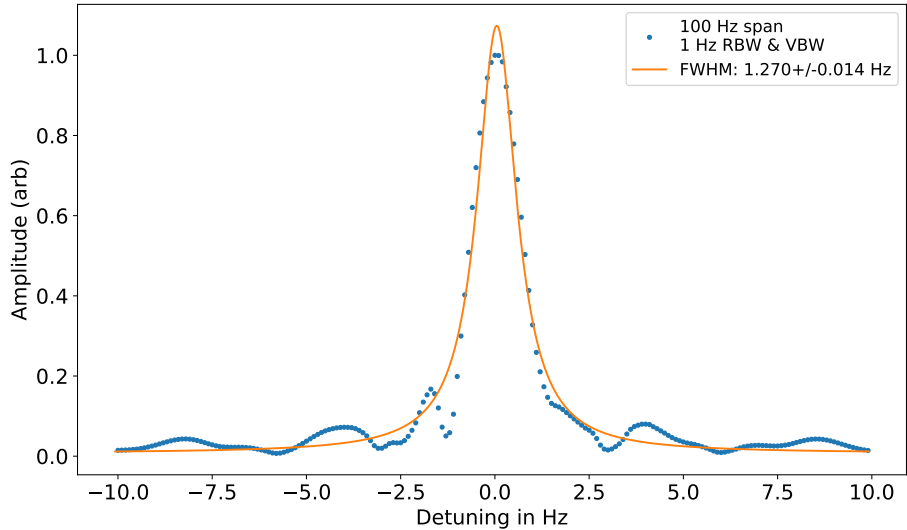


Figure 6.5: Beat TiSa-Toptica diode laser. The upper limit of the linewidth $1.270(14)$ Hz. The absolute frequency difference between both lasers is ≈ 82.9 MHz.

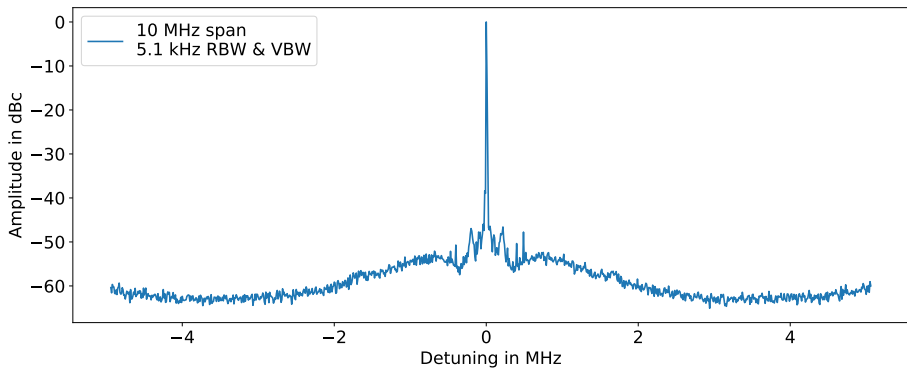


Figure 6.6: Beat TiSa-Toptica diode laser. Measurement of the lock bandwidth and the noise floor of the Toptica diode laser.

Moglabs laser.

The linewidth measurement has shown that the Moglabs diode laser can be stabilized to the 1 Hertz regime or lower. A more stable reference laser as the TiSa or a different measurement scheme is necessary to increase the precision of the measurement. The data of the beat measurement between the Moglabs and the TiSa lasers is published in [45]. The comparison to the Toptica diode laser returns similar values for both lasers for the linewidth, the noise floor, and the lock bandwidth. Ions are necessary for further comparison between both lasers. Interesting parameters are among others Rabi flops and gate fidelities. Seeding the ion with laser light provided by the Moglabs diode laser was out of scope for this work due to technical (laser power limitations in our setup) and time limitations.

7 Conclusion and outlook

The goal of this thesis was on the one hand to design and characterize a rack-based laser system for 854 nm and 866 nm and on the other hand to stabilize a diode laser to the Hertz regime and characterize the linewidth, noise floor, and lock bandwidth. The rack-based laser system is used to seed up to six experiments based on calcium 40 ions.

First the stability of the rack-based setup was tested. The parameters of interest were frequency stability, power loss, and the PER. A beat between a free space laser system and the rack-based system was used to measure an upper limit of the linewidth of the rack-based system at 177(2) kHz for the 854 nm laser and at 217(3) kHz for the 866 nm lasers. Next, a long-time frequency stability measurement was investigated. Both lasers were connected to a wavemeter WS8 and the frequency stability of the rack-based system was compared to the free space setup. The rack-based lasers did drift $< 1.8 \text{ MHz}$ in 70 h(854 nm)/15 h(866 nm) whereas the drift of the free space setup was $\approx 10 \text{ MHz}/24\text{h}$. It was shown that the accuracy of the wavemeter limited the frequency stability measurement of the rack-based setup and the measurement result is an upper limit to the drift. Nevertheless, the rack-based setup is at least more than five times more stable than the free space setup.

We characterized the light distribution setup and the double pass units. Both, the power and the PER were investigated. The PER in the light distribution setup is reduced from 27 dB (laser head) to 3–6 dB (cavity) since multiple fiber-based splitter and combiner are used in series. Nonetheless, stable locking of the lasers on the cavity has been achieved.

In the case of the double pass units, the power loss and the FWHM of the tuning range are investigated. A total loss of 50% was measured for 854 nm and 866 nm. An FWHM of 14.9(2) MHz was observed.

Currently the laser drift measurement is limited to 2 MHz due to the accuracy of the wavemeter. A beat between the rack-based and more stable reference lasers or a frequency comb would be necessary to measure the drift with higher accuracy and precision. A power spectral density measurement can be used to determine the exact linewidth of the rack-based lasers using a more stable reference laser. Further improvements on the PID parameters of the cavity can be made over time by investigating the laser drift and lock stability. However, this is beyond the scope of this thesis.

The second part was to stabilize a diode laser (Moglabs), based on a new concept of an intracavity EOM, to the Hertz regime and compare it to a diode laser using a bulk EOM inside a Littrow configuration (Toptica). The linewidth, the noise floor, and the lock bandwidth were investigated. The TiSa laser of our lab was used as a reference laser for the beat measurement. A linewidth of 1.36(5) Hz was measured for the beat between the Moglabs and the TiSa. The well-known linewidth of the TiSa of 1.7(5) Hz leads to an upper limit of the linewidth of the Moglabs diode laser of 1 Hz. A noise

floor of ≈ 92 dBc/Hz at 1 MHz and of ≈ 101 dBc/Hz at 3 MHz and a lock bandwidth of 5 MHz were measured. The beat Toptica-TiSa resulted in a linewidth of 1.270(14) Hz, matching the linewidth of the beat Moglabs-TiSa within two standard deviations. It can be expected that the linewidth of the Moglabs diode laser is in the same range as the Toptica diode laser. A noise floor of ≈ 92 dBc/Hz at 1 MHz and of ≈ 100 dBc/Hz at 3 MHz and a lock bandwidth of 5 MHz were measured for the Toptica diode laser, which is in the same range as for the Moglabs diode laser.

Further improvements of the linewidth measurement can be done using a more stable reference laser than the TiSa or by using a self-heterodyne measurement scheme [47]. Measurements on the ion are necessary for further investigation of the behavior of the Moglabs diode laser. Currently, it is not possible due to power limitations. A TA behind the laser is required to have enough power to perform such measurements on the ions.

Bibliography

- [1] J. PRESKILL, *Quantum computing 40 years later* (2021). URL <http://dx.doi.org/10.48550/ARXIV.2106.10522>.
- [2] D. DEUTSCH UND R. JOZSA, *Rapid solution of problems by quantum computation*, Proceedings of the Royal Society of London. Series A: Mathematical and Physical Sciences, **439**, 553 (1992).
- [3] P. SHOR, *Algorithms for quantum computation: discrete logarithms and factoring*, in *Proceedings 35th Annual Symposium on Foundations of Computer Science*, S. 124–134 (1994). URL <http://dx.doi.org/10.1109/SFCS.1994.365700>.
- [4] T. D. LADD, F. JELEZKO, R. LAFLAMME, Y. NAKAMURA, C. MONROE UND J. L. O'BRIEN, *Quantum computers*, Nature, **464**, 45 (2010). URL <http://dx.doi.org/10.1038/nature08812>.
- [5] J. HECHT, *Short history of Laser development*, Applied optics, **49** (2010). URL <http://dx.doi.org/10.1117/1.3483597>.
- [6] S. C. SINGH, H. ZENG, C. GUO UND W. CAI, *Lasers: Fundamentals, Types, and Operations*, Kap. 1, S. 1–34, John Wiley & Sons, Ltd (2012), ISBN 9783527646821.
- [7] J. EICHLER UND H. J. EICHLER, *Laser*, Springer Berlin Heidelberg, Berlin, Heidelberg (2010), ISBN 978-3-642-10461-9.
- [8] W. DEMTRÖDER, *Laserspektroskopie: Grundlagen und Techniken*, Springer Berlin Heidelberg, Berlin, Heidelberg, fünfte, erweiterte und neubearbeitete auflage Aufl., ISBN 978-3-540-33792-8.
- [9] W. W. CHOW UND S. W. KOCH, *Semiconductor-Laser Fundamentals*, Springer Berlin, Heidelberg (1999), ISBN 978-3-662-03880-2.
- [10] D. J. D'ORAZIO, M. J. PEARSON, J. T. SCHULTZ, D. SIDOR, M. W. BEST, K. M. GOODFELLOW, R. E. SCHOLTEN UND J. D. WHITE, *Measuring the speed of light using beating longitudinal modes in an open-cavity HeNe laser*, American Journal of Physics, **78**, 524 (2010). URL <http://dx.doi.org/10.1119/1.3299281>.
- [11] C. HENRY, *Theory of the linewidth of semiconductor lasers*, IEEE Journal of Quantum Electronics, **18**, 259 (1982). URL <http://dx.doi.org/10.1109/JQE.1982.1071522>.

BIBLIOGRAPHY

- [12] W. WANG, A. MAJOR UND J. PALIWAL, *Grating Stabilized External Cavity Diode Lasers for Raman Spectroscopy – A Review*, Applied Spectroscopy Reviews, **47** (2012). URL <http://dx.doi.org/10.1080/05704928.2011.631649>.
- [13] F. RIEHLE, *Frequency standards : basics and applications* (2004), ISBN 978-3-527-40230-4.
- [14] M. G. LITTMAN UND H. J. METCALF, *Spectrally narrow pulsed dye laser without beam expander*, Appl. Opt., **17**, 2224 (1978). URL <http://dx.doi.org/10.1364/AO.17.002224>.
- [15] MOG LABORATORIES PTY LTD, *External Cavity Diode Laser, Revision 1.20* (2021). URL https://www.moglabs.com/products/cateye-laser/MOGLabsCEL_manual_rev120.pdf.
- [16] X. BAILLARD, A. GAUGUET, S. BIZE, P. LEMONDE, P. LAURENT, A. CLAIRON UND P. ROSENBUSCH, *Interference-filter-stabilized external-cavity diode lasers*, Optics Communications, **266**, 609 (2006). URL <http://dx.doi.org/10.1016/j.optcom.2006.05.011>.
- [17] D. J. THOMPSON UND R. E. SCHOLTEN, *Narrow linewidth tunable external cavity diode laser using wide bandwidth filter*, Review of Scientific Instruments, **83**, 023107 (2012). URL <http://dx.doi.org/10.1063/1.3687441>.
- [18] T. ABDELZAHER, Y. DIAO, J. HELLERSTEIN, C. LU UND X. ZHU, *Introduction to Control Theory And Its Application to Computing Systems*, S. 185–215, Springer, Boston, MA (2008), ISBN 978-0-387-79360-3. URL http://dx.doi.org/10.1007/978-0-387-79361-0_7.
- [19] Z. MA UND S. ZOU, *Optimal Control Theory: The Variational Method*, Springer Singapore, Singapore (2021), ISBN 978-9-813-36291-8.
- [20] BEN GURION UNIVERSITY, *Feedforward control (PDF)* (2013). URL https://www.bgu.ac.il/chem_eng/pages/Courses/oren%20courses/Chapter_9.pdf.
- [21] R. ISERMANN, *Feedforward Control*, S. 56–67, Springer Berlin Heidelberg, Berlin, Heidelberg (1991), ISBN 978-3-642-86420-9. URL http://dx.doi.org/10.1007/978-3-642-86420-9_6.
- [22] I. D. DÍAZ-RODRÍGUEZ, *Analytical Design of PID Controllers* (2019), ISBN 978-3-030-18228-1.
- [23] B. M. VINAGRE, C. A. MONJE, A. J. CALDERÓN UND J. I. SUÁREZ, *Fractional PID Controllers for Industry Application. A Brief Introduction*, Journal of vibration and control, **13**, 1419 (2007).
- [24] J. G. ZIEGLER UND N. B. NICHOLS, *Optimum Settings for Automatic Controllers*, Journal of Dynamic Systems, Measurement, and Control, **115**, 220 (1993). URL <http://dx.doi.org/10.1115/1.2899060>.

BIBLIOGRAPHY

- [25] K. ÅSTRÖM UND T. HÄGGLUND, *PID Controllers: Theory, Design, and Tuning*, ISA - The Instrumentation, Systems and Automation Society (1995), ISBN 1-55617-516-7.
- [26] T. HANSCH UND B. COUILLAUD, *Laser frequency stabilization by polarization spectroscopy of a reflecting reference cavity*, Optics Communications, **35**, 441 (1980). URL [http://dx.doi.org/https://doi.org/10.1016/0030-4018\(80\)90069-3](http://dx.doi.org/https://doi.org/10.1016/0030-4018(80)90069-3).
- [27] N. CHABBRA, A. R. WADE, E. R. REES, A. J. SUTTON, A. STOCHINO, R. L. WARD, D. A. SHADDOCK UND K. MCKENZIE, *High stability laser locking to an optical cavity using tilt locking*, Opt. Lett., **46**, 3199 (2021). URL <http://dx.doi.org/10.1364/OL.427615>.
- [28] E. D. BLACK, *An introduction to Pound–Drever–Hall laser frequency stabilization*, American Journal of Physics, **69**, 79 (2001). <https://doi.org/10.1119/1.1286663>, URL <http://dx.doi.org/10.1119/1.1286663>.
- [29] B. E. A. SALEH UND M. C. TEICH, *Fundamentals of photonics*, Wiley series in pure and applied optics, Wiley, Newark (2019), ISBN 978-1-119-50687-5.
- [30] M. A. TRAN, D. HUANG UND J. E. BOWERS, *Tutorial on narrow linewidth tunable semiconductor lasers using Si/III-V heterogeneous integration*, APL Photonics, **4**, 111101 (2019). URL <http://dx.doi.org/10.1063/1.5124254>.
- [31] R. GERRITSMA, G. KIRCHMAIR, F. ZÄHRINGER, J. BENHELM, R. BLATT UND C. F. ROOS, *Precision measurement of the branching fractions of the 4p 2P3/2 decay of Ca II*, The European Physical Journal D, **50**, 13 (2008). URL <http://dx.doi.org/10.1140/epjd/e2008-00196-9>.
- [32] M. RAMM, T. PRUTTIVARASIN, M. KOKISH, I. TALUKDAR UND H. HÄFFNER, *Precision Measurement Method for Branching Fractions of Excited P_{1/2} States Applied to ⁴⁰Ca⁺*, Phys. Rev. Lett., **111**, 023004 (2013). URL <http://dx.doi.org/10.1103/PhysRevLett.111.023004>.
- [33] B. K. SAHOO, M. R. ISLAM, B. P. DAS, R. K. CHAUDHURI UND D. MUKHERJEE, *Lifetimes of the metastable ²D_{3/2,5/2} states in Ca⁺, Sr⁺, and Ba⁺*, Phys. Rev. A, **74**, 062504 (2006). URL <http://dx.doi.org/10.1103/PhysRevA.74.062504>.
- [34] P. STAANUM, I. S. JENSEN, R. G. MARTINUSSEN, D. VOIGT UND M. DREWSEN, *Lifetime measurement of the metastable 3d ²D_{5/2} state in the ⁴⁰Ca⁺ ion using the shelving technique on a few-ion string*, Phys. Rev. A, **69**, 032503 (2004). URL <http://dx.doi.org/10.1103/PhysRevA.69.032503>.
- [35] J. A. JONES UND D. JAKSCH, *Quantum Information, Computation and Communication*, Cambridge University Press (2012). URL <http://dx.doi.org/10.1017/CBO9781139028509>.
- [36] M. M. WILDE, *Quantum Information Theory*, Cambridge University Press (2013). URL <http://dx.doi.org/10.1017/CBO9781139525343>.

BIBLIOGRAPHY

- [37] M. A. NIELSEN, *Quantum computation and quantum information*, 10th anniversary ed.. Aufl. (2010), ISBN 9781107002173.
- [38] D. P. DiVINCENZO, *The Physical Implementation of Quantum Computation*, Fortschritte der Physik, **48**, 771 (2000). URL [http://dx.doi.org/10.1002/1521-3978\(200009\)48:9/11<771::aid-prop771>3.0.co;2-e](http://dx.doi.org/10.1002/1521-3978(200009)48:9/11<771::aid-prop771>3.0.co;2-e).
- [39] E. MAGESAN, R. BLUME-KOHOUT UND J. EMERSON, *Gate fidelity fluctuations and quantum process invariants*, Physical Review A, **84** (2011). URL <http://dx.doi.org/10.1103/physreva.84.012309>.
- [40] M. L. DAY, P. J. LOW, B. WHITE, R. ISLAM UND C. SENKO, *Limits on atomic qubit control from laser noise*, npj Quantum Information, **8**, 72 (2022). URL <http://dx.doi.org/10.1038/s41534-022-00586-4>.
- [41] I. POGORELOV, T. FELDKER, C. D. MARCINIAK ET AL., *Compact Ion-Trap Quantum Computing Demonstrator*, PRX Quantum, **2** (2021). URL <http://dx.doi.org/10.1103/prxquantum.2.020343>.
- [42] *BEECH - AQT*, <https://www.aqt.eu/beech-laser-stabilization/>. Accessed: 2022-10-05.
- [43] *Booster - Createch*, <https://createch.pl/product/booster/>. Accessed: 2022-10-05.
- [44] R. STRICKER, *Gatteroperationen hoher Güte in einem optischen Quantenbit* (2017). Leopold-Franzens Universität Innsbruck, Master thesis.
- [45] S. PALMER, A. BOES, G. REN ET AL., *High bandwidth frequency modulation of an external cavity diode laser using an intracavity lithium niobate electro-optic modulator as output coupler*, APL Photonics, **7**, 086106 (2022). URL <http://dx.doi.org/10.1063/5.0097880>.
- [46] A. CELIKOV, P. KERSTEN, F. RIEHLE, G. ZINNER, L. D'EVELYN, A. ZIBROV, V. VELICHANSKY UND J. HELMCKE, *External cavity diode laser high resolution spectroscopy of the Ca and Sr intercombination lines for the development of a transportable frequency/length standard*, in *Proceedings of the 1995 IEEE International Frequency Control Symposium (49th Annual Symposium)*, S. 153–160 (1995). URL <http://dx.doi.org/10.1109/FREQ.1995.483896>.
- [47] Z. YUAN, H. WANG, P. LIU ET AL., *Correlated self-heterodyne method for ultra-low-noise laser linewidth measurements*, Opt. Express, **30**, 25147 (2022). URL <http://dx.doi.org/10.1364/OE.458109>.

8 Appendix

8.1 Raspbudi Webpage

A python script runs on a raspberry pi to control the Raspbudy system remotely. The web server provides easy access to remotely change the frequency, phase, and power of the selected laser light via tuning the rf-output of the corresponding DDS unit. In figure 8.1 the control slider for the power (attenuation) and the frequency of the 854 nm and the 866 nm lasers is shown. For technical reasons, two DDS units are required to run the 854 nm AOM and therefore two sets of sliders are given.

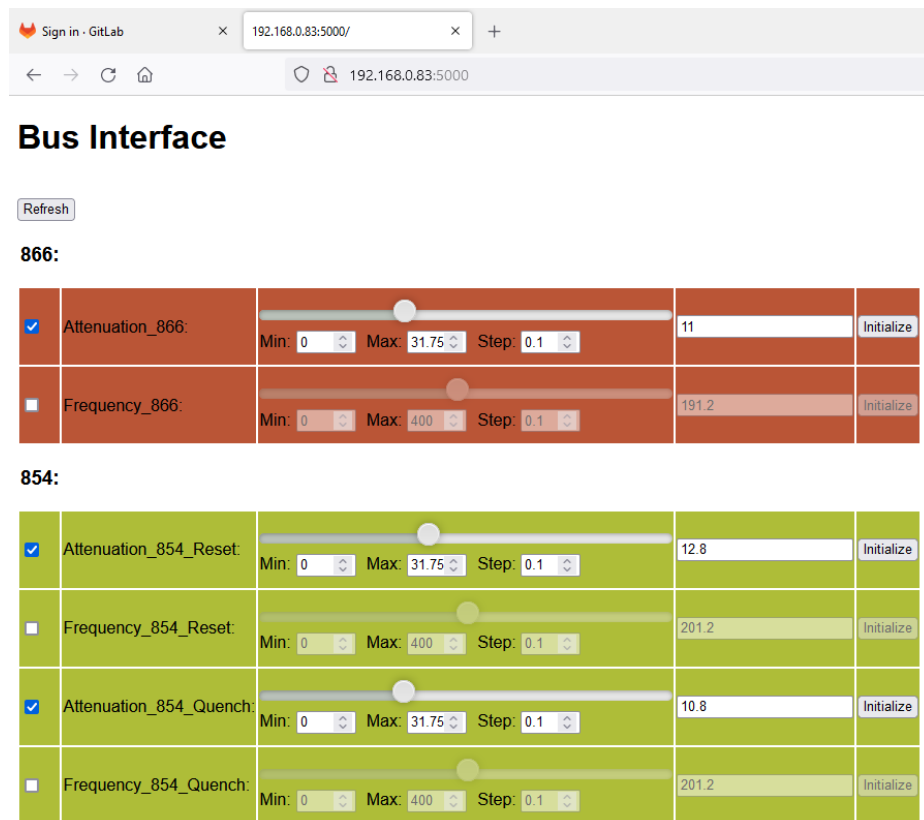


Figure 8.1: Controlling amplitude and frequency of the DDS output rf-signal. It is possible to control the phase of the laser light but it is not needed in this setup.

8.2 High bandwidth frequency modulation of an external cavity diode laser using an intracavity lithium niobate electro-optic modulator as output coupler

High bandwidth frequency modulation of an external cavity diode laser using an intracavity lithium niobate electro-optic modulator as output coupler

Cite as: APL Photonics 7, 086106 (2022); <https://doi.org/10.1063/5.0097880>

Submitted: 03 May 2022 • Accepted: 29 July 2022 • Accepted Manuscript Online: 07 August 2022 • Published Online: 30 August 2022

 S. Palmer,  A. Boes,  G. Ren, et al.

COLLECTIONS

 This paper was selected as Featured



ARTICLES YOU MAY BE INTERESTED IN

Reduced material loss in thin-film lithium niobate waveguides

APL Photonics 7, 081301 (2022); <https://doi.org/10.1063/5.0095146>

Low-loss fiber grating coupler on thin film lithium niobate platform

APL Photonics 7, 076103 (2022); <https://doi.org/10.1063/5.0093033>

Hybrid integrated external cavity laser with a 172-nm tuning range

APL Photonics 7, 066101 (2022); <https://doi.org/10.1063/5.0088119>

The advertisement features a periodic table of elements at the center. Surrounding the table are various material names and their applications:

- Yttrium iron garnet, glassy carbon, beamsplitters, fused quartz, additive manufacturing
- zeolites, III-V semiconductors, gallium lump, copper nanoparticles, organometallics
- nano ribbons, barium fluoride, europium phosphors, photonics
- silver nanoparticles, perovskites, transparent ceramics, OGS
- MOCVD, beta-barium borate, surface functionalized nanoparticles, MBE grade materials, thin film
- rare earth metals, quantum dots, CLED lighting, solar energy
- erbium, scintillation Ce:YAG, sputtering targets, fiber optics
- refractory metals, laser crystal, In-BN deposition slugs
- anode, lithium niobate, InAs wafers, CVD precursors, photovoltaics
- dysprosium pellets, MOFs, AuNPs, instamaterials, borosilicate glass
- chalcogenides, ZnS, CdTe, YBCO, superconductors, InGaAs
- perovskite crystals, transparent ceramics, indium tin oxide, MgF₂, nitrile
- transparent ceramics, diamond micropowder, optical glass

Now Invent.™

www.americanelements.com

© 2021 AEC. American Elements is a U.S. Department of Defense

APL Photonics 7, 086106 (2022); <https://doi.org/10.1063/5.0097880>

7, 086106

© 2022 Author(s).

High bandwidth frequency modulation of an external cavity diode laser using an intracavity lithium niobate electro-optic modulator as output coupler

Cite as: APL Photon. 7, 086106 (2022); doi: 10.1063/5.0097880

Submitted: 3 May 2022 • Accepted: 29 July 2022 •

Published Online: 30 August 2022



View Online



Export Citation



CrossMark

S. Palmer,^{1,a)} A. Boes,¹ G. Ren,¹ T. G. Nguyen,¹ S. J. Tempone-Wiltshire,² N. Longhurst,² P. M. Farrell,² A. Steiner,³ Ch. D. Marciniaik,³ T. Monz,^{3,4} A. Mitchell,¹ and R. E. Scholten^{2,5}

AFFILIATIONS

¹ Integrated Photonics and Applications Centre (InPAC), School of Engineering, RMIT University, Melbourne 3000, Australia

² MOGLabs, Carlton 3053, Australia

³ Institut für Experimentalphysik, 6020 Innsbruck, Austria

⁴ Alpine Quantum Technologies (AQT), 6020 Innsbruck, Austria

⁵ School of Physics, University of Melbourne, Parkville 3010, Australia

^{a)} Author to whom correspondence should be addressed: sonya.palmer@student.rmit.edu.au

ABSTRACT

We present a novel approach to high bandwidth laser frequency modulation. A lithium niobate chip is used as an intracavity electro-optic modulator in a tunable cat eye external cavity diode laser. The modulator is conveniently integrated with the cat eye output coupler, providing a unique approach to high bandwidth frequency stabilization and linewidth narrowing. The intracavity modulator feedback was successfully operated below 1 V and achieved superior frequency noise suppression compared to conventional feedback through diode injection current modulation. A closed loop bandwidth of 1.8 MHz was demonstrated, and the laser linewidth reduced to around 1 Hz as measured by the heterodyne measurement.

© 2022 Author(s). All article content, except where otherwise noted, is licensed under a Creative Commons Attribution (CC BY) license (<http://creativecommons.org/licenses/by/4.0/>). <https://doi.org/10.1063/5.0097880>

INTRODUCTION

Narrow linewidth frequency stabilized lasers are the basis of a wide range of applications from spectroscopy¹ and metrology² to precision timekeeping,³ atom trapping and cooling,⁴ and ion and atom qubits for quantum computation.⁵ External cavity semiconductor diode lasers (ECDLs) are predominantly used for such applications owing to their small size and weight, high efficiency, low cost, diverse wavelength coverage, tunability, low intensity noise, and narrow frequency linewidth. While the achievable linewidth and stability of these lasers are effective for many applications, advances in precision timekeeping^{6,7} quantum sensing,⁸ and quantum computing⁹ continue to further push the requirements for narrower linewidth and faster frequency control.

Frequency stabilization of ECDLs by using the feedback signal from comparison to a second reference laser, an atomic vapor cell, or a high-finesse cavity can be used to actively reduce the laser frequency uncertainty and linewidth. The feedback error signal drives one or more frequency actuators in the laser, typically a piezoelectric transducer for slow changes with a large laser frequency tuning range, and the diode injection current for smaller but faster corrections of the lasing frequency. The diode current response is a combination of relatively slow thermal effects and much faster refractive index changes related to the carrier density in the semiconductor gain medium,¹⁰ and will lead to an increase in the laser's relative intensity noise (RIN). Ideally, the active feedback linewidth reduction requires a feedback bandwidth that is comparable to, or greater than, the technical noise broadened ECDL

linewidth. In practice, it is challenging to achieve a feedback bandwidth of 2–3 MHz needed for sub-Hz linewidth by using this approach.

Intracavity electro-optic phase modulators (EOMs) offer an attractive alternative as a frequency feedback actuator.^{11–16} EOMs can have high bandwidth with a flat frequency response, from DC to many megahertz and even gigahertz with greatly reduced RIN when compared to modulating the laser diode current. For practical implementation in a laser cavity, a large crystalline EOM is typically used, for example, on the order of $4 \times 10 \times 40$ mm³.¹⁴ Large crystals are required to accommodate the 1–2 mm laser beam diameter in the cavity. The thickness of the crystal also reduces the electric field when applying a voltage to the electrodes, and therefore, relatively long crystals are needed to increase the electro-optic interaction length and reduce the driving voltage needed for a given phase shift.

In this paper, we experimentally demonstrate an EOM for intra-cavity linewidth narrowing, which is very compact and easily integrated into a catseye laser cavity configuration.¹⁷ A custom-made lithium niobate modulator is positioned at the focus of the catseye lens such that the active area of the modulator is small, enabling small electrode separation and, thus, a high field strength for a given electric potential difference. That, in turn, allows for a very short crystal interaction length, as short as the thickness of standard lithium niobate (LiNbO₃, LN) wafers (0.5 mm in our case), and fabrication using standard wafer processing methods. The compact size results in small capacitance and high modulation bandwidth. We demonstrate our intracavity EOM by using the Pound–Drever–Hall (PDH) technique for locking and linewidth narrowing of a 729 nm wavelength laser (the wavelength of the optical clock transition of $^{40}\text{Ca}^+$) to a high-finesse cavity. The intracavity modulator allows greater frequency noise suppression over a wider bandwidth compared to feedback via conventional modulation of the diode injection current.

BACKGROUND

Figure 1(a) shows the configuration of a standard catseye ECDL,¹⁷ with a large bulk electro-optic modulator (EOM) within the cavity. The catseye cavity configuration¹⁷ is self-aligning and, thus, mechanically robust and also ensures high efficiency of coupling between the diode and the external cavity, which reduces the linewidth. The catseye ECDL cavity length is typically around 30 mm with a 5 GHz free spectral range (FSR). An ultranarrow bandpass filter (bandwidth 0.20 ± 0.03 nm) is used to select a single external cavity mode. The rotation of the filter allows for tuning over a range of tens of nanometers, without affecting the direction of the output beam. The output coupler optic is fixed to a piezoelectric transducer that allows adjustment of the external cavity length and, thus, laser frequency over tens of GHz, with a bandwidth of tens of kHz. The EOM introduced here provides fast, high-fidelity control required for qubit manipulation, and linewidth narrowing needed for sensing and clock applications.

Figure 1(b) shows the design of the EOM output coupler, which uses an LN chip, with a thickness of 0.5 mm and a length and width of 4.2 mm. The chips were fabricated from a 76 mm X-cut Magnesium doped LN wafer. Magnesium doped wafers were used as they

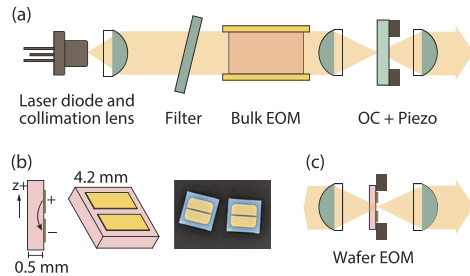


FIG. 1. (a) Schematic of catseye external cavity laser¹⁷ showing placement of an intra-cavity bulk crystal electro-optic modulator. OC: output coupler. (b) Schematic and photograph of wafer-based lithium niobate intra-cavity modulator with rectangular gold electrodes of 100 nm thickness. The gap spacing of the electrodes varied from 0.1 to 0.5 mm. An arrow between the electrodes indicates the electric field between them. (c) Modified catseye external cavity laser configuration with LN intra-cavity modulator. The inside surface is antireflection (AR) coated for 729 nm; the exit surface is uncoated, with Fresnel reflectivity of 15%.

are more robust to optical damage and degradation of the electro-optic effect when used at high optical power. After the deposition and patterning of 100 nm thick gold electrodes on the exit surface of the EOM, an antireflection (AR) coating for a wavelength of 729 nm was applied on the opposite surface. Figure 1(c) shows how the EOM acts as a partial mirror, replacing the fused silica of a typical catseye cavity output coupler. The cavity is formed between the laser diode highly reflecting rear facet and the reflectivity of the uncoated exit surface of the EOM, which has a Fresnel reflectivity of 15%, for a wavelength of 729 nm. A potential difference between the electrodes establishes an electric field that has a strong field component along LN's crystallographic z axis and is perpendicular to the laser propagation axis. If the polarization of the laser light is also along LN's crystallographic z axis, then the r_{33} electro-optic tensor element is the dominant electro-optic effect on the refractive index within the crystal.

The electro-optic coefficient $r_{33} = 32$ pm/V is small, and therefore, to achieve high phase modulation at practical electric potential differences, conventional single-crystal modulators (which are designed to work outside a laser cavity) are typically 20 or 30 mm in length and operate at hundreds of volts to achieve a few radians of phase shift. Our wafer-fabricated device relies on enhancement within a laser cavity, such that a 0.5 mm crystal can operate effectively at just a few volts. The change in frequency Δf due to refractive index change in the EOM is

$$\Delta f = \frac{f_0 dL}{L},$$

where $f_0 = c/\lambda_0$, c is the speed of light in vacuum, and λ_0 is the unmodulated wavelength, determined by the laser diode and filter angle (in our case, $\lambda_0 = 729$ nm). L is the cavity length, and the change in cavity length due to change in refractive index is $dL = L_{\text{LN}} dn$, where L_{LN} is the thickness of the LN wafer and dn is

$$dn = \frac{1}{2} r_{33} n^3 E,$$

with $n = 2.2022$ being the extraordinary refractive index of LN at 729 nm.

We used finite element analysis (CST Studio Suite[®]) to calculate the field strength in two dimensions through the thickness of the substrate with electrode separation of 0.3 mm and a potential difference of 1 V. **Figure 2(a)** shows a cross-section of the z-component of the field strength between the electrodes, and **Fig. 2(b)** shows the field strength of the z-component along the x axis (propagation direction) with the shaded region showing the field strength within the LN substrate. The calculated change in refractive index is $dn = 4.2 \times 10^{-11}$.

We investigated electrodes with a range of gap spacings (d_{gap}), from 0.1 to 0.5 mm. For a given potential difference, a smaller gap creates a stronger field, but increases the capacitance and reduces the bandwidth. For our devices, the capacitance of the electrode pair was below 0.1 pF even for the smallest gap, and, in practice, is overwhelmed by parasitic capacitance in the electrical connections and driving circuit. Hence, smaller gaps would be preferable; however, a smaller gap requires more accurate alignment to the laser axis and cat eye focus. The spot-size of the beam at the cat eye focus is $\sim 1.2 \mu\text{m}$ ($1/e^2$ diameter), with displacement around 0.1 mm per degree of incident angle. To accommodate imperfect alignment, an electrode spacing of 0.3 mm was chosen, giving an estimated frequency shift for 30 mm cavity length, 0.5 mm LN wafer, and 729 nm laser as

$$df = f_0 \frac{L_{\text{LN}}}{L} dn = \frac{c}{\lambda_0} \frac{L_{\text{LN}}}{L} 4.15 \times 10^{-11} \frac{V}{d_{\text{gap}}} = 0.9 \text{ MHz/V.}$$

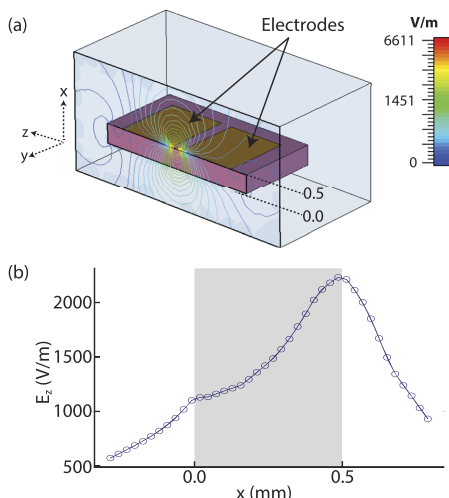


FIG. 2. Calculated electric field in the LN wafer modulator. (a) Cross-section of the E_z component of the field strength between the electrodes of the modulator. (b) E_z component of field strength along the x-direction with the area of the LN modulator indicated by the shaded region of the plot.

In other words, a potential difference of 1 V will shift the cavity lasing frequency by 0.9 MHz, approximately ten times greater than the passive linewidth of an ECDL. Therefore, in active corrections for frequency fluctuations of the laser and reduction of the effective linewidth, our wafer-fabricated cat eye modulator will theoretically operate at the output voltages of common low-voltage op-amp circuits. We have also successfully used the modulators at up to 20 Vpp.

INTRA-CAVITY ELECTRO-OPTIC MODULATOR SENSITIVITY AND BANDWIDTH

We used a high-finesse optical cavity to measure the spectral output of the cat eye ECDL. The laser frequency was scanned across the cavity resonance (cavity linewidth 70 kHz) while driving the intra-cavity EOM with a sinusoidal modulation at varying frequency. The electric field of the modulated laser output is proportional to $\cos(2\pi f_0 t + \beta \sin(2\pi f_m t)) = \sum_n J_n(\beta) \cos(2\pi(f_0 + n f_m)t)$, where f_0 and f_m are the carrier and modulation frequencies, respectively, and $J_n(\beta)$ is the Bessel function, with $\beta = \Delta f/f_m$ being the modulation index, that is, the maximum frequency deviation in terms of the modulation frequency. We fit the square of the electric field to the measured power spectrum, varying β to best match the relative power in each of the peaks, which are proportional to J_n^2 . The sensitivity is then $\Delta f/V$, where $\Delta f = \beta f_m$ and V is the amplitude of the sinusoid driving the modulator. **Figure 3(b)** shows the measured sensitivity varying from 0.6 to 1.4 MHz/V over a range of frequencies from DC to 16 MHz, consistent with the 0.9 MHz/V calculated earlier. At higher modulation frequency, the sideband amplitudes become too small to measure with this approach. Instead, we locked the laser frequency to the cavity by using diode current feedback (see later) and used a signal generator to drive the intra-cavity modulator. We measured the response of the error signal for varying modulation frequency, relative to the $1/f_{\text{mod}}$ decrease expected for the locking error signal.¹⁸ The 8 dB decrease over 50 MHz is consistent with the loss expected for an unterminated coax: the modulator is connected via coax and then ~ 10 cm of untwisted pair 32 AWG wire. The measured loss is very similar to the loss for the cable and untwisted wire without modulator, as measured using a vector network analyzer.

INTRA-CAVITY ELECTRO-OPTIC MODULATOR LINENWIDTH NARROWING

To demonstrate the effectiveness of the intracavity modulator, we used Pound–Drever–Hall (PDH) locking¹⁹ of the laser to a high-finesse cavity [see **Fig. 4(a)**]. Frequency modulation at ± 20 MHz was added with a fiber-coupled electro-optic phase modulator (ixBlue NIR-MPX800-LN-0.1). The reference cavity had a finesse of 21 000, a linewidth of 70 kHz, and free spectral range of 1.5 GHz. The light reflected from the cavity was detected with an amplified photodiode (Thorlabs PDA10A-EC) and mixed with the 20 MHz local oscillator to create a PDH error signal. The error signal was filtered by using a high-bandwidth low-latency servo controller (MOGLabs FSC). The low-frequency (SLOW) output from the fast servo controller (FSC) was connected to the laser piezo driver to correct for slow

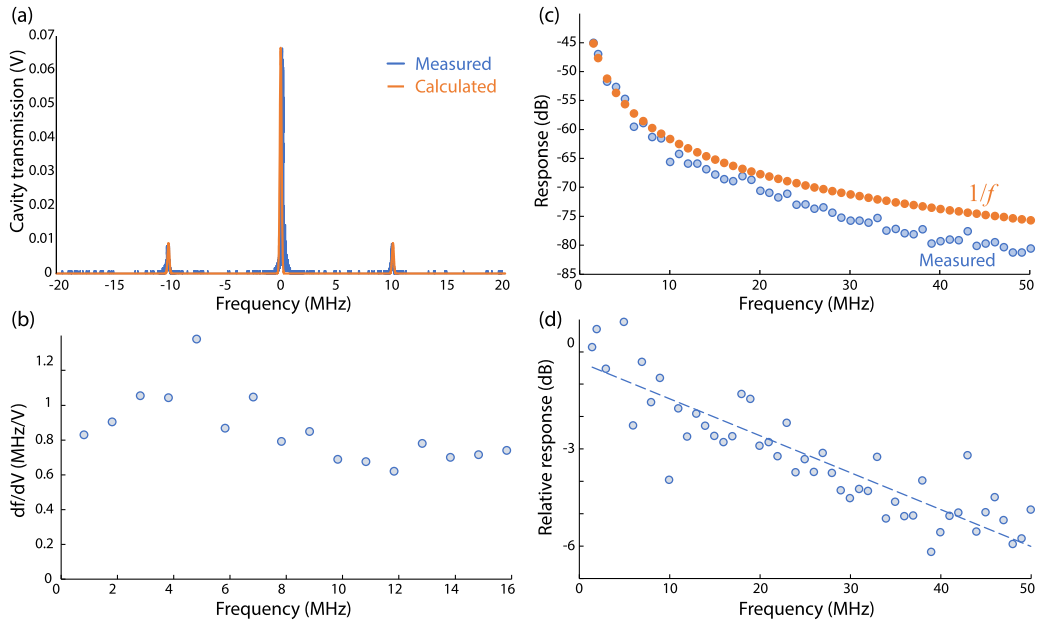


FIG. 3. (a) Laser spectrum at modulation frequency 10 MHz, measured as transmission through high-finesse cavity, with calculated spectrum. (b) Modulator sensitivity from DC to 16 MHz, determined from height of sidebands in (a). (c) PDH error signal response to disturbance from 1.5 to 50 MHz. (d) Measured modulator sensitivity as the difference between measured PDH response and expected PDH response (points), with linear regression (dashed). The -3 dB bandwidth is 25 MHz.

changes to lock the laser frequency to a cavity resonance, and the high-frequency (FAST) output was connected to either the diode injection current or the intra-cavity modulator to reduce the laser linewidth. The laser was operated with an output power of 10 mW, and the power incident on the optical cavity was $150 \mu\text{W}$.

Figure 4(b) (top) shows the cavity transmission and the PDH error signal when the laser is scanned through a cavity resonance. When the laser is locked to the resonance, the error signal reflects the feedback to maintain the laser at the transmission maximum [see Fig. 4(b) (bottom)].

In-loop noise spectra, measurements of the PDH error signal are shown in Fig. 5 for feedback to the intra-cavity modulator and to the diode injection current. The spectra were acquired with a 24-bit digitizer at 2.5×10^6 samples per second (up to 1 MHz) and an RF spectrum analyzer (above 1 MHz). The spectra were acquired with feedback off (unlocked, on resonance), with both piezo and fast feedback (full PID). The spectra were scaled from RF power to frequency noise density by using the slope of the error signal in Fig. 4(b).

For diode current feedback, a servo bump occurs at around 300 kHz, increasing to just above 1 MHz with maximum phase lead in the servo controller. For the intra-cavity modulator, the servo bump is found at up to 2.7 MHz, allowing greater gain and noise suppression; however, the maximum gain was limited by the

onset of oscillation at a narrow resonance in the feedback loop at 1.8 MHz.

Finally, we performed an optical heterodyne (beat measurement) of the laser with a second ultra-stable light source. The laser was PDH locked to an ultra-high-finesse cavity (free spectral range 1.5 GHz, finesse 3×10^5 , fractional frequency stability 2×10^{-15} at 1 s integration time) via a four-stage PI lock. Light was delivered from the catseye via optical fibers to both the cavity and a fast beat diode where it was overlapped with the second light source. The phase and amplitude noise from the fiber delivery were suppressed with additional PI stages and actuators to remove linewidth broadening effects. The reference source was a similarly stabilized Ti:sapphire laser with a linewidth of (1.7 ± 0.5) Hz determined by a three-cornered hat measurement with two similar systems co-located in Innsbruck (Austria). The absolute frequency difference between the two lasers leads to a beat signal centered around 86 MHz as recorded by a fast photodiode (Thorlabs PDA015A/M), with a central peak of (1.4 ± 0.1) Hz linewidth, as shown in Fig. 6(a). This linewidth is a convolution of the linewidths of the two sources and the resolution bandwidth of the spectrum analyzer (1 Hz) used to record the data, thus setting an upper bound on the true linewidth of 1 Hz. A more precise determination of the linewidth would require reference with even narrower linewidth or more complex self-homodyne techniques. When configured for minimum

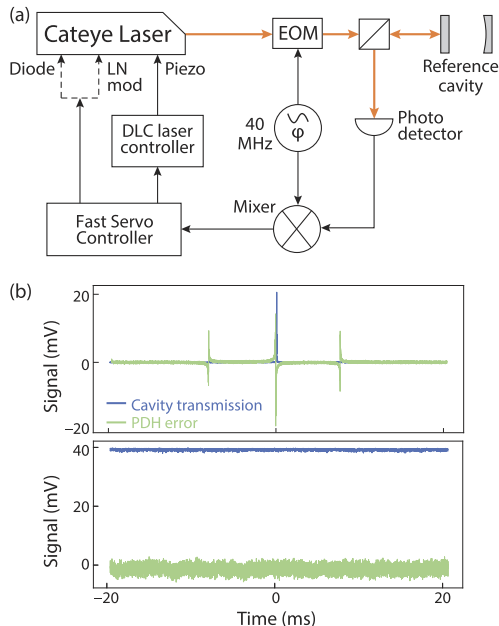


FIG. 4. (a) Simplified diagram of the Pound-Drever-Hall (PDH) locking setup, with the intracavity modulator inside a 729 nm wavelength cateye external cavity laser. (b) Cavity transmission and PDH error signals for laser scanning through the cavity resonance (top) and when locked (bottom).

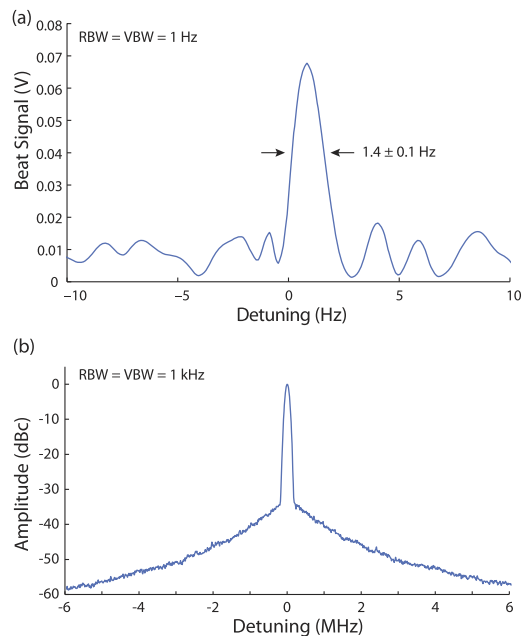


FIG. 6. (a) Beat signal between Ti:sapphire reference laser with the PDH-locked cateye laser, relative to the 86 MHz frequency difference between the two lasers. The linewidth of the resulting beat signal is a convolution of the linewidths of two sources and the spectrum analyzer (RBW 1 Hz), indicating an upper bound of 1 Hz for our laser linewidth. (b) Wide spectrum of the beat note, relative to 69 MHz, with lock parameters configured for a higher locking bandwidth.

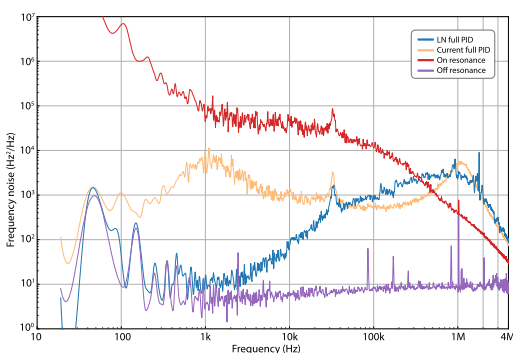


FIG. 5. In-loop noise spectra with feedback to intra-cavity modulator (LN full PID, blue) and to laser diode current (Current full PID, orange), compared to on resonance (no feedback) and off resonance.

linewidth, servo bumps appear at ± 5 MHz but higher locking bandwidths up to 20 MHz were observed, at the expense of central feature linewidth [see Fig. 6(b)].

CONCLUSION

In conclusion, we have demonstrated that the cateye external cavity laser design lends itself to the incorporation of a fast electro-optic modulator based on an LN wafer. With an LN chip at the focus of the cateye, the electrodes can be closely spaced to achieve the frequency modulation needed for frequency stabilization and linewidth narrowing by using signals of a volt or less, compatible with standard analog electronics without high voltage drivers. The low voltage and small size and capacitance of the modulator allow high modulation bandwidth. We stabilized the laser to a high-finesse optical cavity with up to 1.8 MHz closed-loop bandwidth, achieving linewidth narrowing to 1 Hz. We expect that improved narrowing and higher bandwidth should be achievable, for example, by using a higher finesse cavity to improve the signal-to-noise ratio, and with faster electronics to reduce the closed loop group delay. The wafer design could be used more generally in laser cavities that incorporate a tight

focus, for example, by placing the LN chip close to the emission facet of a laser diode in a Littrow or Littman–Metcalf configuration external cavity. We expect that when integrated into tunable lasers, the modulator will be useful for achieving high precision atomic clocks and high-fidelity rapid qubit operations with trapped ion quantum computers.

ACKNOWLEDGMENTS

The authors acknowledge the facilities, and the scientific and technical assistance, of the Micro Nano Research Facility (MNRF) and the Australian Microscopy and Microanalysis Research Facility at RMIT University. This work was performed, in part, at the Melbourne Centre for Nanofabrication (MCN) in the Victorian Node of the Australian National Fabrication Facility (ANFF). This research was supported by the ARC (Grant No. LP180100332). A.S., Ch.D.M., and T.M. acknowledge the support from the Austrian Science Fund (FWF), through SFB BeyondC (FWF Project No. F7109), and the IQI GmbH. T.M. and Ch.D.M. acknowledge funding from the Office of the Director of National Intelligence (ODNI), Intelligence Advanced Research Projects Activity (IARPA), via U.S. ARO Grant Nos. W911NF-16-1-0070 and W911NF-20-1-0007, and the U.S. Air Force Office of Scientific Research (AFOSR) via IOE Grant No. FA9550-19-1-7044 LASCEM.

AUTHOR DECLARATIONS

Conflict of Interest

Authors S.J.T.-W., N.L., P.M.F., and R.E.S. develop external cavity diode lasers at Moglabs.

Author Contributions

S. Palmer: Conceptualization (equal); Data curation (equal); Formal analysis (equal); Investigation (equal); Methodology (equal); Validation (equal); Writing – original draft (equal); Writing – review & editing (equal). **A. Boes:** Formal analysis (supporting); Supervision (equal); Validation (supporting); Writing – review & editing (equal). **G. Ren:** Formal analysis (supporting); Supervision (supporting); Validation (supporting); Writing – review & editing (equal). **T. G. Nguyen:** Formal analysis (supporting); Supervision (equal); Validation (supporting); Writing – review & editing (equal). **S. J. Tempone-Wiltshire:** Data curation (equal); Investigation (equal); Methodology (equal); Resources (supporting); Validation (supporting). **N. Longhurst:** Data curation (equal); Investigation (equal); Methodology (equal); Resources (supporting); Validation (supporting). **P. M. Farrell:** Data curation (equal); Investigation (equal); Methodology (equal); Resources (supporting); Validation (supporting). **A. Steiner:** Data curation (supporting); Formal analysis (supporting); Investigation (supporting); Validation (supporting); **Ch. D. Marciniak:** Data curation (supporting); Formal analysis (supporting); Supervision (supporting); Validation (supporting); Writing – review & editing (supporting). **T. Monz:** Data curation (supporting); Formal analysis (supporting); Supervision

(supporting); Validation (supporting). **A. Mitchell:** Formal analysis (supporting); Funding acquisition (lead); Resources (equal); Supervision (equal); Validation (equal); Writing – review & editing (equal). **R. E. Scholten:** Conceptualization (equal); Data curation (equal); Formal analysis (equal); Funding acquisition (supporting); Investigation (equal); Methodology (equal); Resources (equal); Supervision (equal); Validation (equal);

DATA AVAILABILITY

The data that support the findings of this study are available from the corresponding author upon reasonable request.

REFERENCES

- L. Gianfrani, R. W. Fox, and L. Hollberg, “Cavity-enhanced absorption spectroscopy of molecular oxygen,” *J. Opt. Soc. Am. B* **16**(12), 2247–2254 (1999).
- A. Cabral and J. Rebordão, “Accuracy of frequency-sweeping interferometry for absolute distance metrology,” *Opt. Eng.* **46**(7), 073602 (2007).
- Y. Jiang *et al.*, “Making optical atomic clocks more stable with 10^{-16} -level laser stabilization,” *Nat. Photonics* **5**(3), 158–161 (2011).
- T. W. Hänsch and A. L. Schawlow, “Cooling of gases by laser radiation,” *Opt. Commun.* **13**(1), 68–69 (1975).
- J. I. Cirac and P. Zoller, “Quantum computations with cold trapped ions,” *Phys. Rev. Lett.* **74**(20), 4091–4094 (1995).
- S. L. Campbell *et al.*, “A Fermi-degenerate three-dimensional optical lattice clock,” *Science* **358**(6359), 90–94 (2017).
- G. E. Marti, R. B. Hutson, A. Goban, S. L. Campbell, N. Poli, and J. Ye, “Imaging optical frequencies with 100 μ Hz precision and 1.1 μ m resolution,” *Phys. Rev. Lett.* **120**(10), 103201 (2018).
- J. P. McGilligan, P. F. Griffin, R. Elvin, S. J. Ingleby, E. Riis, and A. S. Arnold, “Grating chips for quantum technologies,” *Sci. Rep.* **7**(1), 384 (2017).
- N. Akerman, N. Navon, S. Kotler, Y. Glickman, and R. Ozeri, “Universal gate-set for trapped-ion qubits using a narrow linewidth diode laser,” *New J. Phys.* **17**(11), 113060 (2015).
- C. E. Wieman and L. Hollberg, “Using diode lasers for atomic physics,” *Rev. Sci. Instrum.* **62**(1), 1–20 (1991).
- B. C. Young, F. C. Cruz, W. M. Itano, and J. C. Bergquist, “Visible lasers with subhertz linewidths,” *Phys. Rev. Lett.* **82**(19), 3799–3802 (1999).
- H. Stoehr, F. Mensing, J. Helmcke, and U. Sterr, “Diode laser with 1 Hz linewidth,” *Opt. Lett.* **31**(6), 736–738 (2006).
- A. D. Ludlow *et al.*, “Compact, thermal-noise-limited optical cavity for diode laser stabilization at 1×10^{-15} ,” *Opt. Lett.* **32**(6), 641–643 (2007).
- A. Celikov *et al.*, “External cavity diode laser high resolution spectroscopy of the Cs and Sr intercombination lines for the development of a transportable frequency/length standard,” in *Proceedings of the 1995 IEEE International Frequency Control Symposium (49th Annual Symposium)* (IEEE, 1995), pp. 153–160.
- J. Le Gouët, J. Kim, C. Bourasson-Bouchet, M. Lours, A. Landragin, and F. Pereira Dos Santos, “Wide bandwidth phase-locked diode laser with an intra-cavity electro-optic modulator,” *Opt. Commun.* **282**(5), 977–980 (2009).
- N. Beverini, E. Maccioni, P. Marsili, A. Ruffini, and F. Sorrentino, “Frequency stabilization of a diode laser on the Cs D₂ resonance line by the Zeeman effect in a vapor cell,” *Appl. Phys. B* **73**(2), 133–138 (2001).
- D. J. Thompson and R. E. Scholten, “Narrow linewidth tunable external cavity diode laser using wide bandwidth filter,” *Rev. Sci. Instrum.* **83**(2), 023107 (2012).
- R. W. Fox, C. W. Oates, and L. W. Hollberg, “1. Stabilizing diode lasers to high-finesse cavities,” *Exp. Methods Phys. Sci.* **40**, 1–46 (2003).
- R. W. P. Drever *et al.*, “Laser phase and frequency stabilization using an optical resonator,” *Appl. Phys. B: Photophys. Laser Chem.* **31**(2), 97–105 (1983).